ROMA TRE
UNIVERSITÀ DEGLI STUDI

SCUOLA DOTTORALE DI INGEGNERIA SEZIONE DELL'ELETTRONICA BIOMEDICA, DELL'ELETTROMAGNETISMO E DELLE TELECOMUNICAZIONI

XXIII CICLO

Design of Metamaterials for Applications to Bioelectromagnetics
-
Progetto di Metamateriali per Applicazioni al Bioelettromagnetismo

Simone Tricarico

A.A. 2010/2011

Docente guida:	Prof. Lucio Vegni
Coordinatore:	Prof. Lucio Vegni
Tutor:	Prof. Filiberto Bilotti

INDICE

1. INTRODUCTION

"The great tragedy of Science: the slaying of a beautiful hypothesis by an ugly fact."

Thomas Henry Huxley

The intriguing properties of Metamaterials (MTMs) have been extensively investigated by the scientific community in the past years. Those kind of complex media show unusual and exotic properties, which may allow to overcome limitations affecting common devices, offering new viewpoints in the interpretation of singular physical phenomena. In the following work, the design and synthesis of MTMs will be deeply analyzed, showing how the application of such materials may lead to a sensible improvement in performances and reliability of common setups involved in the field of bioleletromagnetics, and, more in general, of applied electromagnetics.

In particular, a general overview about MTMs will be presented, introducing also the issues related to characterization and manufacturing of such materials. Some of the most important applications and advances involving MTMs will be also examined, proposing proper figures of merit to evaluate the technological impact with respect to standard available solutions. Peculiar phenomena related to the exotic properties of complex media will be also investigated, suggesting the possibility to synthesize new devices and to beat some intrinsic restrictions related to common setups.

In order to investigate both the theoretical and technological aspects, a general characteriazion technique for regular samples of MTMs and complex materials will be presented. Some usefull design tools will be also introduced, defining proper models and testing the validity of numeric approximations and discretization techniques, mainly with respect to the correct use of computer based electromagnetic solvers.

This work will focus then on the employement of MTMs to obtain novel results proposing new applications in different ranges of frequency, starting from the very low frequencies of electromagnetic fields involved in biological tissues and physiological processes up to optical frequencies related to probing and imaging problems.

In the proposed analysis, several fields will be involved, including Near-Field Scanning Optical Microscopy (NSOM), near-field spectroscopy, nano-manufacturing and nano-assembly. Consequently, optical MTMs will be also presented, exploiting the anomalous properties of such media to describe cloaking, plasmonic and other optical phenomena, with important aspects related to sensing (enhanced resolution) and to optical force manipulation (tweezers, nano-actuators).

1.1 Summary

L'attività di ricerca affrontata nel presente lavoro è stata incentrata sullo studio degli aspetti connessi alla progettazione ed alla sintesi dei metamateriali, con particolare attenzione alle loro applicazioni nell'ambito generale del bioelettromagnetismo. Più nel dettaglio, data la natura complessa ed altamente strutturata dei materiali coinvolti, il principale interesse è stato quello di introdurre delle opportune tecniche di caratterizzazione, ovvero delle procedure che consentano di derivare una descrizione consistente della risposta elettromagnetica di tali mezzi. Le suddette metodologie rendono possibile l'estrazione dei parametri costitutivi efficaci che modellano il comportamento del materiale in un desiderato intervallo di frequenze, facilitando di conseguenza il problema della sintesi. La prima parte del presente elaborato è quindi dedicata all'individuazione ed all'implementazione di nuove strategie per il calcolo di tali grandezze, migliorando le procedure classiche note in letteratura tramite opportuni algoritmi di ottimizzazione, introdotti allo scopo di eliminare le limitazioni che ne penalizzano le prestazioni in termini di accuratezza.

Una volta introdotte delle robuste metodologie di caratterizzazione per i MTM, è stato possibile analizzarne le anomale proprietà elettromagnetiche, indagando alcuni dei fenomeni fisici più interessanti che coinvolgono questo genere di materiali. Un'ampia sezione è stata quindi dedicata allo studio dell'invisibilità elettromagnetica (*cloaking*), ovvero alla riduzione dell'osservabilità di un oggetto tramite l'utilizzo di opportuni rivestimenti. L'uso dei metamateriali costituisce l'elemento fondamentale di tale tecnica, comunemente incentrata sulla sintesi di dispositivi in grado di diminuire

drasticamente gli effetti dello scattering, minimizzando anche i fenomeni di riflessione e assorbimento. Differenti configurazioni sono state analizzate a vari intervalli di frequenze, proponendo una descrizione in termini di efficienza e prestazioni tramite opportune figure di merito. Varie estensioni sono state introdotte applicando il paradigma della soppressione dello scattering a geometrie complesse e fortemente anisotrope. Proprio tali risultati si sono rivelati particolarmente importanti in applicazioni biomediche, tipicamente legate alla spettroscopia in campo vicino.

Si è quindi studiato il fenomeno del controllo delle forze ottiche mediante l'impiego di MTM a frequenze ottiche, proponendo un'interpretazione del legame fra i fenomeni dovuti alla pressione di radiazione esercitata su nano-particelle, e la variazione della relativa polarizzabiltià e sezione di scattering. Diverse applicazioni sono state analizzate, con riferimento ai problemi di *trapping* ed alla manipolazione di oggetti su scala nanometrica, nonché ai fenomeni di adesione dei campioni biologici in presenza di probe e sensori di misura.

Nell'ambito della caratterizzazione e modellazione di strutture e materiali complessi si inserisce inoltre il contributo di ricerca all'interno del progetto internazionale TREMOR: *Control strategies for FES active & semi-active tremor suppression*, il cui obiettivo è utilizzare la stimolazione elettrica per ripristinare una funzionalità muscolare parzialmente compromessa attraverso un array attivo di elettrodi superficiali opportunamente alimentati, posti a diretto contatto con la pelle. Lo scopo del lavoro è stata la sintesi di un modello elettromagnetico accurato del braccio umano, in grado di descrivere la risposta dei tessuti biologici ad una stimolazione elettrica funzionale, mirata a ridurre il tremore cui sono soggetti i pazienti affetti da patologia parkinsoniana. Tipicamente l'elettrostimolazione implica l'iniezione di correnti a basse frequenze, è stato quindi necessario uno studio preliminare delle tecniche di risoluzione disponibili per tali tipi di problematiche, in particolare per quanto concerne le applicazioni in ambito biologico. L'approccio adottato è stato quello di ridurre la complessità del problema attraverso l'introduzione di due modelli: uno macroscopico a bassa frequenza in grado di descrivere da un punto di vista strettamente elettromagnetico la risposta dei tessuti umani del braccio ad un'esposizione di correnti iniettate tramite una disposizione di elettrodi. Il secondo,

prettamente fisiologico, adatto a trattare la risposta muscolare in presenza di una distribuzione di campo indotta dalla schiera di elettrodi.

Per quanto riguarda il primo punto, su cui si è focalizzata l'attività di ricerca, si è sintetizzato un modello del braccio umano in grado di risolvere i dettagli dei tessuti coinvolti con sufficiente accuratezza anatomica. Si è quindi proceduto alla caratterizzazione dei tessuti a bassa frequenza tramite i parametri elettrici fondamentali (permittività e conducibilità elettriche) ed alla discretizzazione numerica del problema. Si è infine validato il modello introdotto, controllandone l'affidabilità e l'accuratezza attraverso un'analisi comparativa dei risultati prodotti, e definendo le classi di variabilità di alcuni dei parametri fondamentali, al fine di testare differenti configurazioni e dimostrare la consistenza dei dati ricavati.

2. METAMATERIALS: THEORETICAL ASPECTS AND DESIGN

In this section we summarize some of the most important features of MTMs, presenting the main characterization and design tools for the analysis and synthesis of these kind of media. We investigate some of their anomalous properties, introducing both analytical and heuristic models describing their macroscopic electromagnetic behavior.

2.1 Definitions and nomenclature

According to the general definition by the Virtual Institute for Artificial Electromagnetic Materials and Metamaterials (Metamorphose) [1] a Metamaterial is «*an arrangement of artificial structural elements, designed to achieve advantageous and unusual electromagnetic properties*». Such a generic definition may result incomplete, especially when dealing with all the possible issues related the synthesis of complex materials. In more detail, we may assert that a MTMs are artificial engineered materials designed by inserting either periodic or random arrays of scattering elements into a dielectric host matrix [2]. This arrangement of structural elements may exhibit collective effective electromagnetic properties not found in constituent materials, and not readily observed in nature. Typically, the anomalous behavior of these media is related to their effective constitutive parameters. In particular the determination of the sign of both the electric permittivity (ε) and the magnetic permeability (μ), allows to define a general classification of such materials [3], as reported in Figure 2.1.

Regular dielectrics usually exhibit a positive pair (ε, μ), and are denoted as double positive (DPS) materials. In single negative (SNG) metamaterials only one between permittivity and permeability is negative and, depending on the proper sign value, it is possible to divide them into epsilon-negative (ENG) or mu-negative (MNG) media. MTMs also includes materials with very low value of (ε, μ), the so called near-zero (or zero index) materials, and media with exceptionally high-valued parameters, often referred as extreme parameters materials [4].

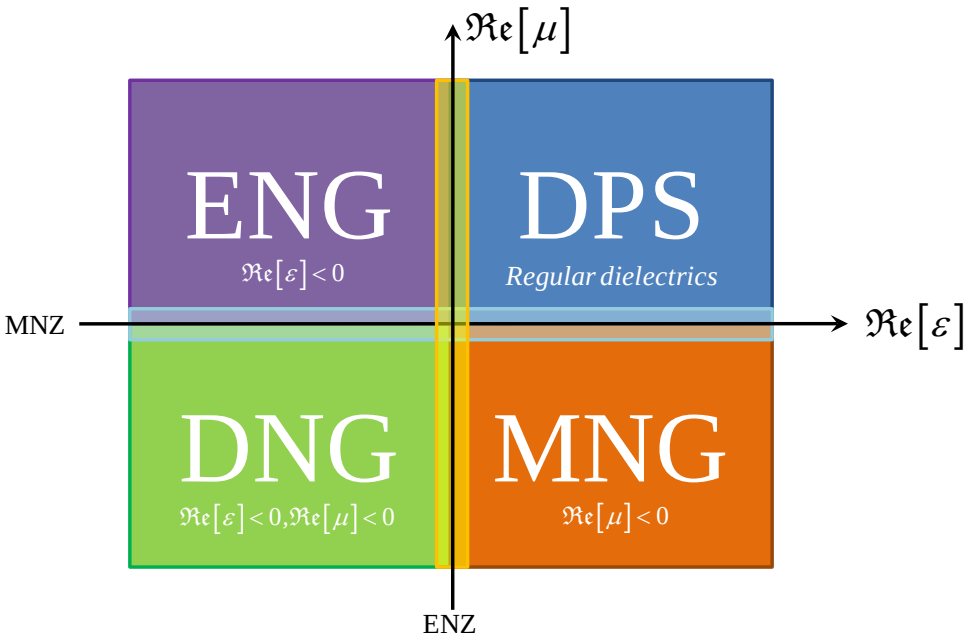

Figure 2.1 Metamaterial classification and nomencalture based on the sign of the real parts of constitutive parameters (ε,μ).

Properly designed metamaterials may thus assume, desired negative values of their parameters at a given frequency. Some of the most interesting effects arising in MTMs involve negative refraction, backward propagation and reversed Cherenkov and Doppler effects [2]. This exotic behaviors have been early investigated by different authors such as L.I. Mandelshtam, D.V. Sivukhin, but they are usually related to the paradigmatic paper of V. Veselago [5] about *the electrodynamics of substances with simultaneously negative values of* ε *and* μ. Anyhow, it is only after the work of J. Pendry [6]-[7] and the first experimental demonstrations [8] that the MTM field has gained a constant expanding interest.

Natural materials (noble metals and some dielectrics) may exhibit at optical frequencies a plasmonic behavior (that is a negative real valued bulk permittivity) explained in terms of electric resonances at a microscopic molecular scale [9]. Similarly, but scaled at lower frequencies, the inclusions hosted in MTMs mimick the response of molecular constituents, determining the macroscopic values of resulting effective parameters. In the following Sections it will be shown how it is theoretically possible to bring back in the visible regime the design concept at the base of MTM technology.

2.2 Synthesis and Characterization

Unusual electromagnetic properties are also produced in conventional materials, but the distinguishing feature of MTMs is that they can be specifically engineered to obtain a required behavior for a desired application. The size and spacing of elements in the material must be manufactured in order to be smaller than the operating wavelength. As a consequence, depending on the given frequency range, the embedding of properly shaped inclusions may lead to technological limitations in the fabrication process. Moreovrer, due to the finite size of the inclusions and their resonating behavior, the macroscopic electromagnetic parameters do show a frequency dispersion. Therefore, the same set of inclusions may return different values of permittivity and permeability and, thus, different electromagnetic properties, depending on the operating frequency.

The geometric dimensions and periodicity are thus important parameters in the synthesis of MTMs, and even if several theoretical models have been developed to relate them to response of composite media [11], they usually fail in completely describing the material response in a wide frequency range. Moreover most of the assumptions introduced to simplify the derivation of closed form expressions may be unrealistic when considering real life implemented setups. This aspect has determined a progressive effort to properly characterize MTMs, in particular defining unambiguous values of their effective constitutive values of permittivity and permeability.

It is well known that in the long wavelength limit the propagation of electromagnetic waves in structured medium can be described in terms of average fields and effective parameters. Under particular conditions an homogenization procedure can be thus applied, assuming the propagation of electromagnetic waves in such complex media as described by effective parameters determined only by the properties and concentration of the constituent inclusions [12]. Typically, this assumption is valid if both the inclusion characteristic size and its periodicity are sufficiently small compared to the operating wavelength. In this case, in fact, the scatterers embedded in the host matrix may modeled as dipoles. Assuming only one Bloch mode propagating in the periodic lattice, it is thus possible to

consider the material as homogeneous and, in general, anisotropic. By defining the particle electric and magnetic dipoles:

$$\begin{cases} \mathbf{p} = \underline{\alpha}_{ee} \cdot \mathbf{E}_{loc} + \underline{\alpha}_{em} \cdot \mathbf{H}_{loc} \\ \mathbf{m} = \underline{\alpha}_{me} \cdot \mathbf{E}_{loc} + \underline{\alpha}_{mm} \cdot \mathbf{H}_{loc} \end{cases} . \tag{2.2.1}$$

being $\underline{\alpha}_{ij}$ the polarizability tensor and $(\mathbf{E}_{loc}, \mathbf{H}_{loc})$ the the local fields close to the inclusions, effective parameters can be derived by applying Clasius-Mosotti formula and Maxwell-Garnett expression [13-15]. Only if the magneto-electric coupling is negligible and the inclusions properly distributed along the main axes, scalar effective parameters may be introduced.

Since the polarizabilities are related to the geometric characteristics of the inclusions, a proper engineered response is theoretically possible. However, as already anticipated, standard models developed to describe the electromagnetic response of inclusion based metamaterials fail when the scatterers are not sufficiently diluted in the hosting volume in order to consider them as non-interacting particles [16].

Usually, an alternative yet simple approach to characterize these media, is to assume that they should interact with the impinging radiation as continuous materials in a properly chosen frequency range. If this assumption is valid, the metamaterial sample may be modelled as an homogeneous slab with effective parameters [17]. Then, these parameters can be derived by inverting the scattering coefficients of the sample, as proposed in [18]-[19]. However, the used approximation may lead to ambiguous values of the retrieved effective permittivity and permeability. Moreover, as clearly shown in [20], the equivalent slab model is often inadequate to consistently describe the metamaterial behavior and to respect the boundary conditions.

The Transmission/Reflection (TR) techniques, in fact, are typically used with planar samples, exploiting the Fresnel formulas only for normal incidence. Even if some results have been extended also to bi-anisotropic metamaterials [21], the extracted parameters may present unexpected frequency dispersion and thickness depending values. These issues are due to the inherently dispersive nature of metamaterials, which, according to

Kramers-Kronig relations, should exhibit a proper dispersion profile satisfying the locality conditions [22]. Considering for instance the frequency dispersion of complex electric permittivity $\varepsilon(\omega)=\varepsilon'(\omega)-j\varepsilon''(\omega)$, according to causality it must be:

$$\begin{aligned}\varepsilon'(\omega)-\varepsilon_\infty &= \frac{1}{\pi}\mathcal{P}\int_{-\infty}^{+\infty}\frac{\varepsilon''(\omega_0)}{\omega_0-\omega}\mathrm{d}\omega_0 \\ \varepsilon''(\omega) &= -\frac{1}{\pi}\mathcal{P}\int_{-\infty}^{+\infty}\frac{\varepsilon'(\omega_0)-\varepsilon_\infty}{\omega_0-\omega}\mathrm{d}\omega_0\end{aligned}, \tag{2.2.2}$$

where $\varepsilon_R(\omega),\varepsilon_I(\omega)$ are the real and imaginary part of the complex permittivity, respectively, at a given frequency, ω is the frequency, the symbol $\mathcal{P}$ denotes the principal value for the integral and ε_∞ is the high frequency dielectric constant, defines as:

$$\lim_{\omega\to\infty}\varepsilon(\omega)=\varepsilon_\infty . \tag{2.2.3}$$

It may be easily derived from relations (2.2.2) that, in order to show negative values of ε, MTMs should be considered as inherently frequency dispersive media and, as a consequence of Kramers-Kronig relations, they should also exhibit losses, as it will be more extensively shown in the next Section. Moreover, remembering the properties of the Hilbert transform it is easy to find that:

$$\begin{aligned}\varepsilon(\omega) &= \varepsilon^*(-\omega) \\ \varepsilon_R(\omega) &= \varepsilon_R(-\omega) \\ \varepsilon_I(\omega) &= -\varepsilon_I(-\omega)\end{aligned} . \tag{2.2.4}$$

with similar expression for the permeability. The parameters retrieved through classical TR techniques may violate the causality condition and, consequently the dispersive behavior predicted by the previous relations. A simple but effective approach to overcome such limitations is the implementation of a retrieval algorithm based on the inversion of the transmission and reflection coefficients, as in TR techniques, but with a numerical optimization procedure forcing the effective parameters to match a set of dispersion models, as proposed in [18]-[19]. This approach is able to provide reliable parameters not affected by standard technique limitations,

as anomalous and spurious resonances, sign inversion and causality violation.

The physical interpretation of these parameters is of course more severe, and is not intended to provide an univocal representation of the real constitutive parameters of the sample, but rather to give a simple tool to properly design metamaterial inspired devices [23]. In fact, in order to effectively synthesize the medium, is sufficient that inclusion based sample exhibit the same behavior of an ideal metamaterial for a given polarization and angle of incidence.

2.2.1 Dispersion Models and Scattering Parameters Inversion

Several models describing the material frequency dependence may be used. The Lorentz profile satisfies all the previous conditions, as a consequence of Titchmarsh theorem, and it may be expressed in term of relative permittivity $\varepsilon(\omega)=\varepsilon_0\varepsilon_r(\omega)$ or permeability $\mu(\omega)=\mu_0\mu_r(\omega)$ as:

$$\varepsilon_r(\omega)=\varepsilon_\infty+\frac{(\varepsilon_s-\varepsilon_\infty)\omega_0^2}{(\omega_0^2-\omega^2)+j\omega\delta},\quad \mu_r(\omega)=\mu_\infty+\frac{(\mu_s-\mu_\infty)\omega_0^2}{(\omega_0^2-\omega^2)+j\omega\delta}. \tag{2.2.5}$$

where (ε_0,μ_0) are the permittivity and permeability of vacuum, (ε_s,μ_s) the model values at low frequencies, ω_0 the resonant frequency and δ the damping factor. Expressions (2.2.5) may be straightforwardly derived by the equation of damped harmonic oscillators. Generally, materials exhibit a collection of Lorentz oscillators with different frequencies, so the previous formulas can be generalized by a superimposition procedure.

It is possible to extend the Lorentz model, which usually applies to dielectrics, also to the case of metals. Since in such media the electrons are unbound and they experience zero restoring force, no resonance frequency can be defined. The Drude motel represent is thus defined as:

$$\varepsilon_r(\omega)=1-\frac{\omega_p^2}{\omega(\omega-j\nu)}. \tag{2.2.6}$$

where ω_p is the plasma frequency and ν the collision frequency. Near the plasma frequency, in a low loss regime, the real part of epsilon is extremely low.

While the Lorentz model satisfies Kramers-Kronig relations also in the limit case of no losses, the Drude profile cannot be applied on the entire spectrum without violating the causality condition. Neverthelss formula (2.2.6) may be effectively used to describe the dispersion behaviour of a given material in a properly defined frequency range. Clearly, in the lossless scenario, by applying the electromagnetic energy denstity *W* definition [2]:

$$W = \frac{1}{2}\left[\frac{\partial(\omega\varepsilon)}{\partial\omega}|E|^2 + \frac{\partial(\omega\mu)}{\partial\omega}|H|^2\right], \tag{2.2.7}$$

it is easy the understand that, in order to keep *W* a positive quantity, the parameter dispersion must satisfy the derivative conditions:

$$\frac{\partial(\omega\varepsilon)}{\partial\omega} \geq 0, \quad \frac{\partial(\omega\mu)}{\partial\omega} \geq 0, \tag{2.2.8}$$

If only passive materials are considered, under a monochromatic harmonic excitation $e^{-j\omega t}$, then it must necessarly be $\Im\mathfrak{w}\{(\varepsilon,\mu)\} < 0$;

In order to retrieve the effective constitutive parameters of uniform planar slabs, several procedures have been proposed in literature. Among all these techniques, the TR approach is one of the most applied, because it may be extremely useful to easily characterize material samples in a given frequency range. In this methodology, the extraction of the relative electric permittivity and permeability is performed by inverting the scattering coefficients associated.

This paradigm has been extensively investigated by Nicholson, Ross and Weir (NRW technique) [18]-[19], and it may be formally derived by the classical Fresnel formulas associated to a planar indefinite uniform slab of thickness *d*, with relative constitutive parameters $\varepsilon_{eff}(\omega), \mu_{eff}(\omega)$ illuminated by a normally impinging monochromatic plane wave (see Figure 2.2):

$$R(\omega)=\frac{\Gamma(\omega)\left(1-e^{-2jkd}\right)}{1-\Gamma(\omega)^2 e^{-2jkd}}, \qquad T(\omega)=\frac{e^{-jkd}\left[1-\Gamma(\omega)^2\right]}{1-\Gamma(\omega)^2 e^{-2jkd}} \tag{2.2.9}$$

where $R(\omega)$ and $T(\omega)$ are the reflection and transmission coefficients respectively (calculated at the sample interfaces), $k=k_0\sqrt{\varepsilon_{eff}(\omega)\mu_{eff}(\omega)}$ is the wave-number in the medium, $k_0=\omega\sqrt{\varepsilon_0\mu_0}$ is the wave-number in free space, and Γ the reflection coefficient for the semi-infinite problem, that is

$$\Gamma(\omega)=\frac{\eta(\omega)-1}{\eta(\omega)+1} \qquad \eta(\omega)=\sqrt{\frac{\mu_{eff}(\omega)}{\varepsilon_{eff}(\omega)}}. \tag{2.2.10}$$

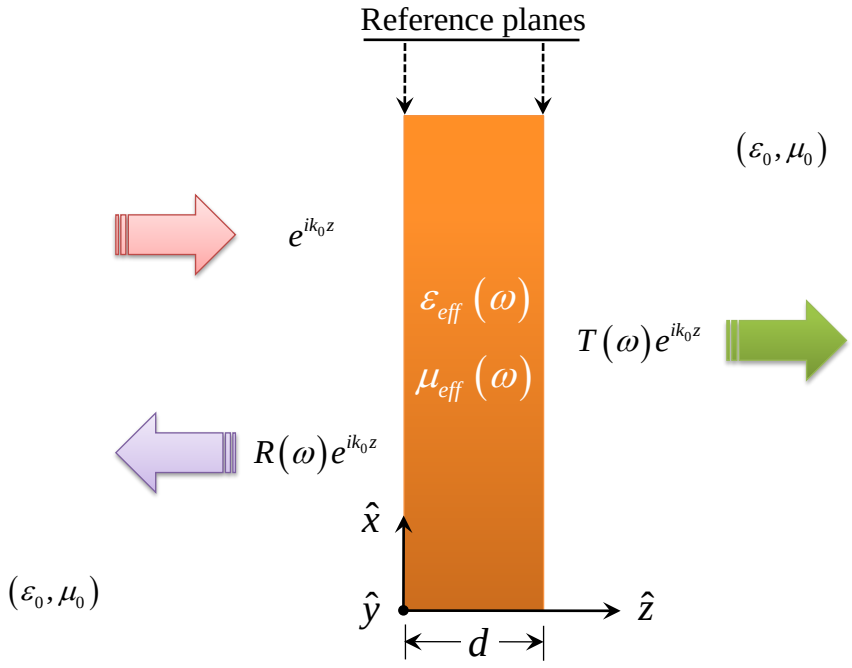

Figure 2.2 Scattering coefficients at the interfaces of a uniform planar unbounded slab.

The values of $R(\omega)$ and $T(\omega)$ are, indeed, frequency dependent because they constitute the spectral response of the material, assuming it dispersive, to the illuminating radiation. The frequency profile of $\varepsilon_{eff}(\omega)$ and $\mu_{eff}(\omega)$ may be extracted by inverting expressions, combining the scattering coefficients as:

$$\cos kd = \cos\left[k_0 n(\omega) d\right] = \frac{1+T(\omega)^2 - R(\omega)^2}{2T(\omega)}, \quad n(\omega) = \sqrt{\varepsilon_{eff}(\omega)\mu_{eff}(\omega)} \qquad (2.2.11)$$

$$\eta(\omega) = \alpha(\omega) \pm \sqrt{\alpha(\omega)^2 - 1}$$

and introducing the complex refractive index $n(\omega) = n_R(\omega) + jn_I(\omega)$, being

$$\alpha(\omega) = \frac{1+R(\omega)^2 - T(\omega)^2}{\sqrt{\left[1+R(\omega)^2 - T(\omega)^2\right]^2 - 4T(\omega)^2}}. \qquad (2.2.12)$$

$$\frac{1+\Gamma(\omega)^2}{2\Gamma(\omega)} = \frac{1-\left[T(\omega)-R(\omega)\right]\left[T(\omega)+R(\omega)\right]}{2R(\omega)}$$

The desired values of permittivity and permeability may be written then as

$$\varepsilon_{eff}(\omega) = \frac{n(\omega)}{\eta(\omega)}, \quad \mu_{eff}(\omega) = n(\omega)\eta(\omega). \qquad (2.2.13)$$

Formulas (2.2.13) represent the core of NRW procedure, which relies on computing the refractive index and the characteristic impedance of the sample. Despite the straightforward derivation, these equations do not hold, generally, for metamaterials, and they fail in properly characterizing the medium over a wide frequency region. This is due to the fact that expressions (2.2.11) are inherently affected by significant limitations, which may lead to numerical instability. In fact, in order to apply the set (2.2.13), we have to invert a cosine function involving complex oscillating quantities, which may lead to multiple branches and discontinuities, especially for electrically thick samples (i.e. for large values of the argument). This implies that it is necessary to check the solutions to verify if the correct branch has been chosen, and the task is generally complicated also by the presence of square roots and sign ambiguities. In order to validate the results some additional conditions have to be posed, such the passivity of the material (typically $|\Gamma| \le 1$) or calculating the group delay.

Intuitively, if the electrical thickness *kd* is small, it is possible to approximate the involved harmonic functions by a proper series expansion, reducing the complexity of the inversion procedure. An alternative is then to pick small samples, even if that may increase the measurement uncertainty [24]. A criterion to properly choose the electrical thickness is to have the value of *d*

at the higher frequency of interest smaller than half wavelength in the sample. In fact, whit low-loss materials is easy to verify that, when the scattering coefficient reach limit value $R(\omega)\to 0$ (d is an integer multiple of half wavelength in the sample) the numeric procedure does not converge, and similar conditions may rise usually for all the NRW variants in which we express constitutive parameter as a combination of $R(\omega)$ and $T(\omega)$.

As a result of these limitations, the NRW techniques often produces anomalous retrieved parameters, typically affected by sign inversions, spurious resonances, and unexpected slope changes. This is principally due to the evaluation $n(\omega)$ in which we have the product of $\varepsilon_{eff}(\omega)$ and $\mu_{eff}(\omega)$, which are not completely decoupled. However, the frequency profile of the constitutive parameters should respond to proper constraints in order to match the causality condition and satisfy Kramers-Kronig relations. For electrically small samples, the expressions:

$$\begin{aligned}\frac{R(\omega)+T(\omega)-1}{R(\omega)+T(\omega)+1}&=-\frac{j}{\eta(\omega)}\tan\frac{kd}{2}\\ \frac{T(\omega)-R(\omega)-1}{T(\omega)-R(\omega)+1}&=-j\eta(\omega)\tan\frac{kd}{2}\end{aligned}, \tag{2.2.14}$$

may be simplified by a series expansion of the argument kd, obtaining

$$\begin{aligned}\frac{R(\omega)+T(\omega)-1}{R(\omega)+T(\omega)+1}&\simeq -j\frac{k_0 d}{2}\varepsilon_{eff}(\omega)\\ \frac{T(\omega)-R(\omega)-1}{T(\omega)-R(\omega)+1}&\simeq -j\frac{k_0 d}{2}\mu_{eff}(\omega)\end{aligned}. \tag{2.2.15}$$

Expressions (2.2.15) lead to a direct decoupled representation of the relative electric permittivity and permeability through the $R(\omega)$ and $T(\omega)$ spectra. Never though, this expressions may be slightly inaccurate in the frequency regions where the permittivity and permeability may exhibit resonances, or for thicker samples, so that generally (2.2.12) must be used.

Moreover a minimum thickness is required to apply homogenization procedure to metamaterial samples. As pointed out in [20]-[22], the homogeneous slab model may not hold with meta-surfaces or alignments of single layer inclusions, because the physical extension of the equivalent slab

cannot be directly related to the unit cell dimensions. In addition, the characteristic impedance $\eta(\omega)$ should not vary with the thickness, but complex inhomogeneous materials generally may not exhibit a constant impedance. In order to extract some significant values of the constitutive parameters, as proposed by [25], an additional gap δ should be considered, fixing the reference plane to a proper distance from the unit cell external walls (see Figure 2.3), assuring the reflected and transmitted waves to be consistent with the hypothesis of plane wave propagation at the effective boundaries planes of the sample, as supposed by use of formulas (2.2.9).

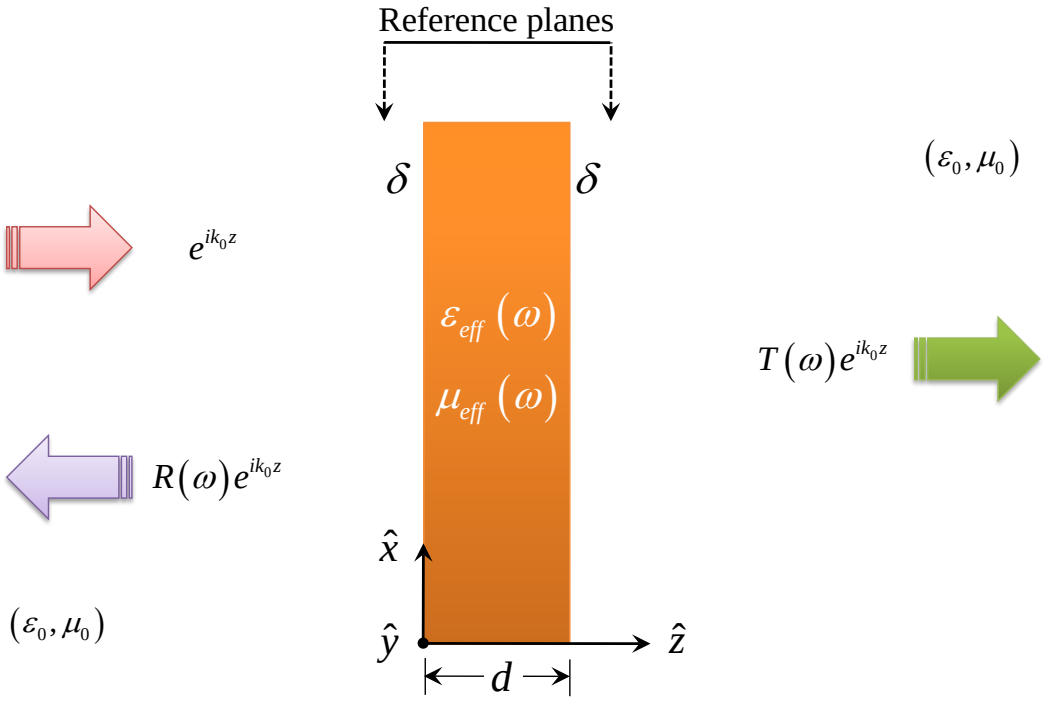

Figure 2.3 Virtual boundaries of the equivalent uniform planar slab.

These gap may be evaluated numerically through the following procedure. As suggested by Grigorenko in [26]-[27], one may think to choose, a priori, a prescribed dispersive model for the material, defining a set of parameters univocally determining the frequency behaviour of the sample. Parametric algorithms should be then used to improve the performances of the inversion techniques, avoiding some of the drawbacks affecting the TR procedures. The overall approach is based on acquiring the reflection $R(\omega)$

and transmission $T(\omega)$ spectra for a given sample thickness, matching them to the ones estimated by assigning the mask for $\varepsilon_{eff}(\omega)$ and $\mu_{eff}(\omega)$ through a numerical fitting, performed relatively to a proper set of parameters according to equations (2.2.11) or (2.2.13).

The virtual gaps can be then calculated, together with the other unknown parameters, by iteratively comparing the acquired spectra to the estimation. Obviously this method does not provide the actual effective parameters of the metamaterial, but rather an equivalent representation of the sample as an homogeneous slab which under normal incidence of a plane wave exhibits the same scattering coefficients. As anticipated, however, this assumptions, it is not strict from the point of view of metamaterial-inspired devices.

Moreover, by choosing the proper dispersion model for the constitutive parameters, Kramers-Kronig relations and then the causality condition may be automatically satisfied. Obviously, the dispersion profile is determined by the electromagnetic properties of the samples (i.e. by the expected electromagnetic response of the inclusions hosted in the material to the impinging radiation). This procedure may be thus straightforwardly applied in the case of Lorentz dispersion, or in the case of a dispersive model which does not satisfy the locality condition over all the spectrum (like the Drude one).

Then, numeric matching algorithms can be implemented to improve the performance of the inversion techniques. The global procedure can be summarized in few points:

- acquiring $R(\omega)$ and $T(\omega)$ spectra by direct measurements or simulations;
- fixing dispersive models for the permittivity and/or permeability;
- matching the acquired spectra for the given sample thickness with a best-fit procedure, performed relatively to a set of fitting parameters (depending on the dispersion model assumed);
- comparing the acquired spectra with the estimation $\overline{R}(\omega)$ and $\overline{T}(\omega)$ obtained by the retrieved parameters.

Different optimization algorithms have been developed in order to obtain the matching condition, using the previous found expressions or other combinations of the spectral parameters already known in literature [28]-[30].

First of all, a numeric code based on commercial symbolic software Mathematica© [31] has been written. The matching procedure has been performed through a best fit process. It has been introduced also a non-linear regression approach in order to improve the performances. The numeric retrieval has been validate by simulating the scattering parameters of a regular homogenoeus dispersive slab, acquired by simulating the strucure through CST Microwave Studio™ [32], a finite integration based commercial electromagnetic solver. The layout is reported in Figure 2.4, the sample is enclosed in a virtual box delimited by facing perfect electric and magnetic walls. According to boundary conditions the structure support a propagating monochromatic plane wave normally impinging on the sample surface.

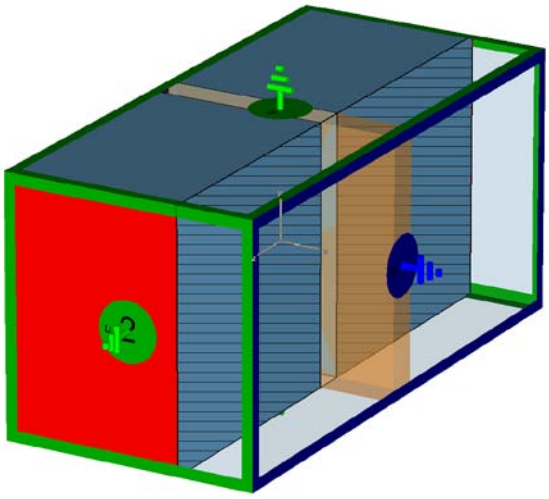

Figure 2.4 Simulation setup of a planar MTM sample for acquiring scattering parameters.

The setup is excited by two ports ports at which the reflection and transmissions coefficinets are calculated. The spectra values on the sample surface may be thus derived by a simple parameter deembedding with respect to the reference planes. The procedure may be applied both at microwaves and at visible frequencies, as it will be shown in the following. Moreover, at very low frequencies expressions (2.2.15) can be used to fasten

the algorithm, allowing the characterization of different samples [33]-[34]. In order to calibrate the overall procedure, initially a prescribed dispersive profile has been fixed for the sample. The software alloes to choose the dispersion model and its parameters, so the first verification has been the matching of the retrieved values with the one predicted by the simulator. A Lorentz dispersion model for the permeability has been used while keeping the permittivity constant, using the following parameters:

$$\begin{aligned} d &= 3\,[mm], \quad \varepsilon = 3 \\ \mu_\infty &= 1 \\ \mu_s &= 4 \\ \omega_0 &= 3\cdot 2\pi\cdot 10^9\ [rad/s] \end{aligned} \qquad (2.2.16)$$

As expected, the algorithm returned estimated values very close to originl ones:

$$\begin{aligned} \bar{d} &\approx 3\,[mm], \quad \bar{\varepsilon} \approx 3.1 \\ \bar{\mu}_\infty &\approx 1.1 \\ \bar{\mu}_s &\approx 4.03 \\ \bar{\omega}_0 &\approx 2.99\cdot 2\pi\cdot 10^9\ [rad/s] \end{aligned} \qquad (2.2.17)$$

Compairison with the resulting spectra are reported in Figure 2.5.

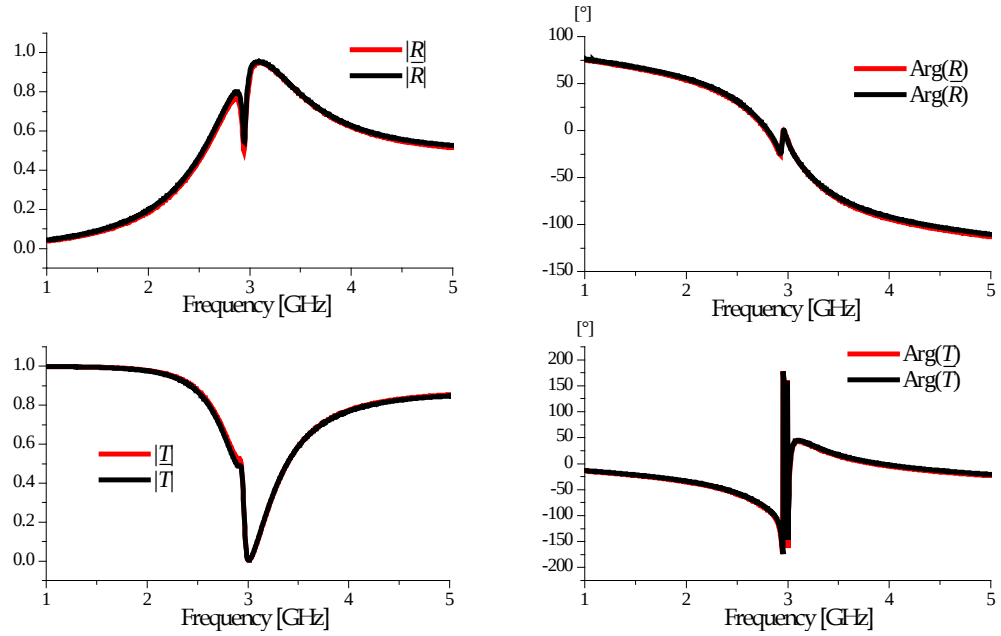

Figure 2.5 Compairison between the simulated spectra and the ones retrieved by applying the implemented extraction procedure.

By applying the standard TR approach, we obtain poorer results. In fact, even if a constant epsilon has been chosen, the inversion of the scattering parameters return a frequency varying permittivity, thus introducing a spurious dispersion which does not characterize the original material, as shown in Figure 2.6

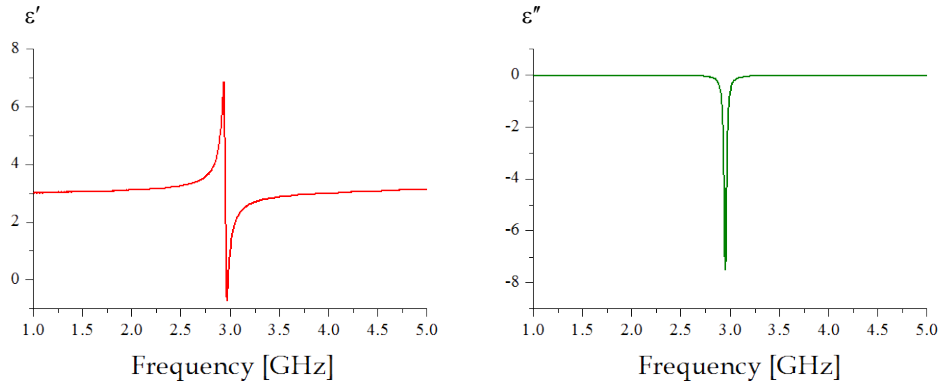

Figure 2.6 Dispersion for the electric permittivity introduced by standard TR inversion technique.

The second class test has been performed by introducing a double dispersion for both the electric permittivity and the permeability, by using the values:

$$\begin{aligned} d &= 3\,[mm] \\ \mu_\infty &= 1 \\ \mu_s &= 4 \\ \omega_{0\mu} &= 3\cdot 2\pi\cdot 10^9\,[rad/s], \\ \varepsilon_\infty &= 1 \\ \varepsilon_s &= 2 \\ \omega_{0\varepsilon} &= 2\cdot 2\pi\cdot 10^9\,[rad/s] \end{aligned} \qquad (2.2.18)$$

where the pedix in the resonance frequency identify the referring constitutive parameter.

Also in this case, the algorithm is able to separate the frequency profile of both the constitutive parameters, providing a robust alternative to classic inversion techniques which may be significantly affected by non locality artifacts in the frequency region where the two dispersion models overlaps. The resulting extracted values $(\bar{\varepsilon},\bar{\mu})$ are reported in Figure 2.7.

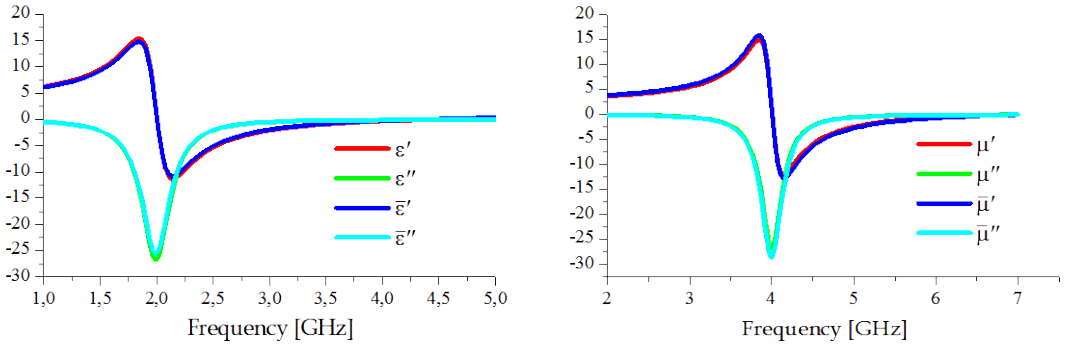

Figure 2.7 Simulated and retrieved dispersive constitutive parameters of the sample.

Before simulating real life MTM unit cell based on resonating inclusions, the retrieval procedure has been verified in the case of larger sample thickness. This is a fundamental issue when dealing with the characterization of bulky MTMs. As anticipated for not electrically small samples, the TR techniques suffer different limitation in the inversion of scattering coefficients. This is due to the rapidly oscillating nature of the involved complex quantities. The previous approach has been then applied to a sample with thickness comparable to the operating wavelength, with constant permeability and Lorentz dispersion for epsilon, posing:

$$\begin{aligned} d &= 33\,[mm] \\ \varepsilon_\infty &= 1 \\ \varepsilon_s &= 2 \\ \mu &= 3 \\ \omega_0 &= 2\cdot 2\pi\cdot 10^9\,[rad/s] \end{aligned} \quad . \tag{2.2.19}$$

Once again, the extracted values do not significantly vary from the chosen ones:

$$\begin{aligned} \bar{d} &\approx 33\,[mm], \quad \bar{\mu} \approx 3.04 \\ \bar{\varepsilon}_\infty &\approx 1.0 \\ \bar{\varepsilon}_s &\approx 2.0 \\ \bar{\omega}_0 &\approx 2.07\cdot 2\pi\cdot 10^9\,[rad/s] \end{aligned} \quad , \tag{2.2.20}$$

assuring that also for moderately large materials the characterization procedure may still be applied, as shown in Figure 2.8. However, especially when dealing with highly disperive material, the attenuation due to losses may worsen the matching accordance of the retrieved parameters.

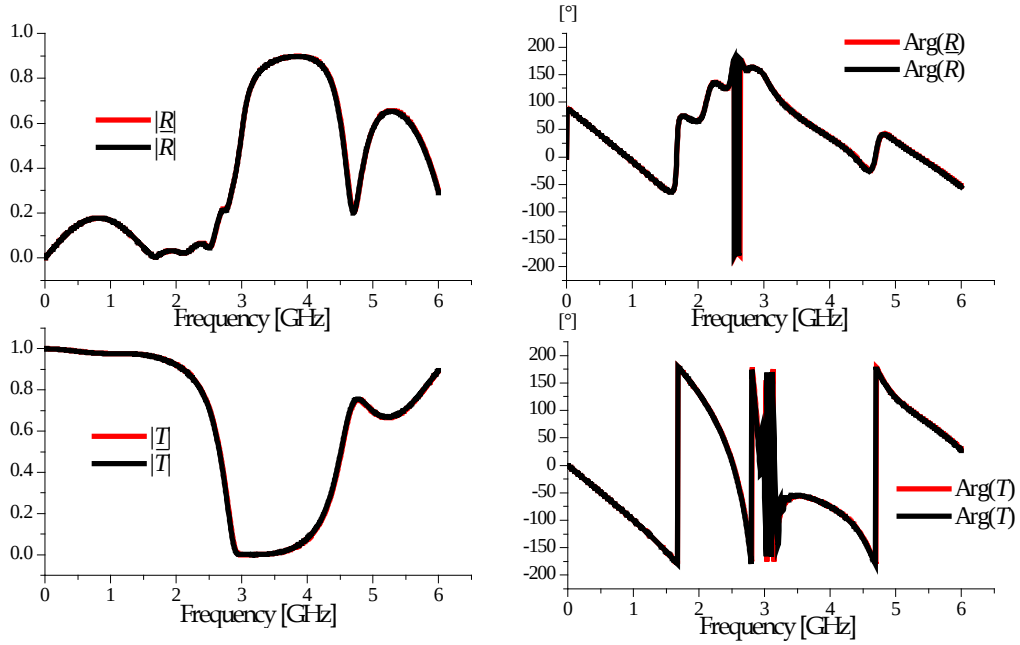

Figure 2.8 Compairison between the simulated spectra and the ones retrieved by applying the implemented extraction procedure.

The approach is anyway slightly affected by usual limitations due to the standard numerical inversion techniques. By comparing the result, it is clear that the values obtained with typical TR procedure do not provide an exact representation of the material behavior, by introducing spurious resonances and ripples in the dispersion profile, as reported in Figure 2.9

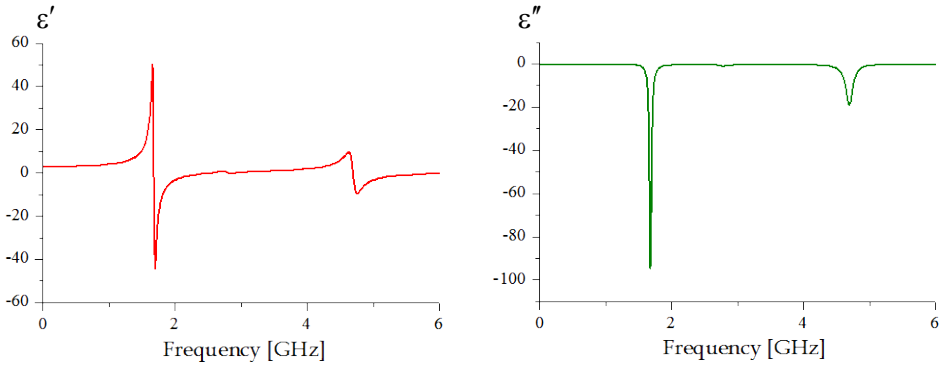

Figure 2.9 Anomalous dispersion for the electric permittivity introduced by standard TR inversion technique.

Once the algorithm has been tested with the previus reference cases, it has been applied to the characterization of real-life MTMs based on inclusions. The nature of the implants varies with respect to the desired electromagnetic response. Commonly, at microwaves, the electric

permittivity tailoring is related to structure containing wires or elongated metallic particles, excited by the electric field and capable of sustaining plasmonic response at moderately low frequency [6]. The permeability is tuned by inserting metallic loops like split-ring resonators (SRRs), spiral resonators (SR) and similar inclusions in the host matrix [7].

A metamaterial sample constituted by a plane array of artificial magnetic inclusions has been the considered. The unit cell is formed by a square spiral resonator (SR) with external length l = 8 mm. The scattering coefficients have been acquired by simulating the structure with the previous boundary conditions. A Lorentz dispersion model for the permeability and a constant value permittivity have been introduced, assuming only a magnetic response for this king of implant. All the unknown parameters have determined by the algorithm managing the de-embedding of the spectra to the virtual reference planes. The results are shown in Figure 2.10

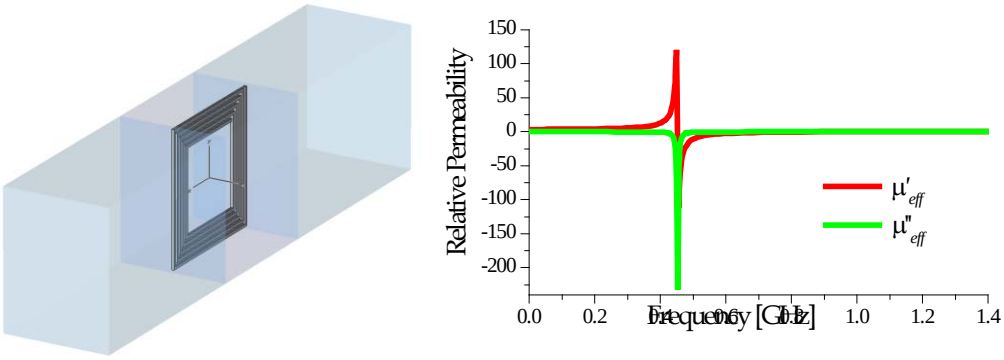

Figure 2.10 MTM unit cell based on single SR (left); retrieved permeability function (right).

Looking at the reconstructed spectra of Figure 2.11, it is quite clear that the extracted effective permeability consistently describes the samples under the working hypothesis, showing results in good agreement with the behaviour of the inclusion predicted by other analytical models [35]. On the contrary, by using usual TR we obtain a varying electric permittivity with anomalous dispersion.

The same approach may be used for other resonating inclusions with similar results.

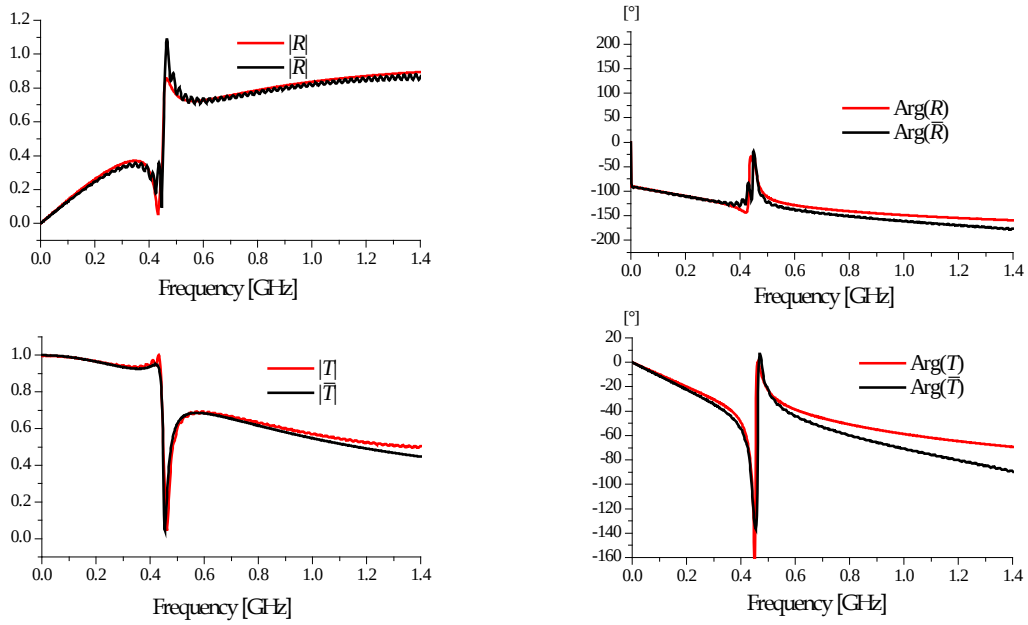

Figure 2.11 Simulated and reconstructed scattering coefficients for the SR based MTM.

In order to improve the overall procedure, the code has also been extended and optimized by employing genetic algorithm. A Non-dominated Sorting Genetic Algorithm (NSGA-II) has been introduce using Matlab® libraries [36]. The initial population is calculated from the known parameters of the configuration. A multiple ring resonator has been used as unit cell, with an external size of length l = 4 mm, an inner separation between the rings of 0.1 mm and two identical gap of 0.1 mm. The metallization is supposed to have a width of 0.1 mm and a thickness of 10^{-3} mm. Results are shown in Figure 2.12, confirming the reliability of the proposed approach.

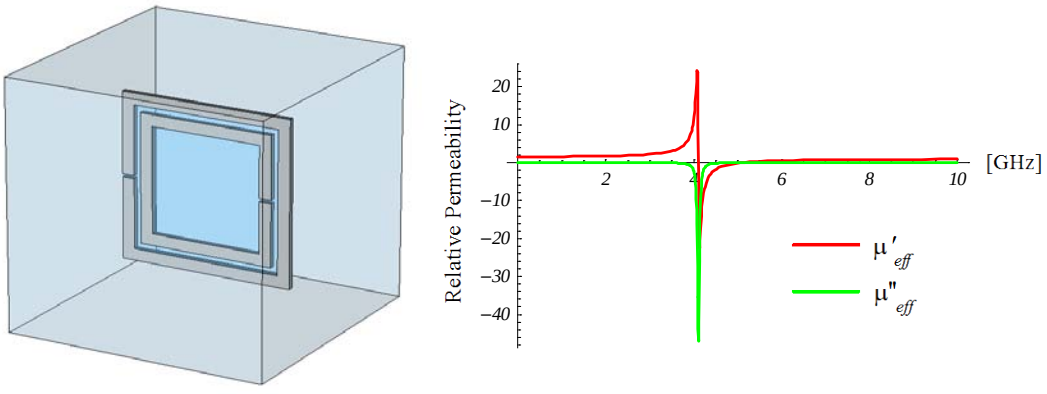

Figure 2.12 MTM unit cell based on a multiple ring resonator (left); retrieved permeability function (right).

Finally, the algorithm has been tested to evaluate the transition from thin to bulky MTMs composed by different layers of inclusions. In order to simulate a realistic scenario, a multiple ring implant has been embedded in a FR4 substrate ($\varepsilon_r = 4.4$). The metallization has been modeled through lossy copper with a strip width of 0.85 mm and thickness of 0.018 mm. The major size of the ring is 7 mm, with an inner gap of 0.6 mm, as shown in Figure 2.13 (left panel). Different layers of inclusions have been packed ans simulated extracting the respective parameters.

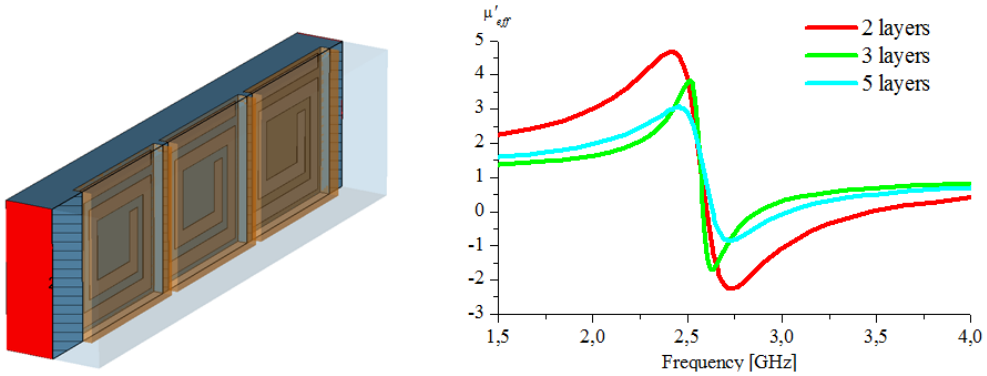

Figure 2.13 Bulky MTM parameters extracted through the optimized inversion procedure.

As reported in Figure 2.13 (right panel), the extracted permeabilities collapse through a slight transition to a similar dispersion profile. As anticipated, a small attenuation is observed when increasing the layer number, due to the losses present in the configuration. However the main characteristics of the resonant model are consistently retrieved by the algorithm, thus providing an useful design tools for several applications.

3. CLOAKING AND OPTICAL FORCES

3.1 Metamaterials in cloaking applications

Recently, the possibility to synthesize properly engineered cloaks of invisibility in a given frequency range has determined a growing interest in the study of induced transparency and low scattering phenomena. Several groups worldwide have proposed alternative solutions [37-53] based on really different physical mechanisms, such as anomalous localized resonances [37], coordinate transformations [38-42], or scattering cancellation [43]. As reported in [44-45], each technique shows advantages but also intrinsic limitations. For instance, the theoretical approach based on the coordinate transformation, which is very elegant from the mathematical and physical point of views, works quite well even for large objects, and is independent of the object to cloak, may find some problems at the fabrication stage, due to the employment of the reduced parameters and to the inhomogeneity of the cloak material. Nevertheless, some experiments have been already conducted with a certain degree of success. As for any metamaterial design, anyway, losses play an important role, as these experiments clearly reveal [39]. Apart from these difficulties, even from the fundamental point of view there are some problems, especially if we are interested in cloaking devices working not only at a single frequency. In the coordinate transformation approach, in fact, the paths of the electromagnetic field circumventing the object are covered with a phase velocity which is greater than the speed of light. Anyway, when a pulsed electromagnetic field impinges on the object covered with the cloak, since the group velocity does not excides the speed of light, the resulting cloak cannot have the desired functionality over a broad range of frequencies, even if we are able to realize broadband metamaterials. On the other hand, as it is well known from the microwave circuit theory, losses are inherently related to any impedance transformation, even in the case of continuous transformation. For this reason, cloaks based on this approach must be quite large in order to have a very smooth variation of the parameters and reduce the losses as much as possible. Also the approach based on plasmonic materials proposed in [43] is characterized by advantages and drawbacks.

One limitation is that this technique is, to some extent, object-dependent. Another potential drawback of this approach resides in the dimensions of the objects that can be cloaked. Even if the approach as such works for electrically small objects, recently some results have been presented showing how it is possible to increase the object dimensions [45-46]. As to the losses, this approach has the important advantage of employing homogeneous materials (i.e. there is no need to synthesize an electric/magnetic profile) possibly having a real part of the permittivity close to zero. Looking at the dispersion of the material, in fact, since the operation frequency is close to the plasma frequency and far away from the resonance of the inclusions, losses can be assumed as rather low. In addition, the dispersion curve close to the plasma frequency has a slow slope and, thus, this approach is characterized by relatively good performances in terms of bandwidth. Moreover, from the fabrication point of view, this approach leads to easier practical designs as compared to the one based on the coordinate transformation. However, some problems arise when we try to use this approach for devices working in both polarizations. When trying to implement this setup at microwaves is indeed difficult to obtain such behavior with real-life inclusion-based cover. Another important issue is how to move towards optical frequencies using the same basic idea. Extend the cloaking approach proposed in [43] to the visible regime, some limitations should be addressed. At these frequencies, in fact, there is a lack of useful natural materials exhibiting the required permittivity. As previously anticipated, for materials characterized by a close-to-zero real permittivity, the plasma frequency should rest in the visible. Unfortunately, noble metals, such as gold and silver, have plasma frequencies at smaller wavelengths in the ultra-violet regime and, thus, exhibit a strong plasmonic (i.e. the real permittivity is strongly negative) behavior in the visible.

3.1.1 Cloaking devices at Microwaves

Before considering the electromagnetic formulation of the problem, it is important to define a suitable figure of merit in order to evaluate the effective performances of a cloaking device based on scattering cancellation

technique, especially when comparing the proposed technique with other reliable approaches.

When studying the propagation of a plane wave in presence of an obstacle we refer to the total field as a superposition of two electromagnetic field: the incident field $\mathbf{E}_i$ (that is the impinging field in absence of the obstacle) and the scattered field $\mathbf{E}_s$ (generated by the scatterer) [53-55]. As figure of merit for the analysis of the electromagnetic problem we introduce the Scattering-Cross-Section (SCS, σ). In plane wave scattering, the SCS is defined as the area intercepting an amount of power that, when scattered isotropically, produces at the receiver a density that is equal to the density scattered by the actual target [53-54]. For two-dimensional objects we denote the SCS as σ_{2D}, while for three-dimensional objects we refer to σ_{3D}, in formulas

$$\sigma_{2D} = \begin{cases} \lim\limits_{\rho\to\infty}\left[2\pi\rho\dfrac{|\mathbf{E}_s|^2}{|\mathbf{E}_i|^2}\right] \\ \lim\limits_{\rho\to\infty}\left[2\pi\rho\dfrac{|\mathbf{H}_s|^2}{|\mathbf{H}_i|^2}\right] \end{cases}, \qquad \sigma_{3D} = \begin{cases} \lim\limits_{r\to\infty}\left[4\pi r^2\dfrac{|\mathbf{E}_s|^2}{|\mathbf{E}_i|^2}\right] \\ \lim\limits_{r\to\infty}\left[4\pi r^2\dfrac{|\mathbf{H}_s|^2}{|\mathbf{H}_i|^2}\right] \end{cases}.$$

Since the total scattering cross-section of an object is given by the sum of the absorption cross-section and the scattering cross-section, and the forward scattering amplitude is related to the total cross-section of the scatterer through the application of the optical theorem [55], it is straightforward to analyze the cloak response just considering the reduction of the scattering cross-section of the covered object.

Usually, the analytical solutions of the scattered electromagnetic field found in some reference geometries, such as the spherical or cylindrical ones, allow a closed form calculation of the SCS associated to structure. This quantity represents, indeed, an effective parameter to evaluate and compare the cloak responses.

Let us consider, for example, some canonical geometries as the cylindrical one depicted in Figure 3.1. We may individuate two fundamental polarizations, depending on whether or not the electric or magnetic field lies along the cylinder axis. As firstly investigated in [43], by knowing the radius and the constitutive parameters of the object, it is possible to

synthesize an optimal cover capable of significantly reduce the scattered field in the operating polarization. In particular, the condition at which the amplitude of the main dipolar scattering contribute reduces to zero relates the ratio between the radius of the object and the radius of the cylindrical shell with the constitutive parameters of both the object and the cloak. Thus, by engineering the cloak response through its effective parameters, we are able to design a device working in both the polarizations.

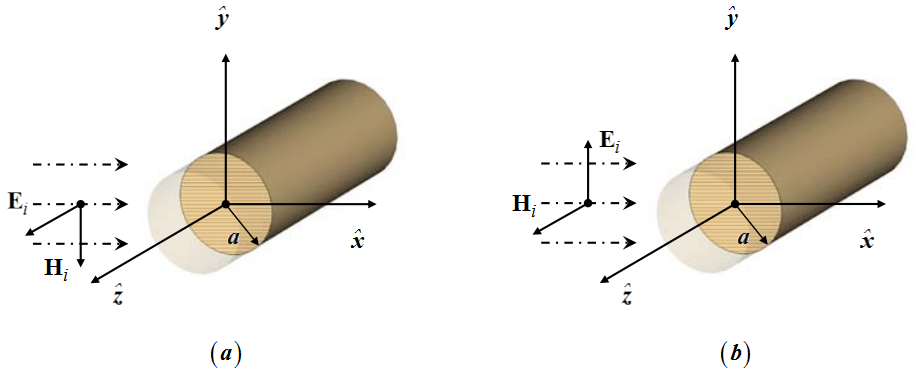

Figure 3.1 A schematic illustration of geometry under analysis. TM polarization incidence (a) and TE polarization incidence (b) for an infinite cylinder of radius *a*.

The results derived for the infinitely long cylindrical structure are indeed valid also in the case of a finite length cylinder, being, in first approximation, the scattering cross-section of the finite length cylinder proportional in the far-field region to the one of the unbounded cylinder through its effective length [53-55].

In this case, the SCS depends on the polarization we consider, but for high symmetrical setup (like in the spherical case) it globally describes the scattering behavior of the structure.

For dielectric object it is sufficient to design a cover with only a proper effective permittivity, but if the object has magnetic properties it is necessary to synthesize also the requiredd permeability. Let us consider the object to have a length $L = 50\,mm$ a radius $a = 10\,mm$ and constitutive parameters $\varepsilon = 2\varepsilon_0,\ \mu = 2\mu_0$. The design frequency is assumed to be $f_0 = 3\,GHz$ and the shell radius $b = 1.8\,a$. Following the procedure presented in [43], in the TE case the numerical minimization of the scattering cross-section can be obtained using a cloak made of an ideal homogeneous

material with the following set of constitutive parameters: $\varepsilon_c = 1, \quad \mu_c = 0.1$. The cloak is then made of a Mu-Near-Zero (MNZ) metamaterial, as the dual counterpart of the Epsilon-Near-Zero (ENZ) material that can be used for purely dielectric objects [43]. By duality, in the other polarizations we get similar results, so the main issue is to synthesize a cover whose response in terms of effective parameters satisfies the theoretical design parameters in both the polarizations. The most effective solutions is to achieve the desired value of permeability for the cover by using magnetic inclusions. Following the design presented in the previous Chapter, spiral resonators (SRs) may be straightforwardly used to obtain the required effective material. The high miniaturization rate of SRs assures that inclusion may be designed not only to obtain the desired value of permeability at the cloaking frequency, but also to properly fit the cover thickness. By radially placing the SRs in the cover and optimizing the design (Figure 3.2) we obtain a significant reduction of the SCS, as reported in Figure 3.3.

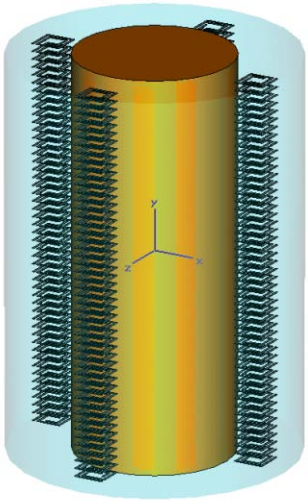

Figure 3.2 Cylinder surrounded by four columns of SRs implementing the MNZ cloak. Figure contained in Reference [50].

In order to obtain a cloaking device working for both TM and TE polarizations, we should mix up the previous design with the one already proposed in [49] for the TM polarization. This latter is based on the employment of the parallel plate medium, which consists of metallic plates extended along the axis of the cylinder and radially placed all around the object. Simulations were performed with full wave simulator introduced in the previous Chapter [32]

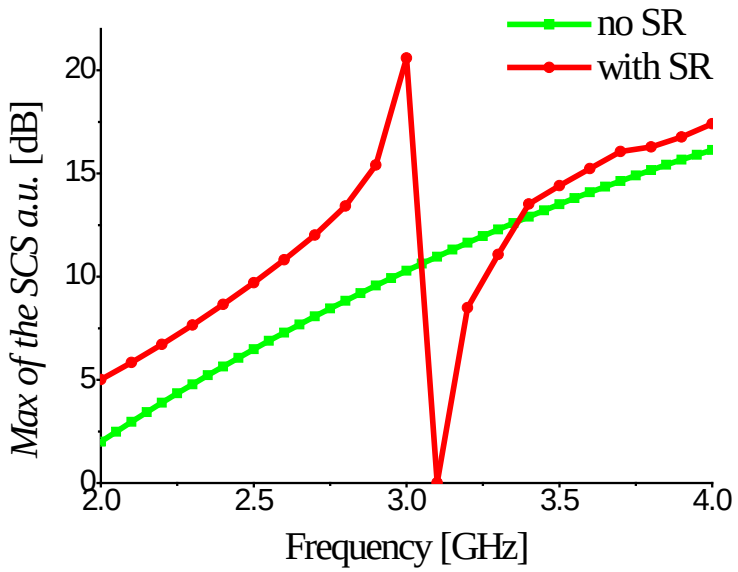

Figure 3.3 Maximum of the scattering cross-section (SCS) of the bare and covered cylinder versus frequency. Figure contained in Reference [50].

This material may match the behavior of the required ENZ material. In order to host the inclusions of the magnetic kind, working for the TE polarization, in the layout based on the parallel plate medium and working for the TM polarization, it is necessary to reduce the number of the plates to leave room to the SRs.

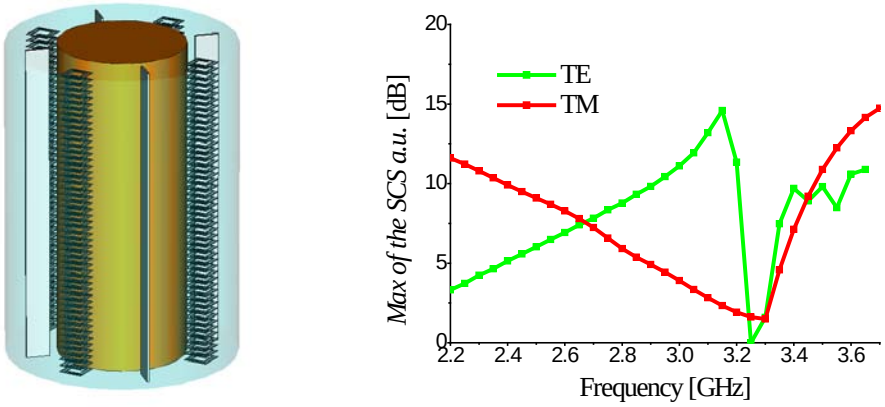

Figure 3.4 Sketch of the layout of a cylindrical cloak working for both TE and TM polarizations (left). Maximum of the scattering cross-section (SCS) for both TE and TM polarizations (right). Figure contained in Reference [50].

The TE polarization layout can be easily merged with a TM polarization cloak made of just four plates, as it shown in Figure 3.4. As shown in [50], the this design is quite effective and provide also a certain robustness in terms bandwidth. This approach may be also extended to work at multiple frequencies, as investigated in [56]

3.1.2 Cloaking devices at Optical Frequencies

When applying the procedure described in [43] for the design of actual cloaks working at optical frequencies, the main difficulty is represented by the synthesis of an artificial material with a plasma frequency laying in the visible in order to get at those frequencies either an ENZ behavior or a moderately negative value of the real part of the relative permittivity. Even if the parallel plate mediuam has been extended also to the visible regime [52], a complete design of the electromagnetic response ot the cover for arbitrary geoemntries is not possible.

In order to overcome such a limitation, we may use the layered medium presented in [57] for a different application and in the case of a planar configuration. By stacking two different material slabs, if the thicknesses of the slabs are electrically small, it is shown in [58-59] that the resulting composite material is described through constitutive parameters which depend only on the ratio between the thicknesses of the two slabs and the constitutive parameters of the two different materials.

Now, let's suppose we want to cloak a cylindrical object with given permittivity and permeability (ε_{obj},μ_{obj}). Extending the formulation proposed in [57] to the case of the cylindrical geometry, we may have the two configurations depicted in Figure 3.5.

When moving from the planar geometry to the cylindrical one, in fact, it is possible to stack the two materials in two different ways. In both cases, the resulting composite material is anisotropic and the expressions of the entries of the permittivity tensor are given in the insets of the figure.

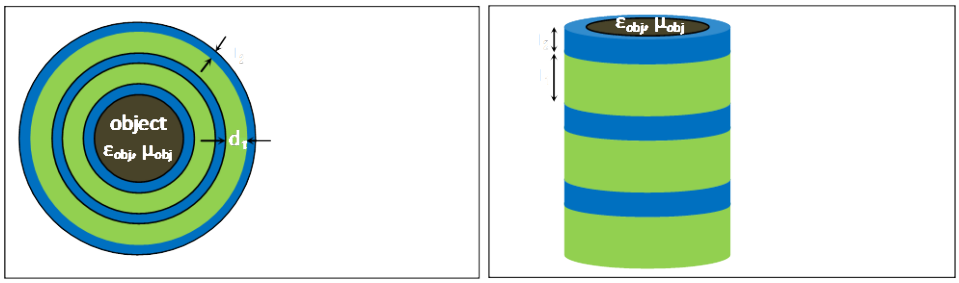

a) b)

Figure 3.5 a) Cylindrical cloak made of concentric shells of different materials. b) Cylindrical cloak made of stacked disks of different materials. Figure contained in Reference [51].

Depending on the polarization of the impinging wave and on the frequency range of interest, the designer can use either of the two configurations depicted in Figure 3.5. Particularly, in order to get the desired value of the relative permittivity, the designer can count on a few degrees of freedom: the geometric parameters (i.e. the thicknesses of either the concentric shells or the slices in Figure 3.5 *a* and *b* respectvely) and the dispersive parameter behaviors of the two materials.

If we are interested in the design of an ENZ cloaking device at visible frequencies, the main problem is represented by the fact that typical plasmonic materials (e.g. nobel metals) exhibit relatively high plasma frequencies. If the impinging wave is TM polarized (i.e. the electric field is along the axis of the cylinder), looking at the expression of the longitudinal effective permittivity in the insets of Figure 1, it is clear that the configuration obtained by vertically stacking different material slices does not permit an easier implementation of an effective ENZ material in the visible. This configuration, in fact, has an effective relative permittivity dominated by the lower term, requiring that one of the two materials must have a relative permittivity less than one.

On the other hand,using a cylindrical cover made of concentric shells, the axial component of the permittivity tensor can be properly designed in order to have an ENZ behavior in the visible. If the two materials are a plasmonic material like silver (Ag) and a non-plasmonic material like silica (SiO_2), it is possible to obtain a close-to-zero real permittivity along the axis of the cylinder at optical frequencies simply by choosing the proper value for the ratio η between the thicknesses of the shells made of the two different materials. Exploiting this configuration, thus, it is now possible to

apply the formulation presented in [43] to reduce the total scattering cross-section (SCS) of a covered cylindrical object for the case of the TM polarization. Let's consider a dielectric cylinder of radius a = 50 nm with relative parameters $\varepsilon_{obj} = 2\varepsilon_0$, $\mu_{obj} = \mu_0$ and a length L = 500 nm illuminated by a plane wave with the electric field directed along the axis of the cylinder (Figure 3.6a). Following the theoretical procedure presented in [43,49,52], it can be numerically found that, in order to reduce the scattering cross-section of the cylinder at the design frequency f = 600 THz, an ideal homogenous non-magnetic ($\mu_c = \mu_0$) metamaterial cover shell with a radius $b = 1.8\,a$ should have a relative permittivity $\varepsilon_c = 0.32\varepsilon_0$. In this case, the ideal reduction of the SCS of the covered cylinder in comparison to the case of the bare cylinder is 14 dB. Applying, now, the design formulas presented in the inset of Figure 3.5 for the case of SiO_2-Ag concentric layers, the desired value of the effective permittivity ($\varepsilon_c = 0.32\varepsilon_0$) at the frequency f = 600 THz is obtained with a thickness ratio $\eta = 0.21$. The dispersion values for the materials used in this configuration are the same measured in literature [60,61]. Given that the thickness of the cloak is limited by the radial value b and the ratio $d_2/d_1 = \eta$ is now fixed, the choice of d_1 can be made in order to fill the cover with a sufficient number of concentric shells, according to the homogenization requirements. A layer of SiO_2 with d_1 = 10 nm is enough to obtain the desired dispersion near the working frequency (see Figure 3.7a), allowing the expected SCS reduction (see Figure 3.7b). The numerical results presented in Figure 3.6b and all the other results presented in the following are obtained through full-wave numerical simulations.

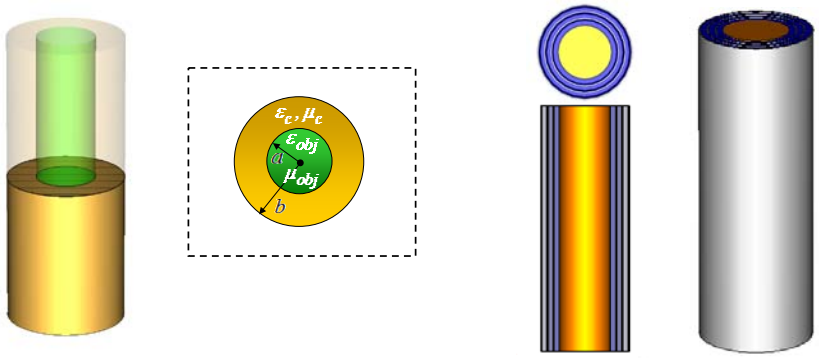

Figure 3.6 a) Cylinder surrounded by an homogeneous cover. b) Cylinder surrounded by a cloak made of concentric shells of different materials. Figure contained in Reference [51].

The reduction of the object observability around the desired frequency is quite evident. As expected, before the plasma frequency the observability of the object is partially increased due to the strong plasmonic behavior of the Ag, while at higher frequencies the SCS of the covered object approaches the one of the bare cylinder.

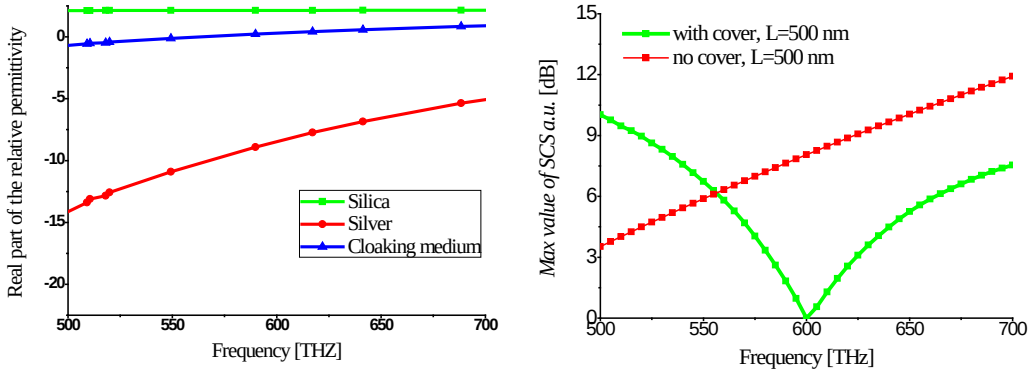

a) b)

Figure 3.7 a) Real part of the permittivity of Ag, SiO_2 and of the cloak effective medium (z-component). The cloak is designed for f = 600 THz and the thicknesses of the two material (Ag and SiO_2) shells are, 2 nm and 10 nm, respectively. b) Maximum total scattering cross-section of a cylindrical object (L = 500 nm, a = 50 nm, $\varepsilon_{obj} = 2\varepsilon_0$, $\mu obj = \mu_0$) with and without the cloak. Figure contained in Reference [51].

In the frequency range of interest, Ag has relatively high losses. This explains the fact that the reduction of the SCS obtained in Figure 3.7b is only *9 dB* instead of the approximately *14 dB* expected from the theoretical calculations involving an ideal, lossless, unbounded and homogeneous cover. If we plot the ratio between the SCS of the bare cylinder and the one of the cylinder covered with an ideal cover as a function of the imaginary part of the cover relative permittivity ε_c'', we obtain the graph reported in Figure 3.8. The reduction of the SCS in presence of the actual losses of the real-life layered material can be easily estimated from this graph.

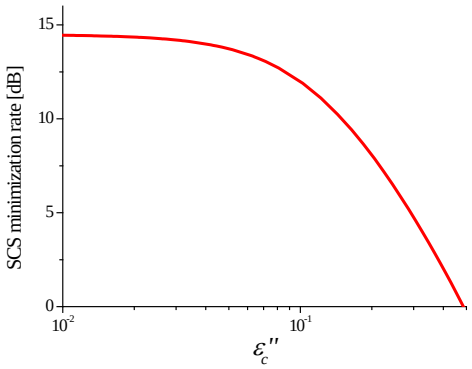

Figure 3.8 Variation of the ratio between the SCS of the bare cylinder and the one of the cylinder covered with an ideal, lossy, homogenous material, as a function of the imaginary part of the relative permittivity of the cover material. The real part of the permittivity is kept at the design value and the frequency is f = 600 THz**.** Figure contained in Reference [51].

The pattern of the SCS in linear units reported in Figure 3.9, clearly shows that the dominant scattering term for the bare cylinder is basically the dipolar one, due to its electrically small dimensions. Applying the layered cover, instead, the dipolar term is almost suppressed and the main contribution is given by an higher-order scattering mode.

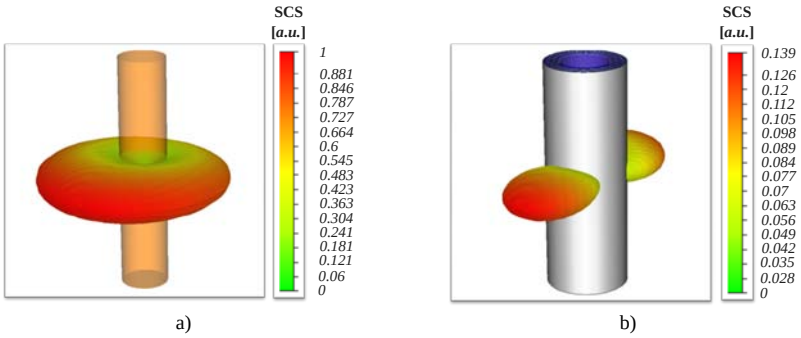

Figure 3.9 Scattering cross-section of the bare cylinder. b) Scattering cross-section of the cloaked cylinder. Figure contained in Reference [51].

Looking at the bi-dimensional plots of the electric and magnetic field amplitude distributions at the cloak frequency (Figure 3.10 and Figure 3.11), the shadow effect is well evident in the case of the bare cylinder, while in the covered case it is visibly reduced.

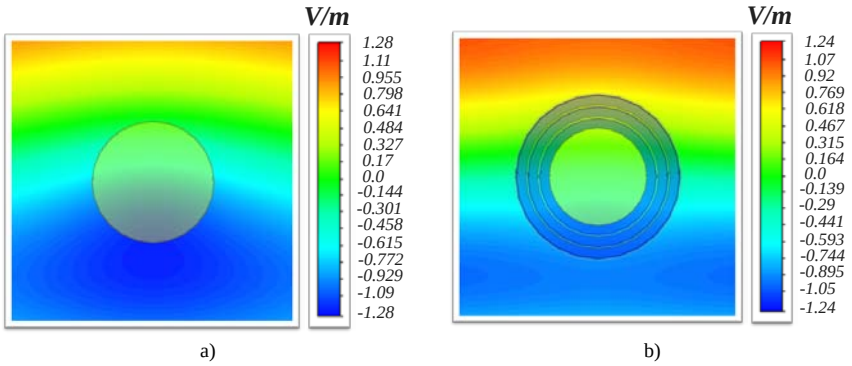

Figure 3.10 Electric field amplitude at the cloak frequency f = 600 THz in the case of the bare cylinder (a) and in the case of the cylinder with the cloak (b). Figure contained in Reference [51].

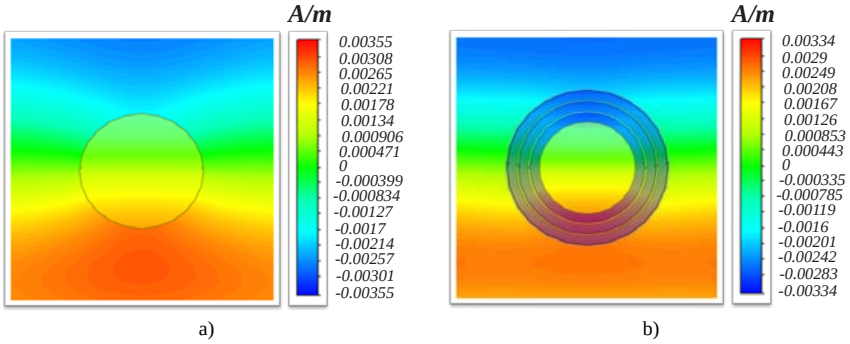

Figure 3.11 Magnetic field amplitude at the cloak frequency f = 600 THz in the case of the bare cylinder (a) and in the case of the cylinder with the cloak (b). Figure contained in Reference [51].

The shadow reduction can be clearly appreciated in Figure 3.12 where the isolines of the magnetic field at the cloak frequency for the bare cylinder and the cloaked one are shown. While in the first case the field lines are deformed by the presence of the obstacle, in the second one they are more similar to the field lines of a plane wave travelling unaltered through the object.

The same approach can be used to cloak also an object with magnetic properties. Even if in the visible regime there are no natural materials exhibiting a magnetic response, it is, indeed, useful from a theoretical point of view to extend the same idea also to such materials.

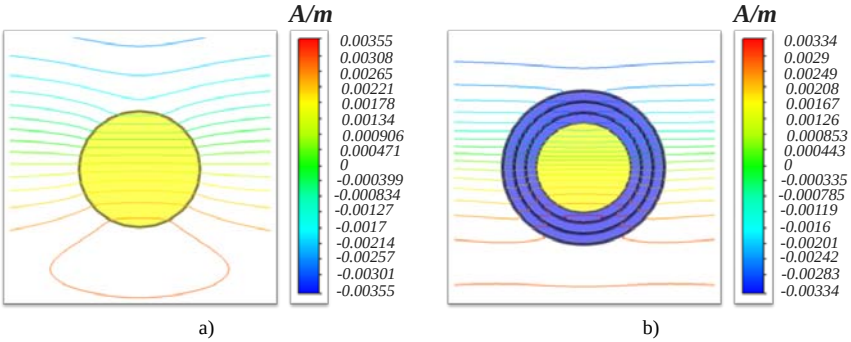

Figure 3.12 Isolines of the magnetic field amplitude at the cloak frequency f = 600 THz in the case of the bare cylinder (a) and in the case of the cylinder with the cloak (b).

Let's consider now a cylinder of radius a = 50 nm and length L = 800 nm with constitutive parameters $\varepsilon_{obj} = 2\varepsilon_0$, $\mu_{obj} = 2\mu_0$, always illuminated by a TM-polarized plane wave with the electric field directed along the cylinder axis. Again, using the previous numerical procedure, it is easy to find out that an ideal homogenous dielectric cover shell ($\mu_c = \mu_0$) with the same radius $b = 1.8\,a$ and relative permittivity $\varepsilon_c = 0.1\varepsilon_0$ should be able to sensibly lower the SCS of the structure. In this configuration, using the same layer of SiO_2 with d_1 = 10 nm and Ag as the plasmonic material, the optimal value for the thickness ratio is $\eta = 0.21$. In Figure 3.13 it is shown the maximum of the SCS as a function of the frequency for the proposed cylinder with and without the cover. Even in this case, the reduction of the object SCS near the design frequency is quite evident.

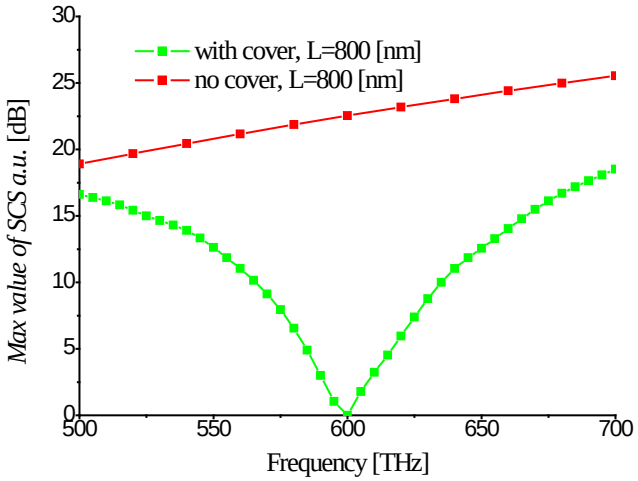

Figure 3.13 Maximum of the SCS of a cylindrical object (L = 800 nm, a = 50 nm, $\varepsilon_{obj} = 2\varepsilon_0$, $\mu_{obj} = 2\mu_0$) with and without the cloak.

Due to the inherent anisotropic behavior of the layered medium (e.g. we cannot have the same values for the diagonal elements of the permittivity

tensor), it is impossible to have a cloaking device working for both TM and TE polarizations at the same frequency. In the case of spherical layered structures, we could consider two different ways to stack the two materials. One possibility is to use concentric spherical shells and the other one is to use a stack of annular circular slices following the profile of the sphere. Anyway, the first setup is only suited for an impinging wave having a radial electric field. For this reason, in this paper, we propose to employ the second setup, which exhibits a given effective permittivity along the electric field direction of a TM-polarized impinging wave.

In the design reported in Figure 3.14b, we have, accordingly, stacked the different material slices along the direction orthogonal to the incident electric field. The operation of such configuration is substantially independent from the electric field direction in the plane of the layers, while we expect that the cloak should not work for the orthogonal polarization.

Figure 3.14 a) A spherical particle surrounded by an homogeneous cover. b) A spherical particle covered with a cloak made of stacked layers of different materials.

Let's consider a spherical particle made of Ag (whose dispersion was previously shown in Figure 3.7b) with radius a = 50 nm. Again, we use the homogeneous cover approach in order to synthesize a spherical shell with a proper permittivity value.

For an homogenous dielectric ($\mu_c = \mu_0$) spherical shell with radius $b = 1.8\ a$ working at the frequency f = 600 THz the required relative permittivity is $\varepsilon_c = 0.5\varepsilon_0$. Applying the design formulas reported in the inset of Figure 3.14b and using again alternating layers of SiO_2 with thickness d_1 = 10 nm and Ag, the optimal value for the thickness ratio is found to be $\eta = 0.2$. In Figure 3.15 it is shown the maximum of the SCS of the Ag spherical shell with and

without the cloak. Again, the observability of the object has been reduced at the design frequency by putting the cloak on.

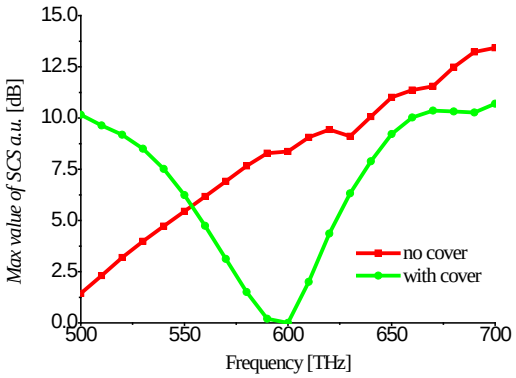

Figure 3.15 a) Maximum of the SCS of a silver spherical particle (a = 50 nm) with and without the cloak as a function of frequency. Figure contained in Reference [51].

The sensitivity of the cloaking device with the variations of the geometrical parameters is shown in Figure 3.16. As expected, a reduction of the ratio between the layer thicknesses corresponds to a lower-shift of the cloak operation frequency. Since the permittivity of SiO_2 is almost constant with the frequency, in fact, when lowering η, a higher (negative) value of the permittivity is required. The needed value can be found in the Ag dispersion at lower frequencies.

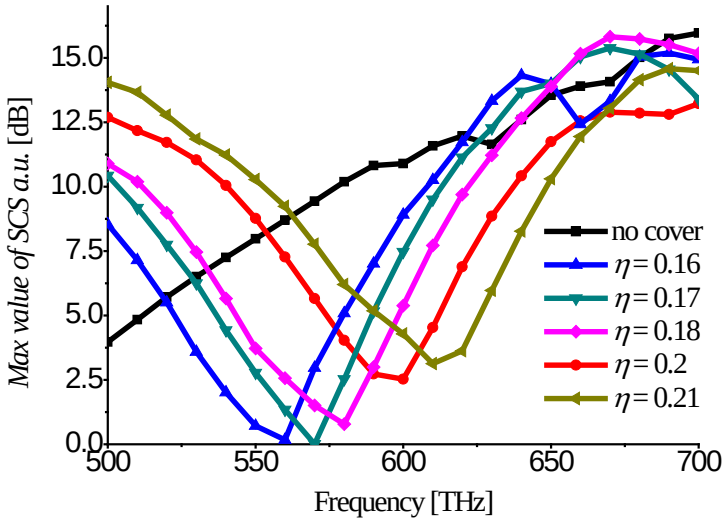

Figure 3.16 Maximum of the SCS of a silver spherical particle (a = 50 nm) with and without the cloak as a function of frequency for different values of the ratio η. Figure contained in Reference [51].

As previously anticipated, the proposed setup is clearly independent from the orientation of the electric field in the plane of the layers, while it expected not to work when the electric field is orthogonally directed with respect to the layers.
In Figure 3.17, we present the SCS of the same spherical particle used in the previous examples for differently polarized incident plane waves. When the electric field is orthogonal to the layers, the cloaking effect disappears, because the effective permittivity seen by the impinging wave (i.e. the orthogonal component of the permittivity) does not match the design value. In addition, since this permittivity is greater than ε_0, the total SCS is even bigger than the one of the bare silver sphere.

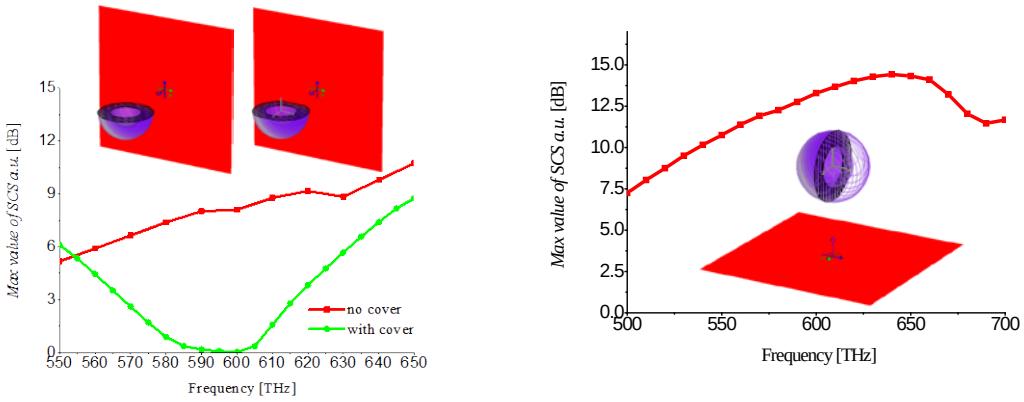

a) b)

Figure 3.17 a) Maximum of the SCS of a spherical silver particle (a = 50 nm) with and without the cloak for an impinging plane wave with the electric field parallel to the layers. b) Maximum of the SCS of the same particle with the same cloak for an impinging plane wave with the electric field orthogonal to the layers. Figure contained in Reference [51].

The SCS pattern obtained in the case of an impinging wave with the electric field parallel to the layers at the design frequency is reported in Figure 3.18. The SCS reduction is rather evident, as can be easily remarked by the scale ranges.

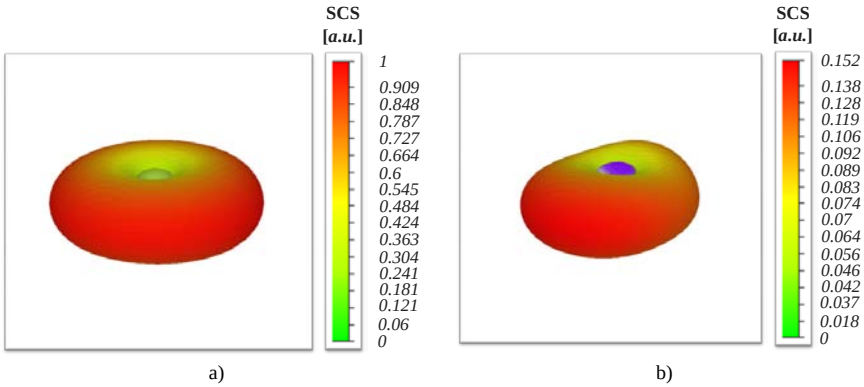

Figure 3.18 SCS of the bare sphere at the cloak frequency f = 600 THz. b) SCS of the cloaked sphere at the same frequency. In both cases the impinging wave is polarized such that the electric field is parallel to the layers. Figure contained in Reference [51].

The maps of the electric and magnetic field amplitude distributions at the design cloak frequency are reported in Figure 3.19 and Figure 3.20. From these graphs, it is well evident that in the case of the covered sphere the fields are noticeably less perturbed.

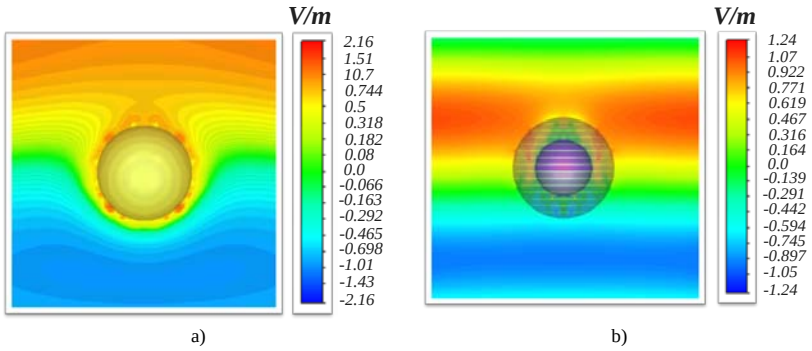

Figure 3.19 Electric field amplitude at the cloak frequency f = 600 THz in the case of a bare sphere. b) Electric field amplitude at the cloak frequency f = 600 THz in the case of a sphere with cloak. Figure contained in Reference [51].

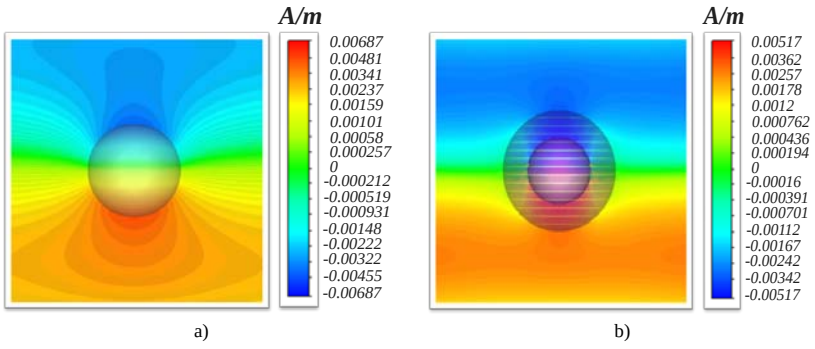

Figure 3.20 Magnetic field amplitude at the cloak frequency f = 600 THz in the case of a bare sphere. b) Magnetic field amplitude at the cloak frequency f = 600 THz in the case of a sphere with cloak. Figure contained in Reference [51].

The reduction of the shadow effect is easily observed in Figure 3.21, showing the isolines of the magnetic field at the cloak frequency for both the bare sphere and the cloaked one.

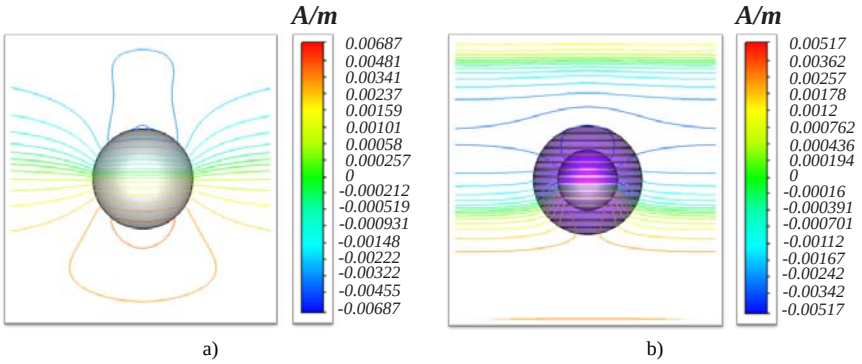

Figure 3.21 a) Isolines of the magnetic field amplitude at the cloak frequency f = 600 THz in the case of a bare silver sphere. b) Isolines of the magnetic field amplitude at the cloak frequency f = 600 THz in the case of a silver sphere with cloak. Figure contained in Reference [51].

The analytical formulations used to design plasmonic cloaks, however, have always assumed in the literature, for simplicity, that the object to be cloaked has a canonical and symmetrical geometry. On the other hand, transformation-based cloaking has seen a relevant number of extensions to arbitrarily shaped objects and cloaks [62-64]. This has generated some confusion in the recent literature, with papers on the topic claiming that the use of a spherical plasmonic cloak may not be successfully employed to hide an irregular or anisotropic shape. The inherent nature of the plasmonic cloaking technique, which is based on a scattering cancellation mechanism, obviously requires that, in order to suppress the scattering response of an anisotropic object, simultaneously at all different angles and polarizations, the cloak should be appropriately designed with an asymmetric and anisotropic shape, which was not considered, for instance, in [65].

It is indeed possible to envision plasmonic cloaks capable of suppressing the scattering of irregular and anisotropic shapes by properly optimizing not only its plasmonic properties, but also its shape and design. In the next Sections, we will investigate the performances of such plasmonic covers to operate at optical frequencies, both for regular shapes and for structures characterized by a strongly polarization-dependent anisotropic response to the illuminating electromagnetic field.

3.1.3 Extension of Scattering Cancellation Technique to Complex Shapes

In the Rayleigh approximation (electrically small objects), the scattering cancellation approach is associated with the suppression of the overall dipole moment by inducing a negative dipole moment in the cloak, which may compensate and cancel the scattering from the object [43]. As shown in [47], this approach is still valid for relatively larger objects, for which the Rayleigh approximation does not apply, since the same approach may be used to cancel any dominant multi-polar scattering order. When dealing with complex geometries and anisotropic scattering response, as shown in the following, the cover may still be designed to obtain an analogous behavior at the desired frequency, independent of the angle of incidence and polarization of the impinging fields. In fact, since this effect is volumetric, it is expected that even irregular shapes may be cloaked, as long as the response of the cloak is tailored to provide the proper (anisotropic) polarization effects.

In the long wavelength limit, a generally shaped object with anisotropic scattering properties may be compactly described by a polarizability tensor $\underline{\boldsymbol{\alpha}}$ [13] that relates the induced dipole moment vector to the impinging electric field vector: $\mathbf{p} = \underline{\boldsymbol{\alpha}} \cdot \mathbf{E}_0$. It is worth noticing that for many shapes of small scatterers, the polarizability tensor may be assumed to be uniaxial in the proper reference system, ensuring that, although the amplitude of the induced dipole moment may vary with the polarization of the local electric field, the induced dipole moment may be parallel to the electric field when lying along the three main axes of the scatterer. Under this assumption, it may be possible to define a scalar polarizability that depends on the polarization of the electric field along these three main directions.

Although the scattering from an irregular shape may not always be calculated analytically, we may easily relate its total scattering cross section, evaluated with numerical techniques, to the components of its polarizability tensor for three orthogonal illuminations. This would represent a complete description of the scattering properties of the object of interest as long as its scattering is dominated by the dipolar fields. In this limit, it is easily found that:

$$\alpha_{xx} = \frac{\sqrt{4\pi\sigma_{xx}}}{k_0^2}, \tag{3.1.1}$$

where α_{xx} is for example the polarizability component for electric field polarized along $\hat{x}$, σ_{xx} is the total scattering cross section for the same polarization and k_0 is the background wave number. By choosing three orthogonal polarizations of the impinging electric field, we can calculate numerically the independent elements of the polarizability tensor $\underline{\boldsymbol{\alpha}}$ for a given object.

In order to validate this approach, we have first calculated the far-zone scattering width of an electrically small dielectric sphere of radius *a* using a full-wave simulations [32]. In this case, given the spherical symmetry of the particle, the electric polarizability α_e is independent from the polarization of the electric field, so the scattering matrix reduces to the scalar σ_s. Then, we numerically integrated the calculated scattering width to compute σ_s, and we compared the polarizability obtained with (3.1.1) to the well known exact solution [54]:

$$\begin{aligned} \alpha_e^{sphere} &= 3V\frac{\varepsilon_r - 1}{\varepsilon_r + 2} \\ \sigma_s^{sphere} &= 4\pi k_0^4 a^6 \left(\frac{\varepsilon_r - 1}{\varepsilon_r + 2}\right)^2, \end{aligned} \tag{3.1.2}$$

in the limit $a \ll \lambda_0$ for a volume $V = 4\pi a^3/3$. As shown in Figure 3.22, the retrieved numerical values of α_e match the expected solution.

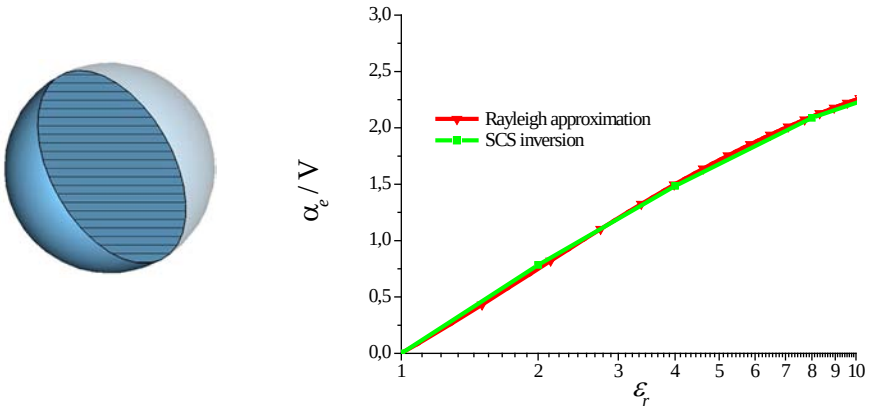

Figure 3.22 Retrieved normalized electric polarizabilty of a sphere as a function of its relative permittivity. Figure contained in Reference [47].

As suggested in [62], if we consider more complex shapes, such as regular polyhedral scatterers, it is easy to find that, due to their high symmetric spatial arrangements of faces, there is no substantially preferred direction, and thus their polarizabilities reduce to scalar quantities as well [62, 64]. Moreover, it is expected that for small dielectric contrasts the polarizability of these shapes should not sensibly differ from the one of a sphere with the same volume. Similar arguments justify the fact that the main factor in designing the proper plasmonic cloak is that its electrical volume may compensate the one of the object to produce an overall zero polarizability for the composite structure. In Figure 3.23, we show the ratio between the electric polarizabilties of a cube and a sphere with same volume, as a function of their relative permittivity, derived by applying the Method of Moments (MoM), as reported in [62,64]. It is evident that, due to the similar values of polarizability in the limit of electrically small particles, a plasmonic cover properly working for a sphere can be also used to cloak a cube, generally working also for different incidence angles. This is consistent with some of the results reported in [65].

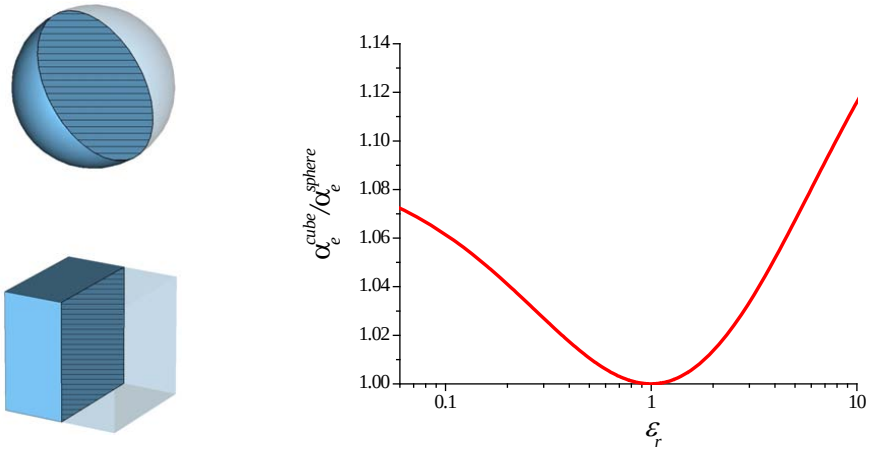

Figure 3.23 Ratio between the electric polarizabilties of a sphere and the one of a cube (with same volumes) as a function of their relative permittivity. Figure contained in Reference [47].

In order to extend these results to more asymmetric shapes, we first compare in Figure 3.24 the values of α_e derived by applying the MoM and SCS inversion for a cubic particle in the case of orthogonal incidence to one of the faces. In Figure 3.25, we consider the case of oblique incidence with

impinging wave vector $\hat{\boldsymbol{k}}_i$ lying along the diagonal of a cubic face (worst case scenario).

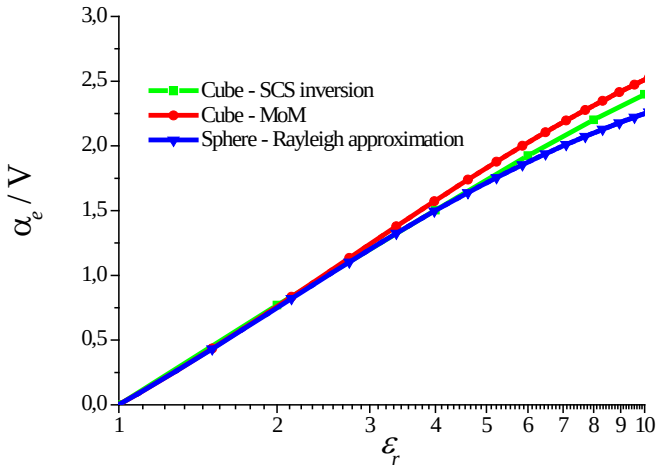

Figure 3.24 Electric polarizabilties for a cube (orthogonal incidence to one of the faces) and a sphere as a function of their relative permittivity. Figure contained in Reference [47].

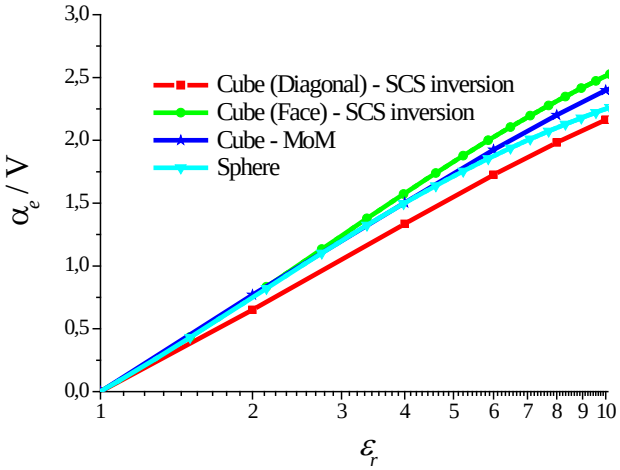

Figure 3.25 Electric polarizabilties for a cube and a sphere as a function of their relative permittivity. Figure contained in Reference [47].

As expected, the cube does not exhibit a strong anisotropic response, but the interesting point is that similar results may be obtained also for a more complex polyhedral shape, such as an octahedron. In this case, as reported

in Figure 3.26, the derived values of polarizability are very close to the ones obtained for a an isovolumetric cube.

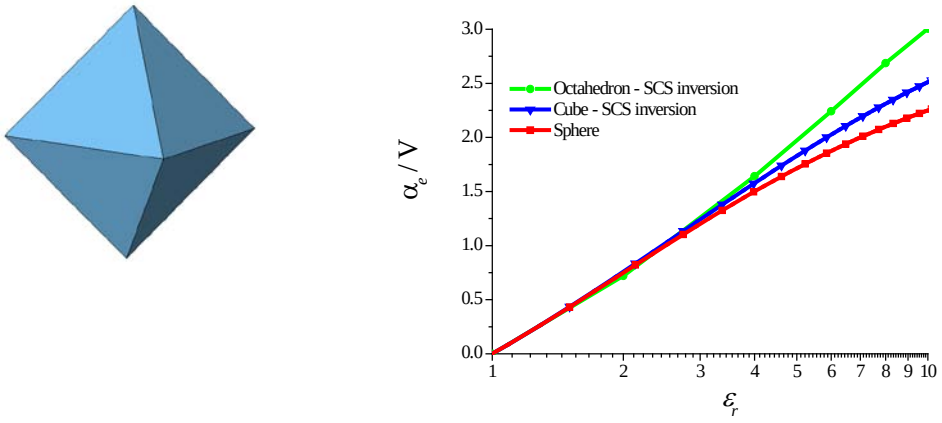

Figure 3.26 Electric polarizabilty for an octahedron as a function of their relative permittivity. Figure contained in Reference [47].

If we consider now a cone, we expect a substantially different response by changing the propagation direction of the impinging radiation. As shown in Figure 3.27, for weak scatterers (i.e. small dielectric contrasts), the electric polarizability is still comparable with the one of a bare sphere, but increasing the relative permittivity of the dielectric, the anisotropic behavior indeed may not be neglected.

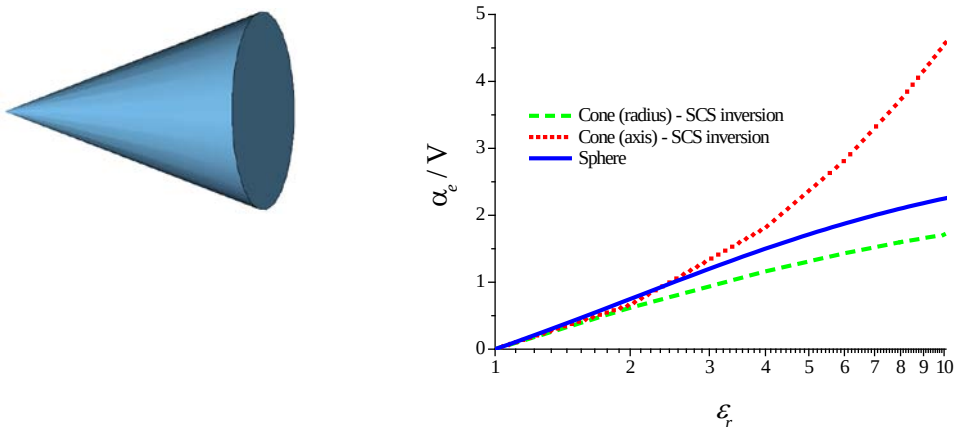

Figure 3.27 Electric polarizabilty for a cone as a function of its relative permittivity: impinging electric field directed along the axis (dotted red line), impinging electric field directed along the base radius (dashed green line). Figure contained in Reference [47].

An immediate consequence of the previous results is that we may be able not only to design a proper cover to cloak electrically small objects, but we may use a shell designed for a spherical geometry to properly work also for a different shape, as long as the electrical size of the object is small enough to ensure quasi-uniform field in the object. For larger objects, however, the situation is different and a wiser cloak design should be employed to make sure that the different polarizability of an anisotropic object for different field polarization is properly taken into account.

Let us consider a spherical silver particle of radius R of permittivity ε surrounded by a plasmonic cover with radius R_c (see Figure 3.28). As previously shown, we can easily find the relative permittivity of the cover to sensibly reduce the SCS of the structure. Assuming, for example, R = 50 nm and R_c = 1.8 R, we get for the external shell permittivity $\varepsilon_r \approx 0.5$ at 600 THz. Now, let us explore the possibility to cloak a cubic object. It is obvious that in the general case we cannot simply put a smaller cubic shape fitting the spherical core inside the cloak, as suggested in [65]. Following the previous analysis, in the quasi-static limit the same cloak may work only for a cube having similar physical volume as the sphere.

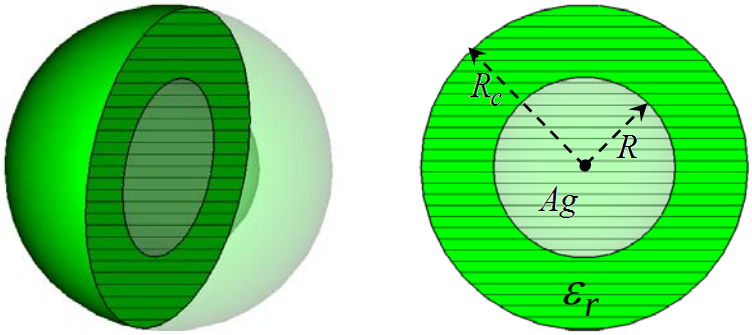

Figure 3.28 A silver sphere covered with a plasmonic shell. Figure contained in Reference [47].

In order to clarify this point, let us consider the asymptotic behavior of scattering coefficients in the quasi-static limit for a coated electrically small spherical object. Considering only the dipolar term in the Mie expansion [43] the total dipole moment of the overall system (core + cover) is suppressed if the following relation holds:

$$V(\varepsilon-1)+\frac{V_c}{3}(\varepsilon_r-1)\left(\frac{\varepsilon}{\varepsilon_r}+2\right)=0, \tag{3.1.3}$$

where V and V_c are the volumes of the inner particle and of the shell, respectively. Expression (3.1.3) is formally equivalent to the one derived for arbitrarily shaped cylindrical objects in [49] for the 2D case, introducing a condition on the ratio between the involved volumes and their dielectric contrasts, which is directly associated with the overall polarizability of the object and the cloak (3.1.1), consistent with the results reported in [43]. Since the transparency condition is based on a non-resonant volumetric phenomenon of cancellation of the induced electric dipole moments, following the previous results, it is expected that this same condition may be applied to non-spherical objects.

Consider for instance a cubic scatterer, as in Figure 3.29. Proper cloaking may be achieved by deforming the cloak shape to adhere conformably to the cubic surface, keeping the same filling factor as in Eq. (3.1.3), but preserving the shape of the hidden object, as depicted in Figure 3.29. This may ensure that, independent of the angle of incidence, the overall polarizability of the cube and the cloak are opposite to each other.

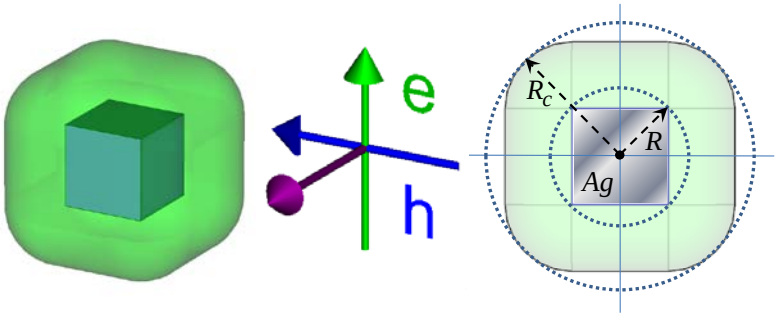

Figure 3.29 A conformal plasmonic cover for a silver cube. Figure contained in Reference [47].

Following these considerations, we have simulated a cloaked cube with same value of permittivity as in the spherical setup. The silver was modeled as a Drude dispersive material with losses [60,61]. As expected, we obtain similar performances at the design frequencies, resulting in a total scattering reduction of almost *14 dB* with respect to the case of the bare cube. In Figure

3.30, we have reported the 2D field maps, both in amplitude and phase, for the electric and magnetic field distribution. We have assumed here plane wave incidence from bottom to top with an electric field amplitude of $1V/m$. It is noticed that the field is identically restored with proper cloaking, both in amplitude and phase, and the electric field enhancement at the cube vertices, which is mainly responsible for the scattering in this case, are eliminated by the presence of the cloak.

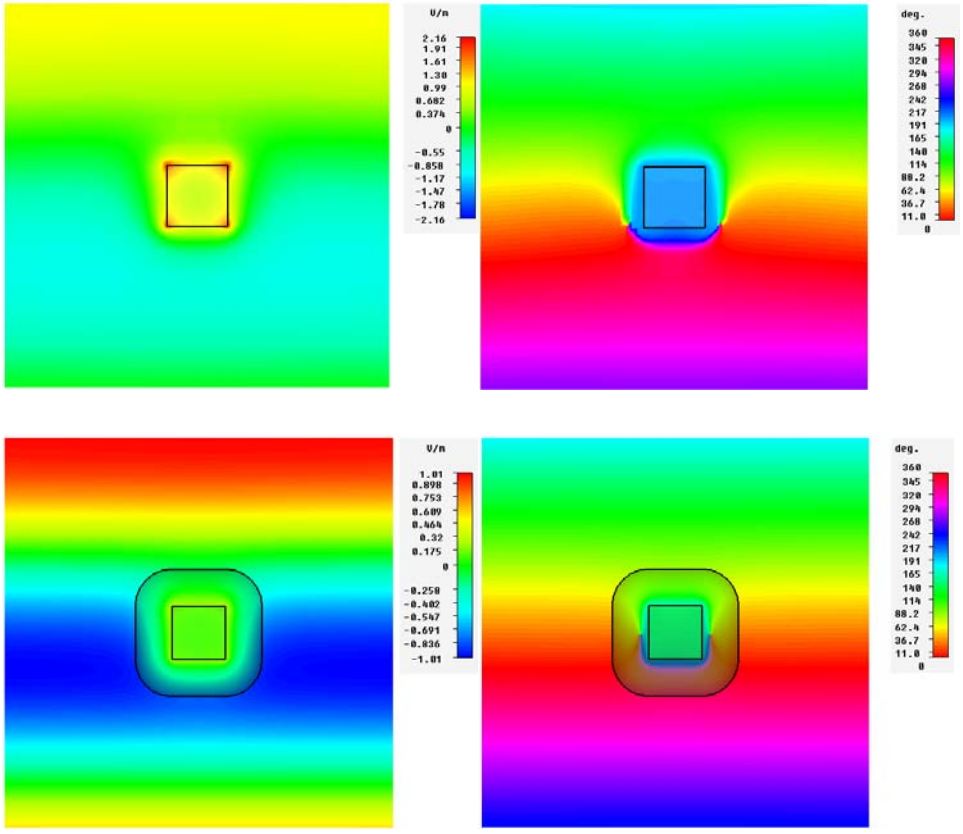

Figure 3.30 2D maps of the electric field amplitude (left) and phase (right) for the bare silver cube (top) and the cloaked one (bottom) for plane wave incidence from bottom to top with incident electric field of $1V/m$. Figure contained in Reference [47].

In Figure 3.31, we report the variation of the total scattering reduction ($\underline{\sigma}$), that is the ratio between the SCS of the bare object and the cloaked one, with the angle of incidence of the illuminating plane wave, varying from incidence orthogonal to one face to the case of incidence on the cube edge. It is evident that the conformal design of the cloak ensures similar cloaking performance independent of the angle of incidence.

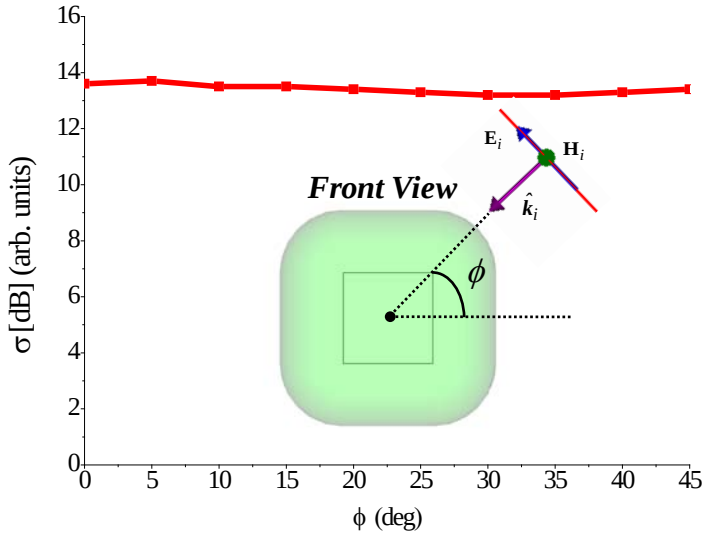

Figure 3.31 Total scattering reduction between the SCS of the bare cube and the cloaked one as a function of the incidence angle. Figure contained in Reference [47].

We consider now two different geometries for the cloak, keeping the same cubic object: the use of the original spherical shape and the use of a cubical shape without rounded corners, as in Figure 3.32.

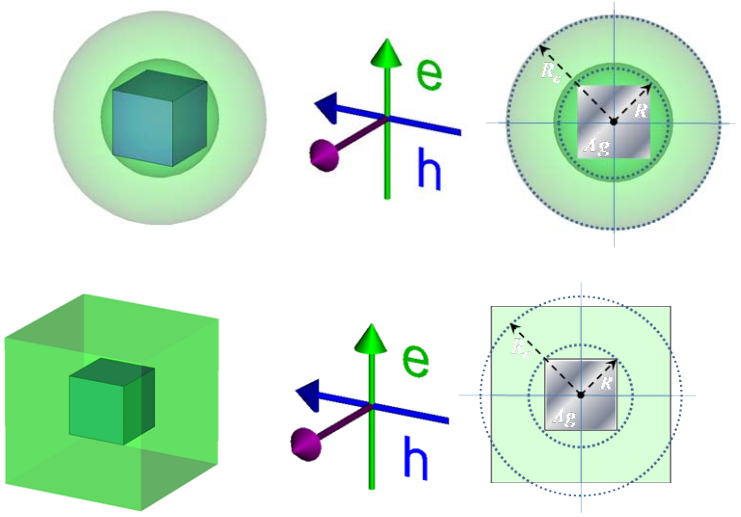

Figure 3.32 A silver cubic particle surrounded by a plasmonic spherical shell (top) and by a cubic one (bottom). Figure contained in Reference [47].

In these cases the scattering reduction is worsened, as expectable, even though the spherical cloak still may achieve a reasonable scattering reduction using high filling ratios. In this case, however, the scattering reduction is more anisotropic, due to the difference in effective

polarizability when impinging at an edge of the cube, as shown in Figure 3.32 (right panel). In the cubic cloak case (left panel), the change in effective volume of the cloak and the presence of sharp edges and vertices produce additional scattering, that worsens the overall performance compared to Figure 3.31.

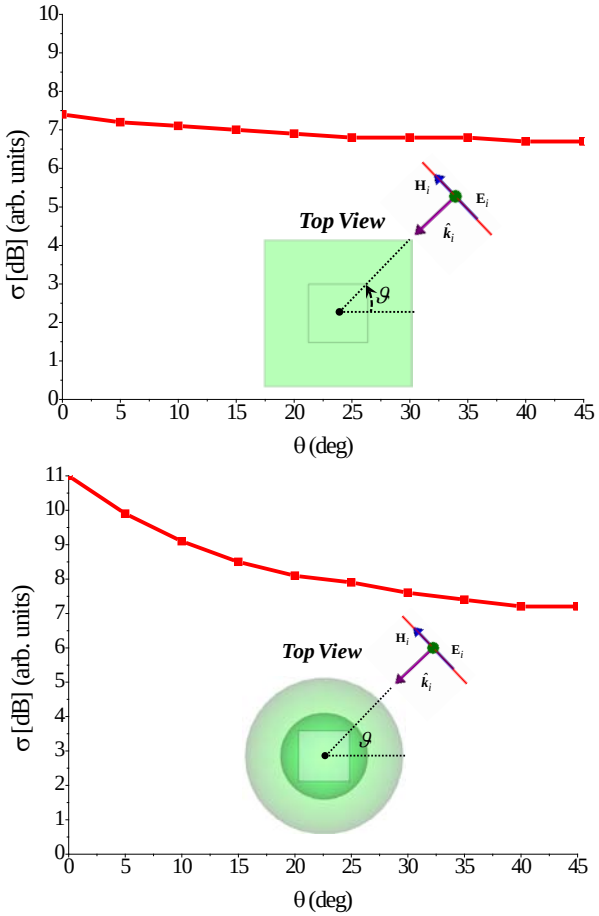

Figure 3.33 Ratio between the SCS of the bare cube and the cloaked one as a function of the incidence angle for a particle surrounded by a non-rounded cubic shell (left) and by a spherical one (right). Figure contained in Reference [47].

The previous examples show that for moderately anisotropic objects it may indeed be possible to design a cloaking plasmonic layer effective over a broad range of angles and polarization, and with quasi-isotropic response. The best solution is to design a conformal cloak with rounded shapes conformal to the object of interest, which provides similar drastic scattering cancellation performance for all angles of incidence. The cloak may still keep its simplicity of design, relying on homogeneous and isotropic materials, but the thickness of the cloak should be locally chosen to conform

to the local variation in the shape of the object. When the geometry gets electrically larger and/or more anisotropic, the simple volumetric formulation (3.1.3) is not strictly applicable, since the ideal assumption of quasi-static fields in the object and the cloak is not valid. Also in this case, however, a proper design of the cloak using physical considerations may be carried out, as shown in the next Section.

We consider different conformal cloaks for dielectric (e.g. made of silica) and plasmonic (e.g. made of silver) objects of different shapes, properly optimized to provide strong scattering reduction for all incidence angles, despite the anisotropic scattering from the object to be cloaked. The plasmonic covers have been modeled as Drude dispersive media, which is characterized by the following relative permittivity:

$$\varepsilon_r(\omega) = \varepsilon_\infty + \frac{\omega_p^2}{\omega(\omega - j\nu_c)}, \tag{3.1.4}$$

being ω_p the plasma frequency, ε_∞ the upper frequency permittivity limit and ν_c the damping factor taking into account losses. The characteristic electrical dimension of each obstacle is $200\,nm = 2/5\,\lambda_0$ at the operating frequency of 600 THz.

Consider first a dielectric cube of silica [60,61] with a diagonal length $\ell = 280$ nm, as in Figure 3.34, which reports also the scattering width of the object (measured in squared wavelengths). It is evident that for this size the scattering is not purely dipolar any longer, and higher-order multipoles contribute to a more directive scattered shadow. A proper cloak may be synthesized as a conformal cover, as discussed in the previous section. We have derived with numerical optimization the proper Drude parameters in (3.1.4) to achieve a good scattering reduction with a thickness $d = 40$ nm. The damping frequency has been assumed $\nu_c = 10^{-2}\omega_p$, which is a realistic value for plasmonic materials at optical frequencies. For a value $\varepsilon_r \approx 0.38$ at the design frequency, the scattering is sensibly reduced, as evident in Figures 3.35-3.36. In particular, Figure 3.35 reports the field distributions in the cloaked and uncloaked case for plane wave incidence from bottom to top of the figure (towards a side of the cube).

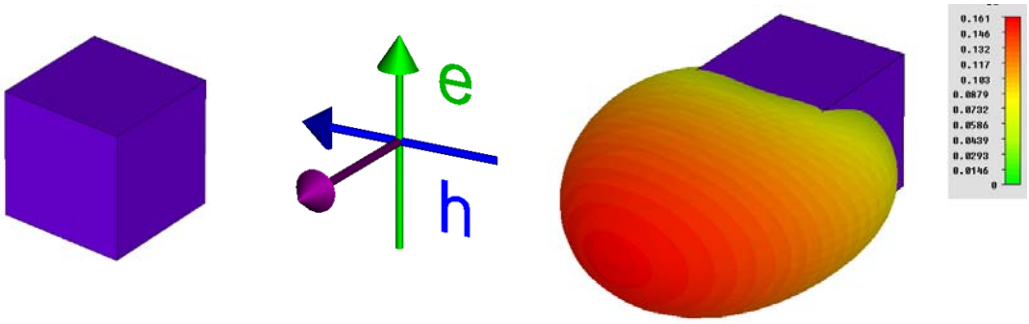

Figure 3.34 Radar cross-section of a dielectric cube of silica for the given polarization.

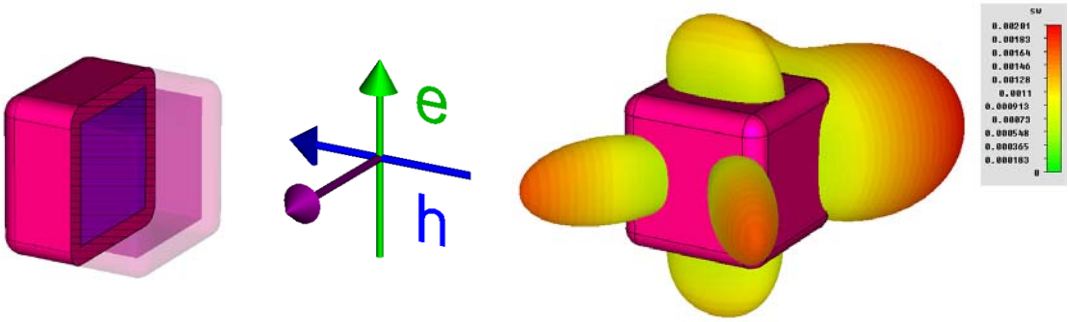

Figure 3.35 Radar cross-section of a cloaked dielectric cube of silica for the given polarization. Figure contained in Reference [47].

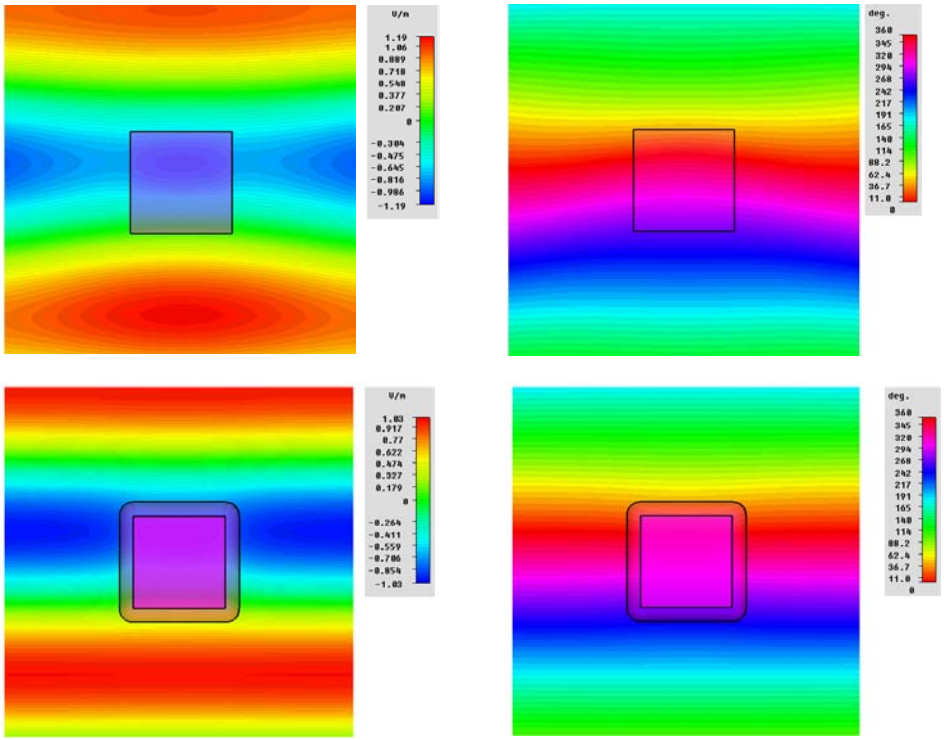

Figure 3.36 2D maps of the electric field amplitude (left) and phase (right) for the bare silica cube (top) and the cloaked one (bottom). Figure contained in Reference [47].

Even by changing the angle of incidence for the impinging plane wave we still verify good performances, even in the worst case scenario of incidence at the edge, as shown in Figure 3.37. The proper shape of the cloak, designed as outlined in the previous section, produces a quasi-isotropic cloaking effect.

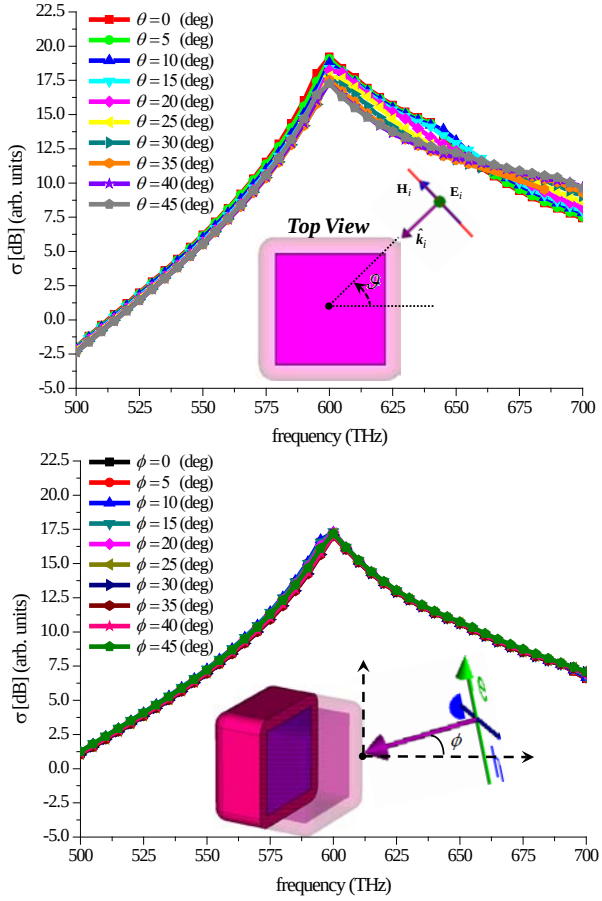

Figure 3.37 Ratio $\underline{\sigma}$ between the SCS of the bare cube and the cloaked one as a function of the incidence angle. Figure contained in Reference [47].

Next, we have simulated a silica octahedron with the same volume as the previous cube, as in Figure 3.38. Again performing a numerical optimization, we have found that for $\varepsilon_r \approx 0.35$ and a cover thickness $d = 26\,\text{nm}$ the SCS may be reduced by almost 12 dB. This value is almost constant with respect to a variation of the angle formed by the electric field vector and one of the principle diagonals of the octahedron, as shown in Figure 3.38.

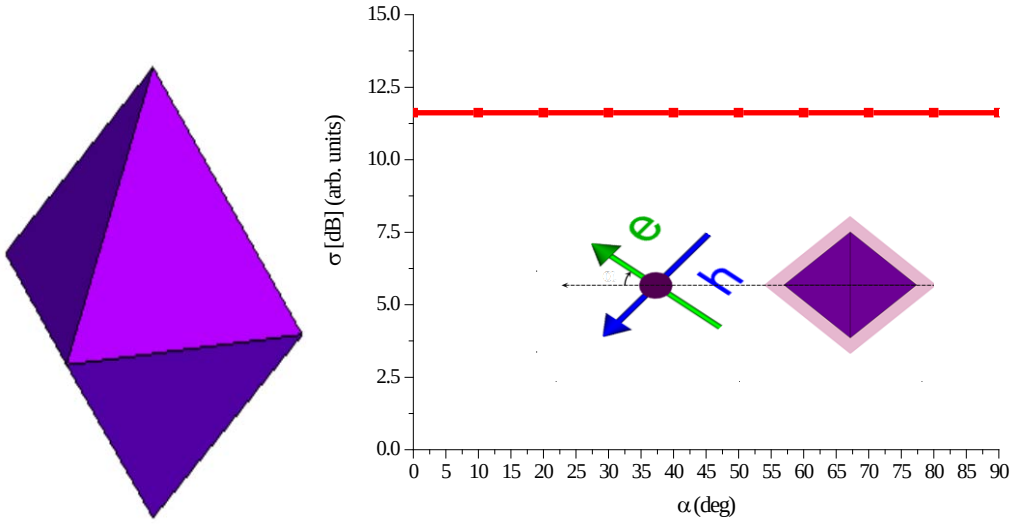

Figure 3.38 Radar cross-section of a silver octahedron for the given polarization. Figure contained in Reference [47].

The transparency effect is indeed evident in the 2D maps of the electric field in Figure 3.39, where the field lines of the bare silica octahedron and the cloaked one are compared.

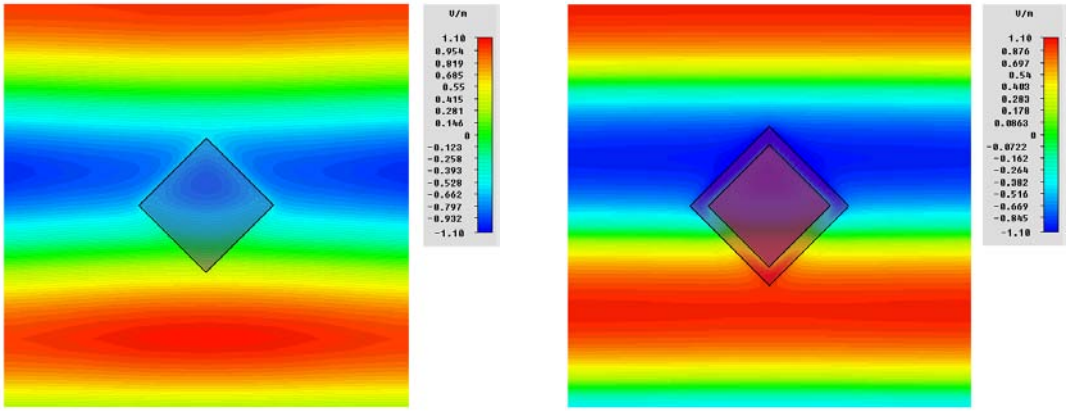

Figure 3.39 maps of the electric field amplitude for the bare silica octahedron (left) and the cloaked one (right). Figure contained in Reference [47].

The same results may be obtained also for more anisotropic shapes. We have considered, for example, a silica cone with a base diameter of 120 nm and an height of 160 nm. For a cover thickness $d = 20$ nm and $\varepsilon_r \approx 0.46$ we get a very strong reduction of the scattering width, as shown in Figure 3.40. Once again, the anisotropic scattering effect of an asymmetric shape like a cone may be compensated by properly covering the cone with a conformal plasmonic cloak, which presents similar anisotropic response, ensuring that

the cancellation mechanism is quasi-isotropic. Clearly, if one had chosen to cloak the cone with a spherical plasmonic cloak, the scattering reduction could have worked only for a limited range of illumination angles, due to the strong anisotropy in its shape.

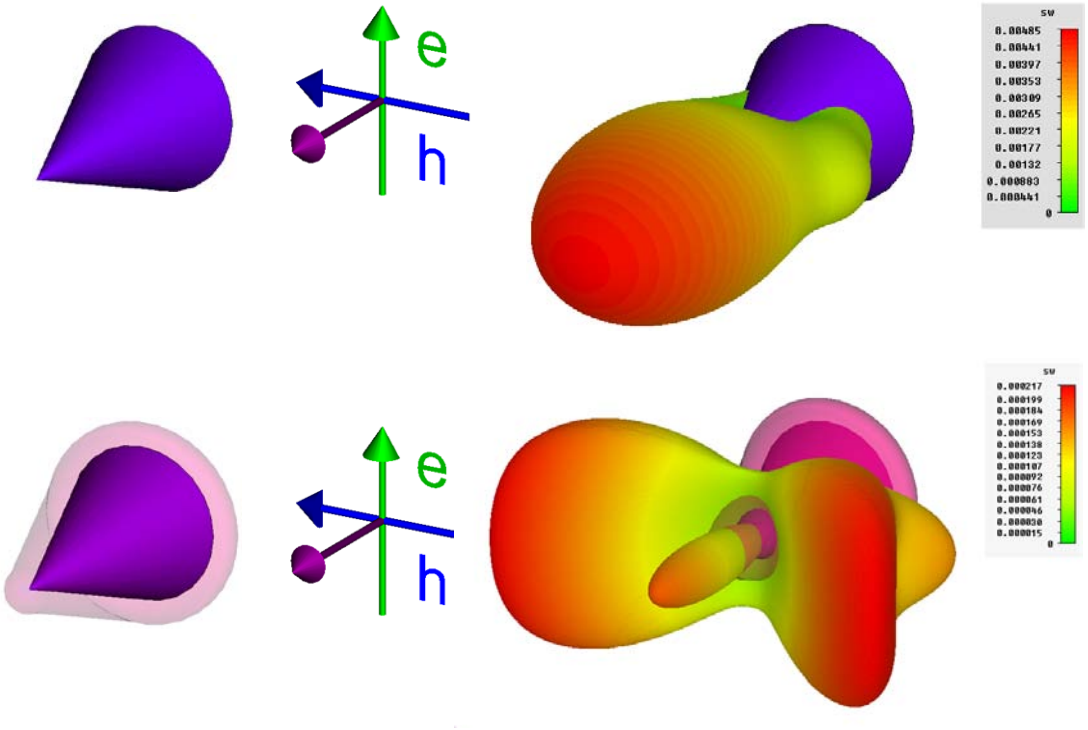

Figure 3.40 Ratio σ between the SCS of the silica bare cone and the cloaked one as a function of polarization angle. Figure contained in Reference [47].

As it can be clearly seen in Figure 3.41, instead this structure is not sensitive to variation of the illuminating radiation polarization. It is seen that for electric field parallel to the axis of the cone, stronger polarization is expected, and therefore a larger effective thickness of the plasmonic material has been chosen along the axis. This ensures that the scattering reduction is uniform with the orientation of the electric field, different from the geometry analyzed in [65].

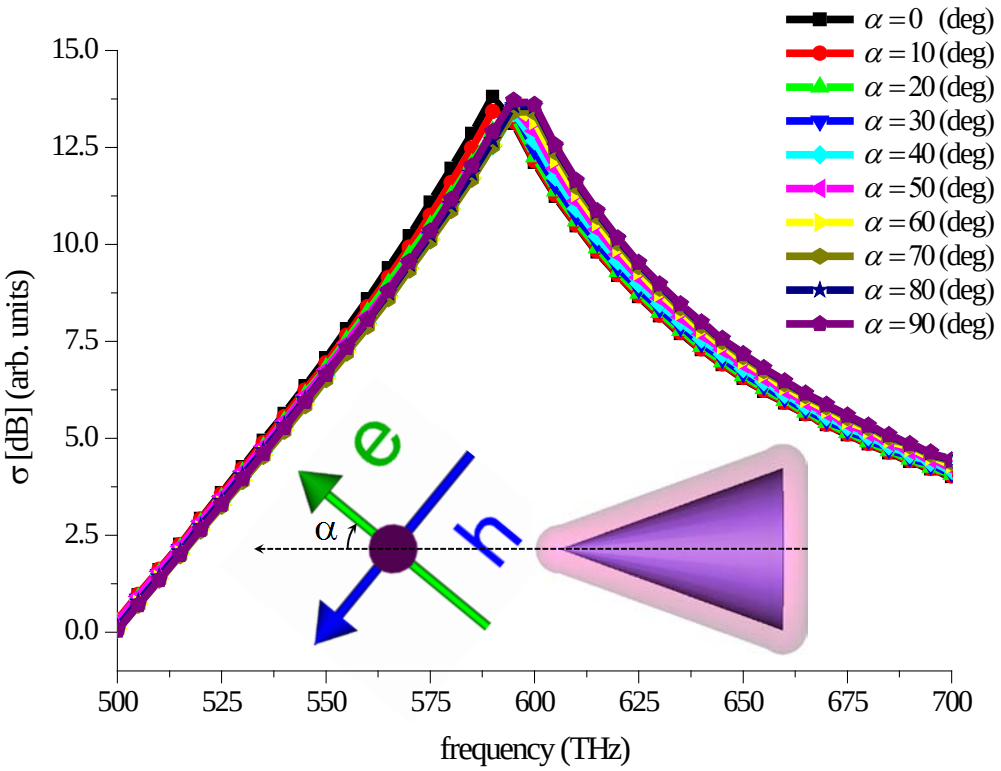

Figure 3.41 Ratio σ between the SCS of the bare cone and the cloaked one as a function of polarization angle. Figure contained in Reference [47].

We have also investigated the response of a cone geometrically identical to the the previous one, but made of silver, with similar results (Figures **Errore. L'origine riferimento non è stata trovata.**3.42-3.43). Also in this case, despite the less penetrable nature of the conical object, drastic scattering suppression is achieved for $d = 20\,\text{nm}$ and $\varepsilon_r \approx 0.18$. In this scenario, however, when the electric field lies along the cone axis, the scattering reduction is less isotropic and poorer performance is obtained, due to the inherent electric field enhancement at the plasmonic tip (Figure 3.43).

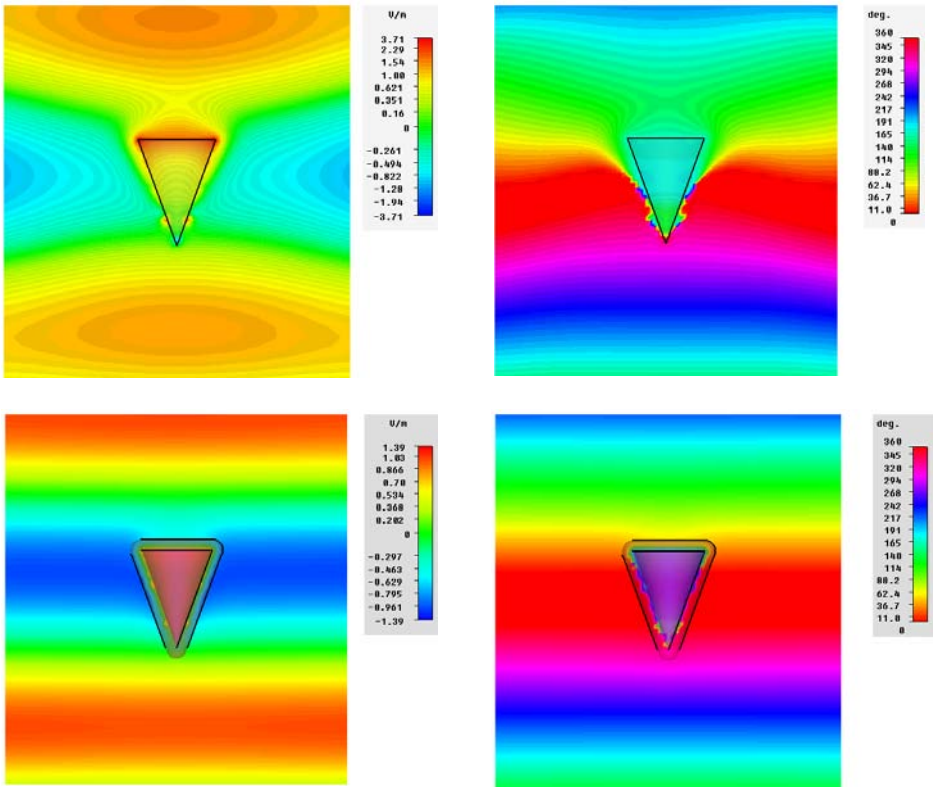

Figure 3.42 2D maps of the electric field amplitude (left) and phase (right) for the bare silver cone (top) and the cloaked one (bottom). Figure contained in Reference [47].

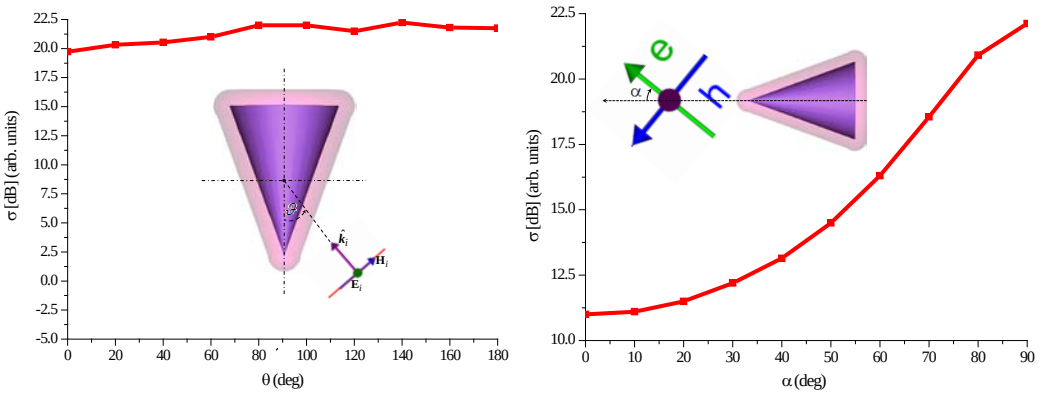

Figure 3.43 Ratio σ between the SCS of the silver bare cone and the cloaked one as a function of the incidence angle. Figure contained in Reference [47].

This kind of response is expectable, and is inherently related to the initial choice we adopted to design a conformal cover with a constant thickness. However, for anisotropic scatterers with plasmonic properties, the drastic field enhancement at the tip should be properly taken into account by increasing the cloak thickness near the tip, as shown in Figure 3.44. This would ensure, for the same homogeneous material composing the cloak, a

larger local polarizability that may compensate the increased scattering from the tip.

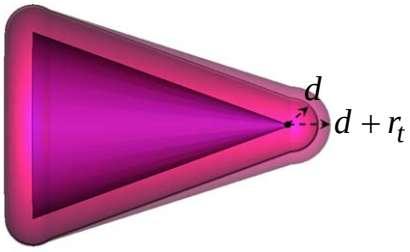

Figure 3.44 Cloaking cover for the silver cone locally thicker around the tip. Figure contained in Reference [47].

By numerically optimizing the cover thickness d near the tip, we obtain for a slight variation $r_t = 7$ nm of the initial setup an almost isotropic response for all the incidence angles, as reported in Figure 3.45.

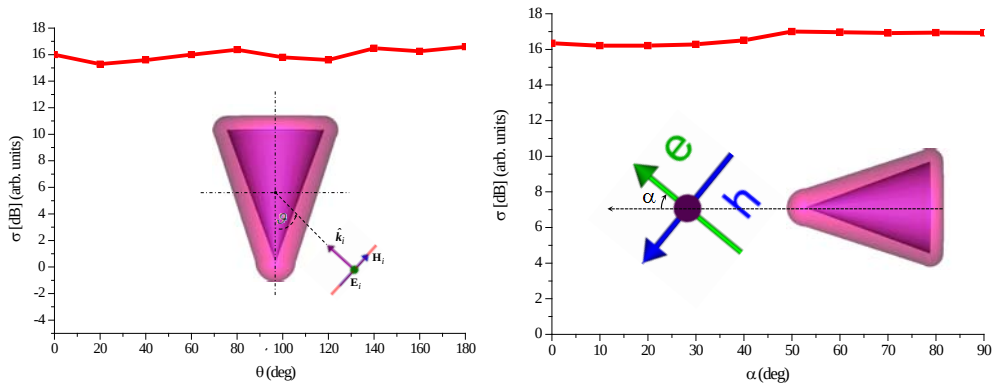

Figure 3.45 Ratio σ between the SCS of the silver bare cone and the cloaked one in the new configuration. Figure contained in Reference [47].

In the next Chapter we will use these results to propose novel setups based on plasmonic cloaking devices in sensing and probing applications.

3.2 Governing Optical forces with Metamaterials

As previously shown, scattering cancellation technique has been recently proposed as one of the possible routes to synthesize invisibility cloaking devices. Following this approach, the scattered field from a given object may be drastically reduced by employing a properly designed conformal plasmonic cover, exhibiting an effective relative electric permittivity smaller than unity. So far, most of the research efforts concerning scattering cancellation have been focused in making a cloaked object nearly transparent to the illuminating electromagnetic radiation. As clearly demonstrated in [43], this phenomenon is inherently related to the dispersive nature of the plasmonic material used for the cloak, which, in the long-wavelength limit, is characterized by a locally negative polarizability compensating the electric dipole scattering contribution due to the object.

In the Rayleigh approximation, however, if the object dimensions approach the nano-scale, optical forces come into play, and their contribution cannot be neglected any more. As early speculated in [69], metamaterials (MTMs) and plasmonic media may allow to control such forces through their inherent dispersive behavior. This implies, for instance, that it is possible to manipulate light forces simply by changing the material characteristics or the operating frequency. We will show that, as reported in [70], it is possible to govern such forces by MTM covers properly designed.

Typically, light forces on electrically small particles are explained in terms of gradient and scattering forces [71]. The former are directly related to the interaction between the external field and the induced dipole, which is drawn by the field intensity gradients. The latter are related to the momentum transfer between the scattered field and the illuminated particle, being proportional to the Poynting vector [71,72]. Since both these forces are inherently associated to the scattering properties of the object, it is interesting to study their behavior when a cloak placed around a nano-particle causes the reduction, or even the suppression, of the total scattered field.

It is possible to combine optical force calculation to the electromagnetic cloaking formulation, in order to obtain further physical insights and

explore new possibilities for the manipulation of nano-structures, with promising results for several applications in current nanotechnology.

3.2.1 Optical Forces Acting on Electrically Small Particles

Optical forces acting on a nano-particle can be derived from the conservation of the linear momentum introducing Maxwell's stress tensor [71]. Without loss of generality, we may consider an object made of an isotropic homogeneous dielectric, surrounded by vacuum, and illuminated by a time harmonic electromagnetic field (excitation of the kind $e^{j\omega t}$ is assumed throughout the paper). Neglecting the particle motion and assuming mass density and optical properties of the object to be constant with respect to the exerted pressure, the time average force $\langle \mathbf{F} \rangle$ exerted on the particle is given by [71,73]:

$$\langle \mathbf{F} \rangle = \frac{1}{4}\Re\mathfrak{e}\left[\alpha_e\right]\nabla\left|\mathbf{E}_0\right|^2 + \frac{\sigma_t}{2c}\Re\mathfrak{e}\left[\mathbf{E}_0 \times \mathbf{H}_0^*\right] + \frac{\sigma_t}{2k_0}\Im\mathfrak{m}\left[\varepsilon_0\left(\mathbf{E}_0^* \cdot \nabla\right)\mathbf{E}_0\right], \tag{3.2.1}$$

where $\Re\mathfrak{e}[\circ]$ and $\Im\mathfrak{m}[\circ]$ are the real and imaginary parts, respectively, $[\circ]^*$ complex conjugation, $k_0 = \omega/c$ the free space wave number, σ_t the total scattering cross section (SCS), and α_e the electric polarizability of the object. In the Rayleigh approximation, any given object with anisotropic scattering properties may be described by its polarizability tensor $\underline{\boldsymbol{\alpha}}_e$ [13,67]. For highly symmetrical small scatterers, the polarizability tensor may be assumed as a scalar quantity α_e, while, for more complex geometries, a similar approach may be still used, assuming the polarizability tensor to be uniaxial in a convenient coordinate system oriented along the three main axes of the scatterer [68]. By means of the optical theorem [74] we can straightforwardly express σ_t in terms of the electric polarizability of the object as:

$$\sigma_t = \frac{k_0}{\varepsilon_0}\Im\mathfrak{m}\left[\alpha_e\right]. \tag{3.2.2}$$

Therefore, in (3.2.1) we distinguish three terms, related to the acting forces on the particle: the first one is the *gradient force*, the second one is the scattering force or *radiation pressure* and the third one, which is generally neglected in the case of electrically small objects [73], has been recently

associated to the time averaged spin density of a transverse electromagnetic field [75].

According to (3.2.1), by nullifying the complex electric polarizability α_e (both real and imaginary parts), we are able to contemporary minimize all the force contributions acting on Rayleigh scatterers. In the following, we show how it is possible to achieve such condition by using scattering cancellation approach, in the general case of lossy materials described by proper dispersion models.

Let us consider, as a first example, the case of a *spherical particle* of radius *a* and permittivity function $\varepsilon(\omega)=\varepsilon_0\,\varepsilon_r(\omega)$. Due to the symmetry of the problem, the electric polarizability does not depend on the polarization of the electric field. In the limit $k_0 a \ll 1$, the electric polarizability $\alpha_e^s(\omega)$ is given by [15, 21]:

$$\alpha_e^s(\omega)=\frac{\alpha_e^0(\omega)}{1-j\dfrac{k_0^3\alpha_e^0(\omega)}{6\pi\varepsilon_0}}, \qquad \text{with:} \qquad \alpha_e^0(\omega)=3\varepsilon_0 V\frac{\varepsilon_r(\omega)-1}{\varepsilon_r(\omega)+2}, \tag{3.2.3}$$

where the radiation-reaction term (due to the interaction of the dipole with its own radiated field) has been introduced, in order to satisfy the optical theorem [71,75]. It is worth noticing that optical force formulation, derived through Maxwell's stress tensor, is fully consistent with the approach based on the Lorentz force calculation [54,76,77].

From (3.2.3), it may be easily derived that an electrically small sphere, made of a regular dielectric material with $\varepsilon_r>1$, will always experience an acting optical force, according to (3.2.1). Let us assume, now, that the scatterer is made of a material whose relative permittivity $\varepsilon_r(\omega)$ follows Drude dispersion model as:

$$\varepsilon_r(\omega)=\varepsilon_\infty-\frac{\omega_p^2}{\omega(\omega-j\nu_c)}, \tag{3.2.4}$$

being ω_p the plasma frequency, ε_∞ the upper frequency permittivity limit and ν_c the damping factor. As it results from the expression of α_e^s, the complex polarizability exhibits a resonant behavior at $\omega=\omega_r$, where the plasmonic resonance occurs for $\varepsilon_r(\omega_r)=-2$, thus implying that $\Re\mathrm{e}\left[\alpha_e^s(\omega_r)\right]=0$, while $\Im\mathrm{m}\left[\alpha_e^s(\omega_r)\right]$ reaches its maximum. As it is well

know, in this case, the radiation pressure term is enhanced by the plasmonic nature of the material at the resonance frequency. On the other hand, being the real part of α_e^s almost zero at $\varepsilon_r(\omega_r) = -2$, the gradient force term is significantly reduced, even if $\nabla|\mathbf{E}_0|^2 \neq 0$, as it may be generally assumed. Only under plane-wave illumination, in fact, the first and the last terms of equation (3.2.1) are identically zero [73], being the radiation pressure, which is proportional to the Poynting vector, the only force contribution acting on the scatterer.

Now, if we cover the scatterer with a plasmonic shell of radius b and relative permittivity $\varepsilon_c(\omega)$, the overall polarizability α_e^{cs} of the rigid covered particle, may be consistently expressed as [77,78]:

$$\alpha_e^{cs}(\omega) = \frac{\alpha_e^0(\omega)}{1 - j\dfrac{k_0^3 \alpha_e^0(\omega)}{6\pi\varepsilon_0}}, \qquad (3.2.5)$$

$$\alpha_e^0(\omega) = 4\pi b^3 \varepsilon_0 \frac{b^3(\varepsilon_c - 1)(2\varepsilon_c + \varepsilon_r) - a^3(2\varepsilon_c + 1)(\varepsilon_c - \varepsilon_r)}{b^3(\varepsilon_c + 2)(2\varepsilon_c + \varepsilon_r) - 2a^3(\varepsilon_c - 1)(\varepsilon_c - \varepsilon_r)}$$

where the frequency dependence of the permittivities has been omitted for sake of brevity. In the limit case $\varepsilon_c \to 1$, we obtain the polarizability of the bare sphere $\alpha_e^s(\omega)$, otherwise, according to theory developed in [43], for any given relative permittivity ε_r of the inner particle, it is possible to determine a certain range of permittivity values for the cover material, which allow nullifying contemporarily both the real and the imaginary parts of the complex polarizability $\alpha_e^{cs}(\omega)$.

In order to clarify these aspects, let us consider an example. The inner core of a coated spherical particle is made of a regular dielectric with $\varepsilon_r = 2$, while the external shell is made of a Drude-like dispersive and lossy material. According to equation (3.2.5), for a certain value of the permittivity $\varepsilon_c(\omega_0)$ at the design frequency ω_0, we may find an optimal ratio between the radii $\beta = a/b$, assuring that $\alpha_e^{cs}(\omega_0) \approx 0$, thus implying that $\Re\mathrm{e}\left[\alpha_e^s(\omega_0)\right] = 0$, while keeping the imaginary part extremely low.

In Figure 3.46, we show the complex polarizability as a function of the normalized frequency ω/ω_p and β, with $\nu_c = 10^{-2}\omega_p$.

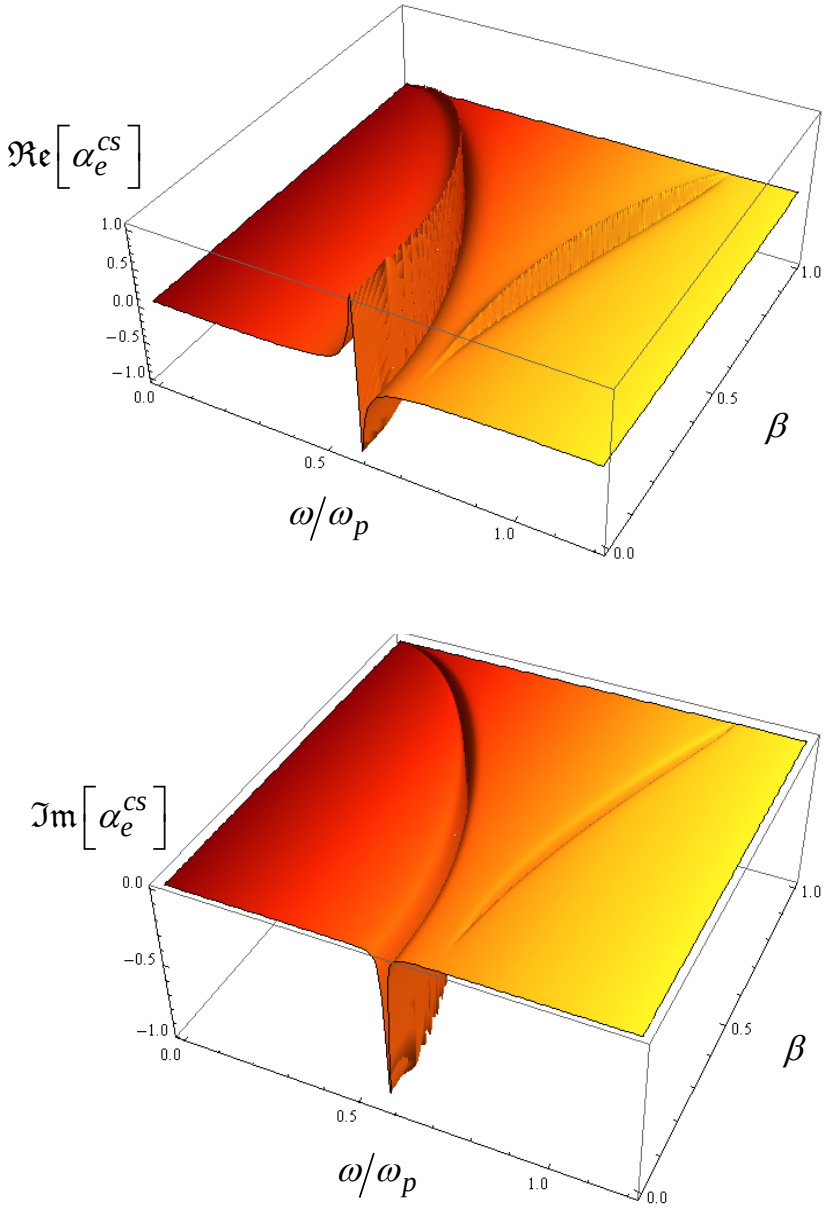

Figure 3.46 Complex polarizability of a dielectric electrically small spherical particle covered with a plasmonic coating whose permittivity follows Drude dispersion. Real and imaginary parts of the polarizability are normalized to their relative maximum values. Figure contained in Reference [47].

From these plots, we note that there is a frequency region in the dielectric plane described by $\varepsilon_c(\omega)$ and ε_r, in which the condition $\alpha_e^{cs}(\omega_0) \approx 0$ is satisfied (in Figure 3.47 we show one of the zero occurrences for $\beta \approx 0.67$).

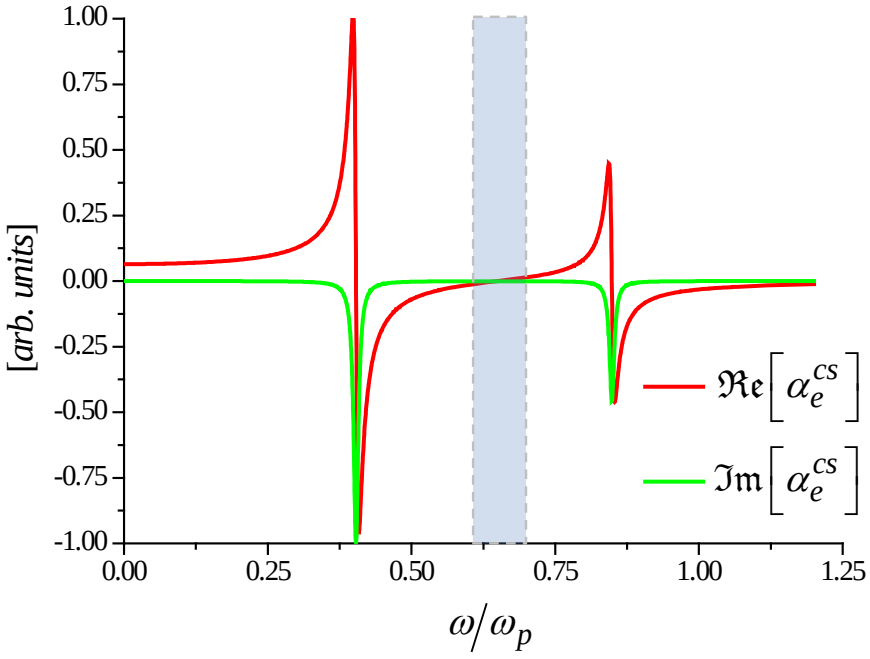

Figure 3.47 Complex polarizability (normalized to its maximum value) for a dielectric electrically small spherical particle covered with a plasmonic coating, whose permittivity follows Drude dispersion, for $\beta \approx 0.67$. The shadowed area indicates the frequency region in which the complex polarizability is almost zero. Figure contained in Reference [47].

Polarizability cancellation effect is certainly affected when increasing losses, that is when varying the collision frequency ν_c in the model. However, it is worth noticing that, being the scattering cancellation approach based on a non-resonant phenomenon, we can reasonably assume that losses are generally sufficiently small in the frequency range of interest. Nevertheless, even considering moderately higher losses, it is still possible to obtain the desired behavior, as shown in Figure 3.48, where a dependence $\nu_c = 10^{-\sigma}\omega_p$ for the collision frequency is assumed.

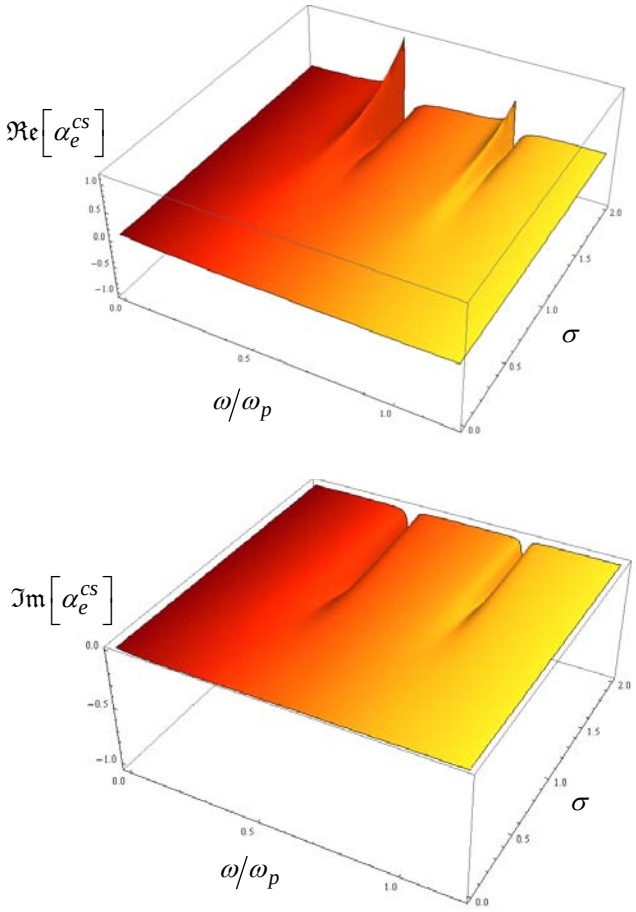

Figure 3.48 Normalized complex polarizability for a dielectric electrically small spherical particle covered with a plasmonic coating, whose permittivity follows Drude dispersion, for $\beta \approx 0.67$ and assuming losses to vary according to $\nu_c = 10^{-\sigma}\omega_p$. Figure contained in Reference [47].

The proposed formulation is certainly consistent also when describing 2D configurations, that is when considering, for instance, nanorods and wires with electrically small cross-sections. In this case, it is possible to evaluate the acting forces simply by introducing the proper polarizability [75], according to the previous analysis. Let us consider, then, the case of a circular cylinder of radius *a*, infinitely extended along its symmetry axis (Figure 3.49). Referring to the main polarizations of the impinging field, we can define two different polarizabilities $\alpha_e^{\parallel}(\omega)$ and $\alpha_e^{\perp}(\omega)$, depending on whether the illuminating electric field is parallel or perpendicular to the cylinder axis ($\hat{z}$), respectively.

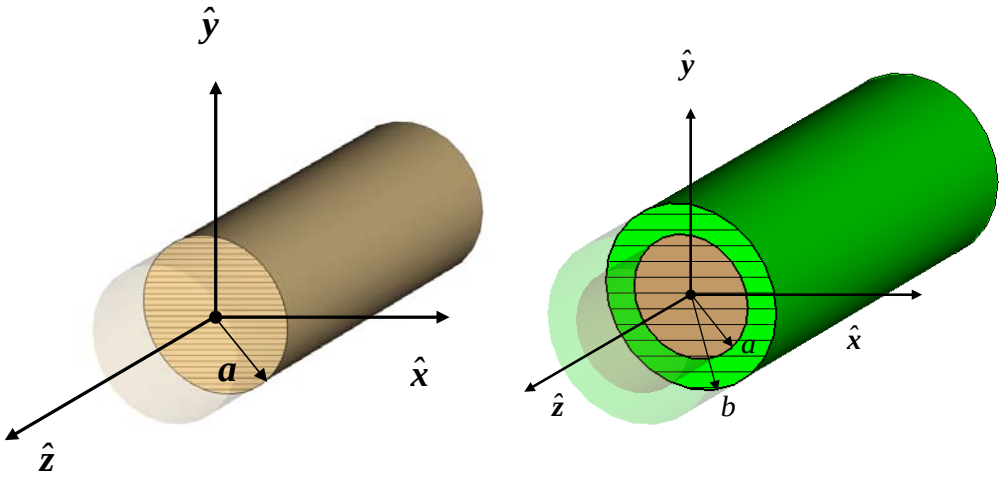

Figure 3.49 Cylindrical nanorod of radius *a* infinitely extended along its symmetry axis (left). Cylindrical nanorod of radius *a* infinitely extended along its symmetry axis and covered with a plasmonic shell of radius *b*. Figure contained in Reference [47].

For an electrically small cylinder with permittivity $\varepsilon(\omega)=\varepsilon_0\,\varepsilon_r(\omega)$, polarizability $\alpha_e^{\parallel}(\omega)$ may be expressed through a series expansion of the zeroth order Mie scattering coefficient as [79]:

$$\alpha_e^{\parallel}(\omega)=\frac{\alpha_e^{p}(\omega)}{1-j\dfrac{k_0^2}{4\varepsilon_0}\alpha_e^{p}(\omega)},\qquad \alpha_e^{p}(\omega)=\pi a^2\varepsilon_0\left[\varepsilon_r(\omega)-1\right], \tag{3.2.6}$$

while for the orthogonal polarization $\alpha_e^{\perp}(\omega)$ can be similarly written as [80]:

$$\alpha_e^{\perp}(\omega)=\frac{\alpha_e^{o}(\omega)}{1-j\dfrac{k_0^2}{4\varepsilon_0}\alpha_e^{o}(\omega)},\qquad \alpha_e^{o}(\omega)=\pi a^2\varepsilon_0\frac{\varepsilon_r(\omega)-1}{\varepsilon_r(\omega)+1}. \tag{3.2.7}$$

Looking at expressions (3.2.6) and (3.2.7), it follows that also in this case, for any $\varepsilon_r\geq 1$, the object experiences an acting force in both the polarizations. If the cylinder is made of a plasmonic material, $\alpha_e^{\perp}$ shows a resonant behavior similar to the one of a small sphere, this time with the material resonance occurring at $\varepsilon_r(\omega_r)=-1$.

It is worth noticing that, even if the cylinder is assumed to be infinitely long, the approach still applies for finite length wires, provided that the effective length L of the object is comparable to the operating wavelength.

Again, when coating the cylinder with an external shell of radius b, as reported in Figure 3.49 (right panel), the total polarizabilities in the main polarizations $\alpha_{e,c}^{\parallel}$ and $\alpha_{e,c}^{\perp}$ are given by:

$$\alpha_{e,c}^{\parallel}(\omega)=\frac{\alpha_e^{cp}(\omega)}{1-j\frac{k_0^2}{4}\alpha_e^{cp}(\omega)},$$
$$\alpha_e^{cp}(\omega)=\pi\varepsilon_0 a^2\left[\varepsilon_r(\omega)-1\right]-\pi\varepsilon_0\left(b^2-a^2\right)\left[\varepsilon_c(\omega)-1\right] \quad , \quad (3.2.8)$$

and

$$\alpha_{e,c}^{\perp}(\omega)=\frac{\alpha_e^{co}(\omega)}{1-j\frac{k_0^2}{4}\alpha_e^{co}(\omega)},$$
$$\alpha_e^{co}(\omega)=\pi b^2\varepsilon_0\frac{b^2(\varepsilon_c-1)(\varepsilon_c+\varepsilon_r)-a^2(\varepsilon_r+1)(\varepsilon_c-\varepsilon_r)}{b^2(\varepsilon_c+1)(\varepsilon_c+\varepsilon_r)-a^2(\varepsilon_c-1)(\varepsilon_c-\varepsilon_r)} \quad . \quad (3.2.9)$$

In Figure 3.50, we show the complex polarizability of a coated nanorod consisting of a dielectric inner core with $\varepsilon_r=2$ and a lossy plasmonic external shell whose permittivity is modeled through a Drude-like dispersion model, as a function of the normalized frequency ω/ω_p and $\beta=a/b$, assuming $\nu_c=10^{-2}\omega_p$.

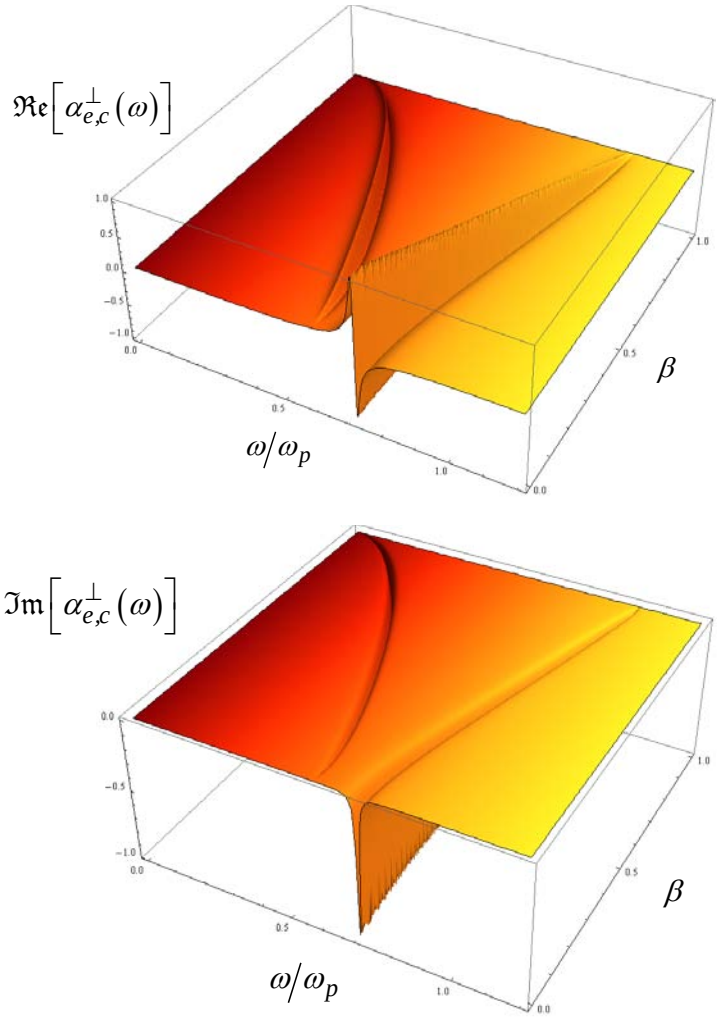

Figure 3.50 Normalized complex polarizability for a dielectric nanorod covered with a plasmonic coating, whose permittivity follows Drude dispersion (electric field orthogonal to the symmetry axis). Figure contained in Reference [47].

According to (3.2.9), at a given pair (ω_0, β) it may result $\alpha_{e,c}^{\perp}(\omega_0) \approx 0$, thus implying that no force is exerted on the object for that polarization. As in the spherical case, moderately high losses still allows to obtain the cancellation effect, as reported in Figure 3.51.

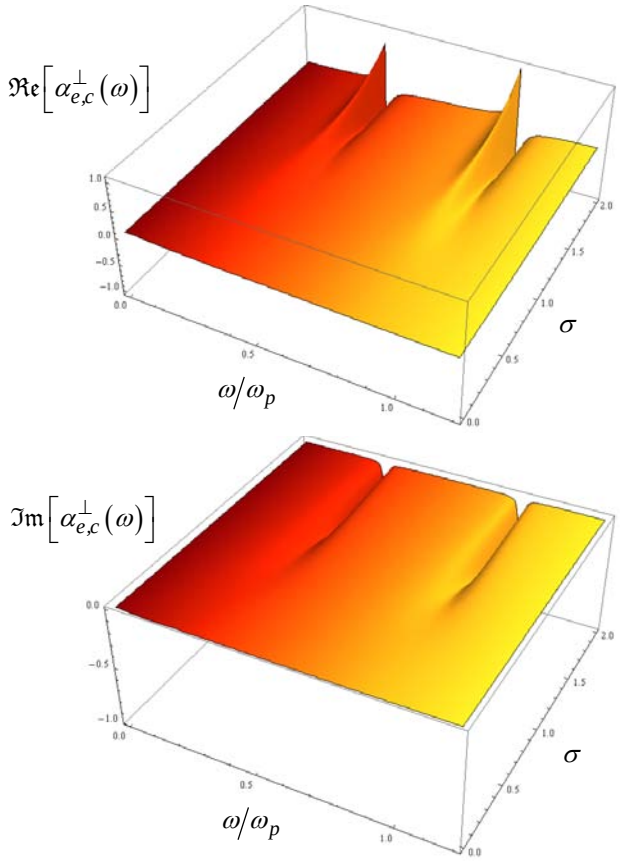

Figure 3.51 Normalized complex polarizability for a dielectric nanorod (electric field orthogonal to the symmetry axis) covered with a plasmonic coating whose permittivity follows Drude dispersion, for $\beta \approx 0.67$ and assuming losses to vary according to $\nu_c = 10^{-\sigma}\omega_p$. Figure contained in Reference [47].

For more complex geometries, as recently shown in the previous secions, it is still possible to use conformal plasmonic coatings to effectively cloak the object, even in the case the scatterer shows a strong anisotropic electromagnetic response. Moreover, for moderately low dielectric contrasts, Rayleigh particles should exhibit polarizability values very close to the ones of an isovolumetric sphere, thus implying that similar considerations may be straightforwardly applied even for non canonical shapes.

3.2.2 Optical Torque and Dipolar Interaction on Cloaked Nanoparticles

Starting from equation (3.2.1), we can derive the intrinsic optical torque $\mathbf{\Gamma}$ acting on a small particle under Rayleigh approximation. For a dielectric object illuminated by an external field $\mathbf{E}_0$, the induced dipole $\mathbf{p}$ leads to an electric torque which, adding the radiation-reaction term to the static polarizability α_e^0, is given by [76,82]:

$$\mathbf{\Gamma} = \frac{1}{2}\Re\mathfrak{e}\left[\mathbf{p}\times\left(\frac{\mathbf{p}}{\alpha_e^0}\right)^*\right]. \tag{3.2.10}$$

Consequently, the torque vector magnitude is directly proportional to α_e^0 and all the considerations done in the previous Sections still apply. Interestingly, since in the more general case the polarizability is a tensor and $\mathbf{p}=\underline{\alpha}_e(\omega)\cdot\mathbf{E}_0$, the torque magnitude depends not only on the orientation of the impinging field, but also on the elements of $\underline{\boldsymbol{\alpha}}_e(\omega)$. This implies that the stability of the configuration may change when coating an object with a plasmonic shell. In particular, it is possible to determine new equilibrium positions, or to make stable an equilibrium position which results unstable for the bare particle.

Let us consider, for instance, the case of a dielectric cylinder of radius *a* and length *L*, with the major axis aligned along the $\hat{\mathbf{z}}$ direction. We may assume that the polarizability of such a particle is uniaxial, as:

$$\underline{\boldsymbol{\alpha}}_e = \alpha_e^{zz}\hat{\mathbf{z}}\hat{\mathbf{z}} + \alpha_e^t\underline{\mathbf{I}}_t, \tag{3.2.11}$$

where the components of $\underline{\boldsymbol{\alpha}}_e$ may be derived either by interpolating functions [81] or by remembering that, for a finite length electrically thin cylinder, the SCS (and, consequently, the polarizability) is proportional to the one of the infinite case, through the effective length of the object. Interestingly, expression (3.2.11) holds, in general, for any given elongated symmetrical particle. For instance, a prolate spheroid may be described by a closed-form uniaxial polarizability tensor [81,82], for which it is well known that, when the impinging electric field is parallel to one of the three main axes, no torque is exerted. If the spheroid is made of a regular dielectric with $\varepsilon_r > 1$, the direction of the torque components is independent from the magnitude of ε_r, and, since $\alpha_e^{zz} > \alpha_e^t$, the equilibrium positions along the

minor axes are unstable, so that the particle tends to align with the major axis along the impinging electric field direction [82]

Since the relative amplitudes of the tensor elements determine the nature (stable or unstable) of the equilibrium positions, by using the polarizabilities derived for the infinite length coated cylinder (see previous Section), we may now find some regions in the dielectric plane described by $(\varepsilon_c, \varepsilon_r)$ such that unstable equilibrium positions for the bare particle may be turned to stable ones for the coated particle, and viceversa.

In Figure 3.52, region plots, referred to the magnitude of the complex polarizability tensor elements of a dielectric cylindrical nanorod with $\varepsilon_r = 2$ covered by the same plasmonic shell as in the previous example, are reported. The colored area in the two plots corresponds to the points for which $\left|\Re\mathrm{e}\left[\alpha_e^{cp}(\omega)\right]\right| < \left|\Re\mathrm{e}\left[\alpha_e^{co}(\omega)\right]\right|$ and $\left|\Im\mathrm{m}\left[\alpha_e^{cp}(\omega)\right]\right| < \left|\Im\mathrm{m}\left[\alpha_e^{co}(\omega)\right]\right|$, respectively, that is when both the real and imaginary parts of the orthogonal polarizability are greater than the longitudinal ones.

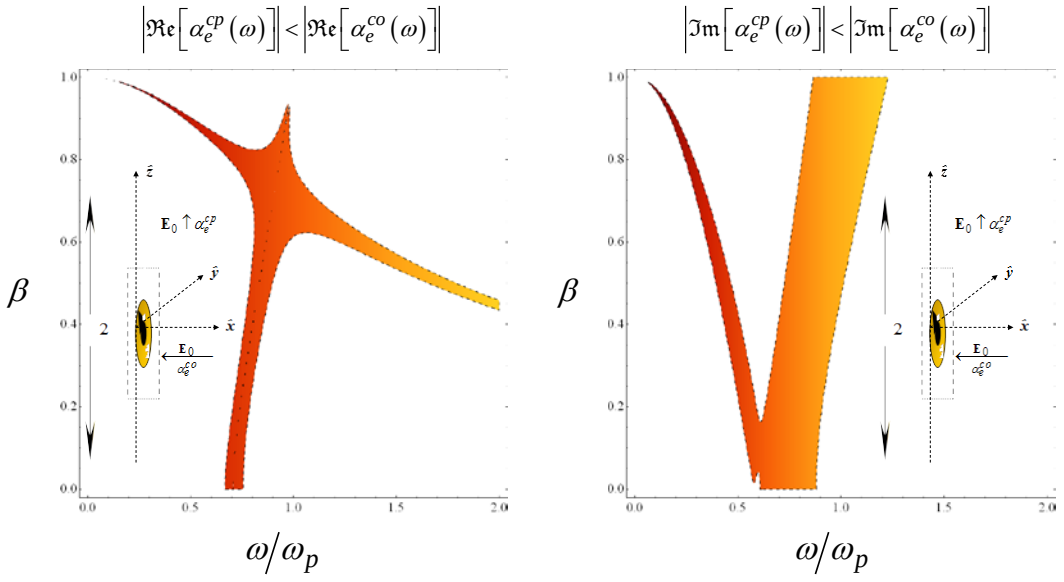

Figure 3.52 Region plots referred to the magnitude of the complex polarizability tensor elements of a dielectric nanorod with $\varepsilon_r = 2$, covered by the same plasmonic shell used in Figure 5. White areas represent the points at which the relations shown in the insets are not satisfied. Figure contained in Reference [47].

From Figure 3.52, it is possible to determine a proper parameter range in which the acting torque may be effectively controlled by the plasmonic behavior of the cover. In particular, when the real and imaginary parts of the orthogonal polarizability are both greater than the ones of the longitudinal polarizability, the illuminated nanorod may experience an anomalous torque, leading to the alignment of the particle along the direction of the minor axis. This position, which for uncovered particles is usually an unstable one, turns out to be a stable equilibrium position in the case of the covered particle.

This is only one of the possibilities offered by the new degrees of freedom introduced by plasmonc cloaking for this particular configuration. Further possibilities result also from the exploitation of the cover material dispersion, which may be used to switch equilibrium positions from stable to unstable ones, according to the plots in Figure 3.52.

So far we have considered only particles in free-space. In order to show how the new possibilities offered by plasmonic cloaking can be applied also to more complex scenarios, we consider now the case of a Rayleigh particle placed near the interface of a dielectric half-space, and illuminated by an external field $\mathbf{E}_0$, as shown in Figure 3.53.

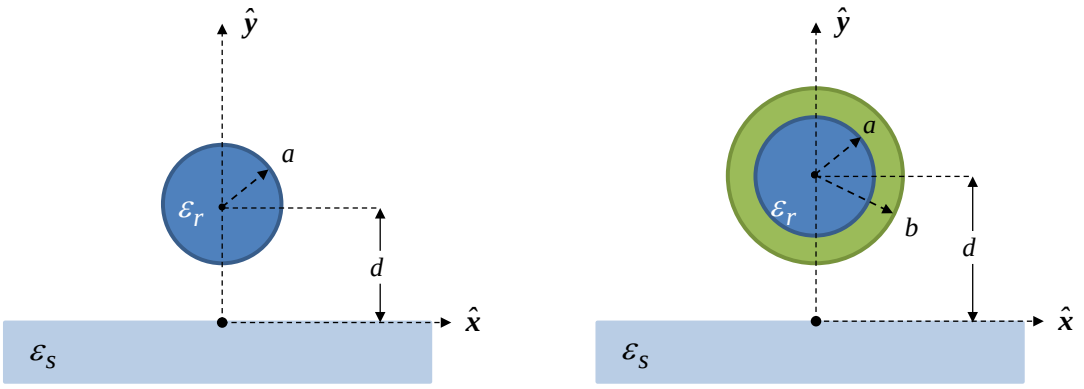

Figure 3.53 A Rayleigh spherical particle placed above a dielectric flat surface (left). Rayleigh spherical particle covered with a plasmonic shell placed above a dielectric flat surface (right) . Figure contained in Reference [47].

In the quasi-static limit, the total electric field at the sphere position may be written as [80]:

$$\mathbf{E}=\left[\underline{\mathbf{I}}-\frac{\alpha_e}{\varepsilon_0}(\omega)\underline{\mathbf{S}}\right]^{-1}\bullet\mathbf{E}_0, \tag{3.2.12}$$

where the tensor $\underline{\mathbf{S}}$ is the linear response of an electric dipole in presence of the half-space (polarizability is assumed to be a constant, but also anisotropic media may be considered simply by changing α_e when varying the polarization of the applied field). Assuming that the distance bewteen the object and the surface is electrically small, in the long-wavelength limit $\underline{\mathbf{S}}$ is uniaxial, and its elements are related only to the relative distance from the particle and to the electric properties of the half-space, that is to its relative permittivity ε_s, as [80]:

$$\underline{\mathbf{S}}=\frac{1}{8d^3}\frac{\varepsilon_s-1}{\varepsilon_s+1}\begin{pmatrix}1&0&0\\0&2&0\\0&0&1\end{pmatrix}=\frac{1}{8d^3}\gamma\begin{pmatrix}1&0&0\\0&2&0\\0&0&1\end{pmatrix}, \tag{3.2.13}$$

being γ the Fresnel reflection coefficient, and d the distance of the surface from the center of the particle. As we can see from expression (3.2.13), when $d\to\infty$ we obtain the response of a particle in free space, while for any other value of d, provided that it is smaller than the wavelength, we may evaluate the dipolar coupling. If the propagation vector lies in the xy plane, no force is exerted along $\hat{z}$, due to the symmetry of the problem. Consequently, if we consider a plane wave impinging on the sphere with the electric field directed along $\hat{z}$, the force components are given by [80]:

$$\begin{aligned}F_x&=\frac{|E_{0z}|^2\varepsilon_0}{2}\Re\mathfrak{e}\left[\frac{8d^3\alpha_e\left(jk_{0x}\right)^*}{8\varepsilon_0 d^3+\gamma\alpha_e}\right],\\ F_y&=\frac{\varepsilon_0|E_{0z}|^2}{2}\Re\mathfrak{e}\left[\frac{8d^3\alpha_e\left(jk_{0y}\right)^*}{8\varepsilon_0 d^3+\gamma\alpha_e}+\frac{12d^2|\alpha_e|^2\gamma}{\left|8\varepsilon_0 d^3+\gamma\alpha_e\right|^2}\right],\end{aligned} \tag{3.2.14}$$

while in the orthogonal polarization it is found:

$$F_x = \frac{\varepsilon_0}{2}\Re\mathfrak{e}\left[4d^3\alpha_e\left(jk_{0x}\right)^*\left(\frac{2\varepsilon_0\left|E_{0x}\right|^2}{8\varepsilon_0 d^3+\gamma\alpha_e}+\frac{\varepsilon_0\left|E_{0x}\right|^2}{4\varepsilon_0 d^3+\gamma\alpha_e}\right)\right],$$

$$F_y = \frac{\left|E_{0x}\right|^2\varepsilon_0}{2}\Re\mathfrak{e}\left[\frac{8d^3\alpha_e\left(jk_{0y}\right)^*}{8\varepsilon_0 d^3+\gamma\alpha_e}+\frac{12d^2\left|\alpha_e\right|^2\gamma}{\left|8\varepsilon_0 d^3+\gamma\alpha_e\right|^2}\right]+ \quad . \qquad (3.2.15)$$

$$+\frac{\left|E_{0y}\right|^2\varepsilon_0}{2}\Re\mathfrak{e}\left[\frac{4d^3\alpha_e\left(jk_{0y}\right)^*}{4\varepsilon_0 d^3+\gamma\alpha_e}+\frac{6d^2\left|\alpha_e\right|^2\gamma}{\left|4\varepsilon_0 d^3+\gamma\alpha_e\right|^2}\right]$$

In the case of a covered sphere, we are able to reduce the acting forces (mainly related to the radiation pressure), in the same way as for the configurations considered in the previous Sections. In fact, by inserting $\alpha_e^{cs}(\omega)$ from (5) in equations (3.2.14) and (3.2.15), we easily obtain by inspection that all the force components vanish if both the real and the imaginary parts of the polarizability of the coated spherical particle $\alpha_e^{cs}(\omega)$ vanish.

Interestingly, a similar approach may be used also for cylindrical particles, simply by substituting the proper polarizability $\alpha_e^{\parallel}(\omega)$ or $\alpha_e^{\perp}(\omega)$, according to the polarization of the external field, and by using for $\underline{\mathbf{S}}$ the form:

$$\underline{\mathbf{S}} = \frac{1}{2d^2}\frac{\varepsilon_s-1}{\varepsilon_s+1}\begin{pmatrix}1&0&0\\0&1&0\\0&0&0\end{pmatrix}, \qquad (3.2.16)$$

It is well known that, when a dielectric particle is close to the interface, it may experience an attractive force directed in the opposite direction of propagation of an normally incident illuminating field, due to the interaction of the dipole with its own reflected evanescent field [26]. When coating the particle, the force does not depend only on the distance d anymore, but it can be changed also through the electric permittivity of the cover $\varepsilon_c(\omega)$.

Let us consider, for instance, the case of a plane wave with the electric field directed along $\hat{z}$ and $k_0 = k_y$, normally impinging on the planar surface separating the vacuum and the material. In the case of a spherical particle

placed in the vacuum half-space at a distance d from the surface, equation (3.2.14), after some manipulation, simplifies as:

$$F_y = \frac{\varepsilon_0 |E_0|^2 64 d^3}{2\left|8\varepsilon_0 d^3 + \gamma \alpha_e^{cs}\right|^2}\left\{\frac{k_0}{\varepsilon_0}\Im\mathfrak{m}\left[\alpha_e^{cs}\right] + \frac{3\gamma\left|\alpha_e^{cs}\right|^2}{16 d^4}\right\} = \\ = \frac{\varepsilon_0 |E_0|^2 64 d^3}{2\left|8\varepsilon_0 d^3 + \gamma \alpha_e^{cs}\right|^2}\left(\sigma_t + \frac{3\gamma\left|\alpha_e^{cs}\right|^2}{16 d^4}\right) \quad . \tag{3.2.17}$$

In this expression, we straightforwardly recognize the contribution given by the total SCS σ_t of the particle, while the last term is due to the interaction of the particle with the surface. The zeroes of F_y occur then at:

$$\sigma_t = -\frac{3\gamma\left|\alpha_e^{cs}\right|^2}{16 d^4}. \tag{3.2.18}$$

while the direction of the force is given by $sign\left[\sigma_t + 3\gamma\left|\alpha_e^{cs}\right|^2 \Big/ 16 d^4\right]$. From expression (3.2.18) we may conclude that, for a regular dielectric lossless substrate ($\gamma > 0$), the zeroes of F_y are determined by negative values of σ_t. Such a condition may be achieved if also the imaginary part of the polarizability is negative, and this may happen through a proper choice of the plasmonic properties of the shell surrounding the particle. Similar conclusions may also apply for the cylindrical case.

From the previous analysis, it is clear that the light force upon a particle on a dielectric plane can be controlled through the distance d and the dispersive behavior of the material composing the shell. A suitable design may, thus, allow to engineer the small scatterer response, with interesting applications in particle trapping and manipulation (tweezers).

4. APPLICATIONS IN BIOLECTROMAGNETICS

In this Chapter, different applications of the obtained results are presented. As first, an accurate phantom model of the human upper limb based on the volume conductor approximation [84] is developed. The model implements a simplified anatomical representation of the arm where the involved tissues are stacked in a multilayered cylindrical geometry. Each tissue has been characterized by proper electrical and geometrical properties, according to techniques proposed in the previous chapters. We apply the model to successfully derive the electromagnetic field distribution induced inside the arm by the excitation of an array of electrodes fed by a generic current pattern. We used, then, finite integration based time domain commercial solver [32] to evaluate the passive electromagnetic response of the structure to the given stimulation. Following a classical two-step analysis, the model may thus effectively provide a set of reliable electric parameters, such as current density values, which can be used by active models to predict nerve fibers behavior.

Successively, we propose different applications of metamaterial based setups to improve performances of standard devices employed in biological sensing and probing.

4.1 Modeling the Human Upper Limb: a phantom model of the human arm

The purpose of the study is to define an accurate electromagnetic model of the human arm, able to describe the response of biological tissue to a functional electrical stimulation, designed to reduce tremor faced by patients with Parkinson disease. The general aim is to provide new computational tools in a general framework defined by the international project *TREMOR: Control strategies for active & EDF semi-active tremor suppression* [85], in which this contribute has been developed. The aim is to reduce through electrical stimulation (ES) [84] the involuntary tremor affecting parkinsonian patients.

ES is a technique to force the activation of nerve and muscle fibers by applying electrical current pulses to the human body. The electrical current is injected by active electrodes causing a depolarization of cellular membranes in excitable tissues. Depending on the kind of employed electrode, it is possible to classify ES in implantable, percutaneous, and transcutaneous electric stimulation (TES). With implantable systems, even if high muscular selectivity is obtained by placing the electrodes close to the nerves or to the muscles, surgery is required with high discomfort for the patient. In percutaneous ES needle electrodes are inserted into the body while in TES the electrodes are directly applied on the skin, causing the current to flow through the tissues and exciting them. This latter configuration is the less invasive and, thus, the less traumatic.

The Functional Electrical Stimulation (FES) is TES whose employment should aid to improve or restore muscle functionality by inducing electrical stimulation through an array of active surface electrodes placed in direct contact with the skin, and properly fed. Typically, electrical stimulation involves the injection of current at low frequencies, therefore it is necessary to preliminary study resolution technique available for these types of issues, in particularly with regard to applications in biology.

Even if some multiphysics and analythical models have been implemented [86,87] to describe the physiological behavior of excitable tissues, the choses approach taken was to reduce the complexity of the problem through the introduction of a two-step models [84,88,89]: a macroscopic low-frequency electromagnetic layout describing the response of human tissues of the arm to an exposure of injected currents through a set of electrodes (volume conductor model). The second, purely physiological, suitable for treating the muscular response in the presence of a field distribution induced by a matrix of active array. The present work has been focused on the synthesis of the first step.

In order to properly analyze the electromagnetic response of the arm is necessary to know the electric properties of the involved tissues. Given that we are dealing with human tissues that show no magnetic properties in the operating bandwidth [90], we characterized material parameters ion for the electrical permittivity and conductivity [91,92]. The frequency dependence

comes about because when a time-varying electric field is applied, the polarization response of the material cannot be instantaneous. Causality implies that the response has to follow the excitation, as predicted by Kramers-Kronig relations. The most remarkable consequence of these equations is that we cannot have a medium which has no losses for all the frequency spectrum, because the real part of its permittivity is inherently related to the imaginary part (whit takes into account the dissipation in the material). Finally if the material has unbounded conduction charge, remembering Ohm's law, we have to introduce also conductivity of the material.

Then the fundamental parameters for a characterization of the principal tissues to be involved in the model have been retrieved and analyzed in the frequency range of interest (from 10 Hz up to KHz):

1. Blood
2. Blood Vessel
3. Bone
4. Bone Marrow
5. Cartilage
6. Fat tissue
7. Muscle
8. Skin (dry and wet)

In particular, the dispersion for the electrical permittivity and for the electrical conductivity has been determined (both in their real and imaginary parts), as reported in Figure 4.1-4.8. The spectrum effective bandwidth has been derived from direct measurement. These materials have been integrated in the HUGO Anatomical Data Set available in [32], combining both the anatomical voxel and surface data set with the materials data set. The retrieval has been performed by using interpolation tools according to the first Chapter analysis. The values have been sampled matching also the data with the available literature [91-93].

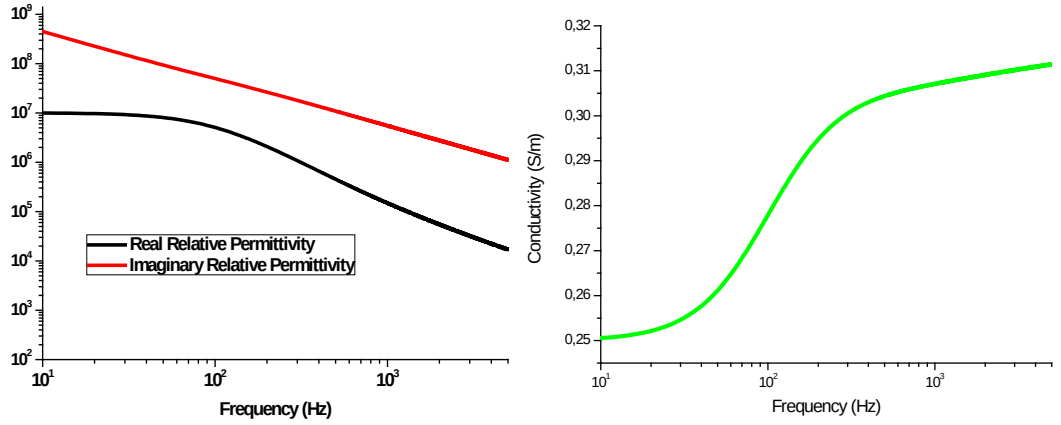

Figure 4.1 Frequency dispersion of the electric parameters of blood vessels.

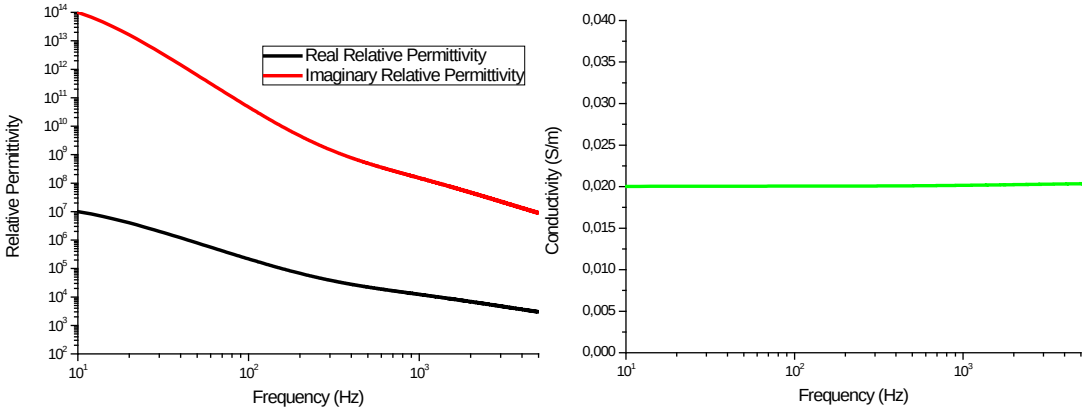

Figure 4.2 Frequency dispersion of the electric parameters modelling bone.

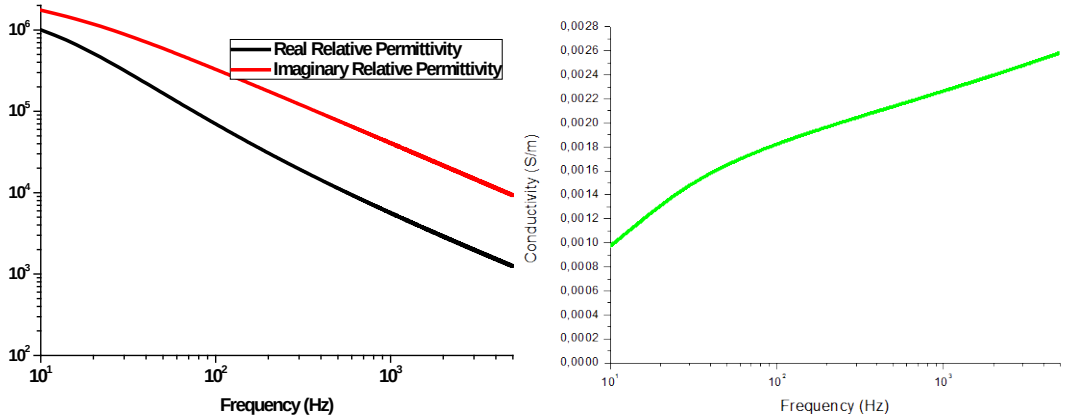

Figure 4.3 Frequency dispersion of the electric parameters modelling bone marrow.

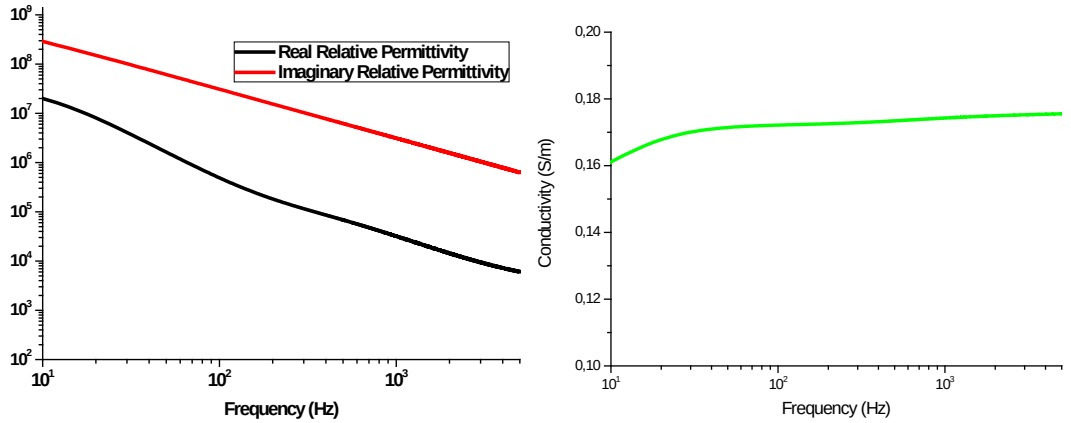

Figure 4.4 Frequency dispersion of the electric parameters modelling cartilage.

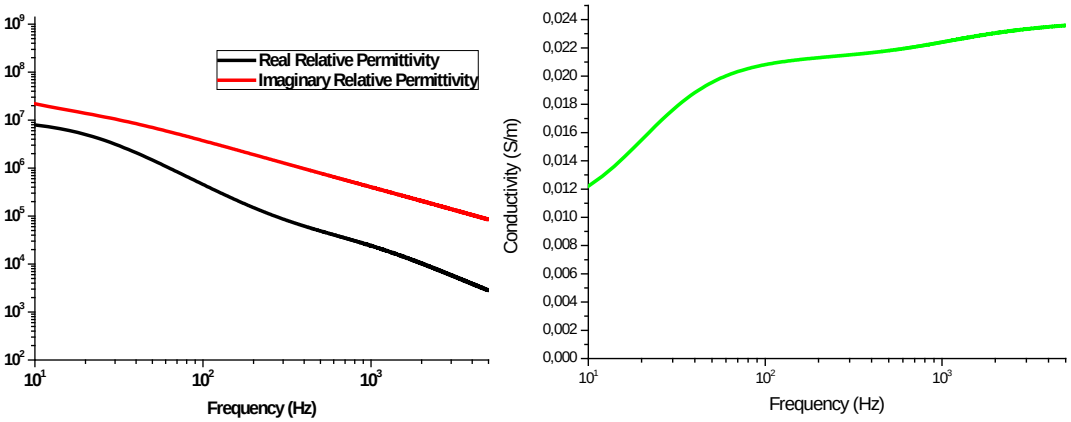

Figure 4.5 Frequency dispersion of the electric parameters modelling fat tissue.

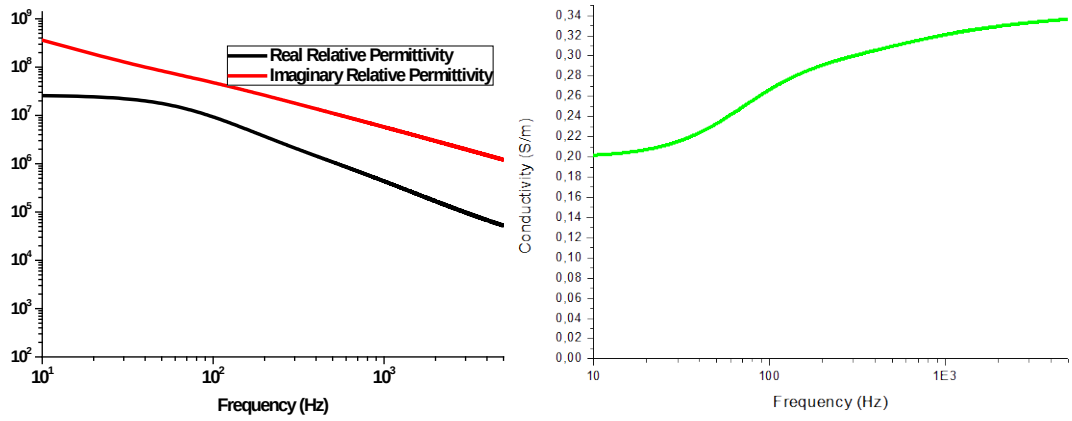

Figure 4.6 Frequency dispersion of the electric parameters modelling muscles.

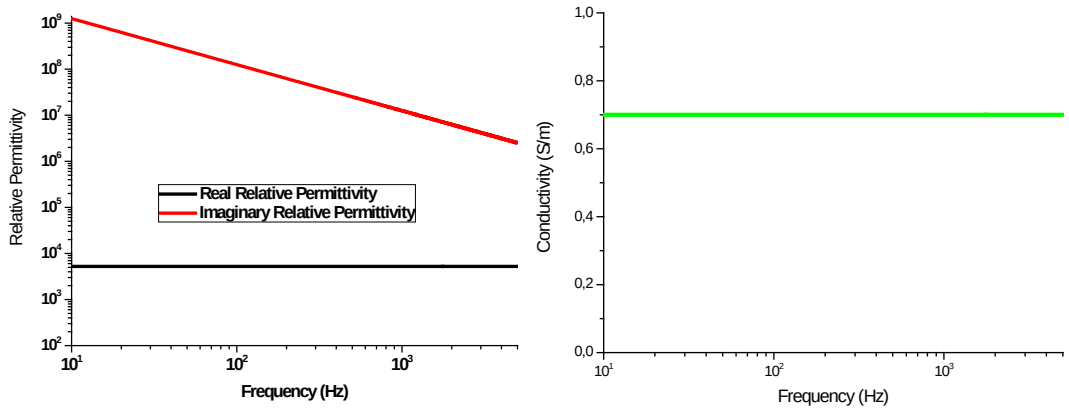

Figure 4.7 Frequency dispersion of the electric parameters of blood.

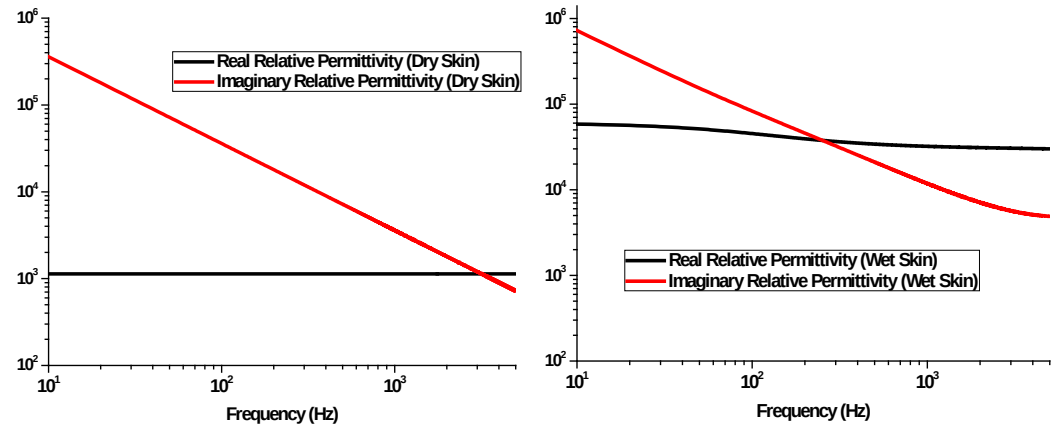

Figure 4.8 Frequency dispersion of the electric parameters of blood vessels.

From Figure 4.8, we can see that characterizatione also allow to treat different configurations on the basis of electromagnetic response of the tissue. For example wet may distinguish between dry or wet skin, in the case we apply an electrode directly or after humidifying the interested area, respectively. Moving to the discretization of the model, HUGO data set is categorized into 40 types of tissue with levels of detail starting from the smallest voxel size of 1x1x1 mm^3 up to 8x8x8 mm^3. Considering that the average adult skin thickness is close to 2-3 mm [84,91,92], the needed highest spatial resolution has been fixed to the smallest voxel size, in order to resolve also the thinnest details (Figure 4.9-4.10).

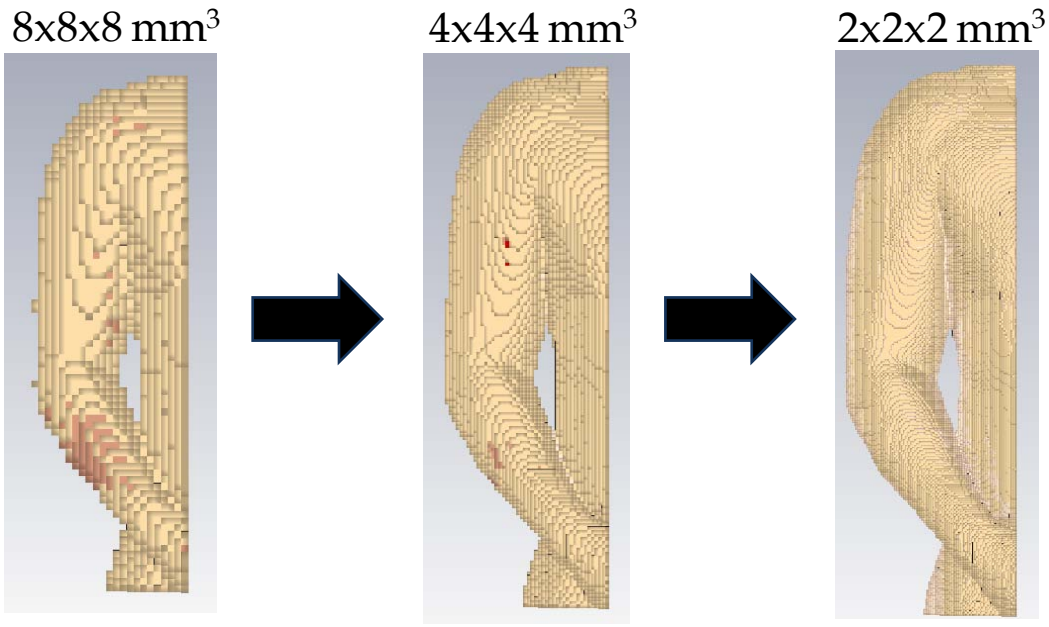

Figure 4.9 Voxel refinement in the anatomical modeling of the upper limb with discrete data set HUGO**.**

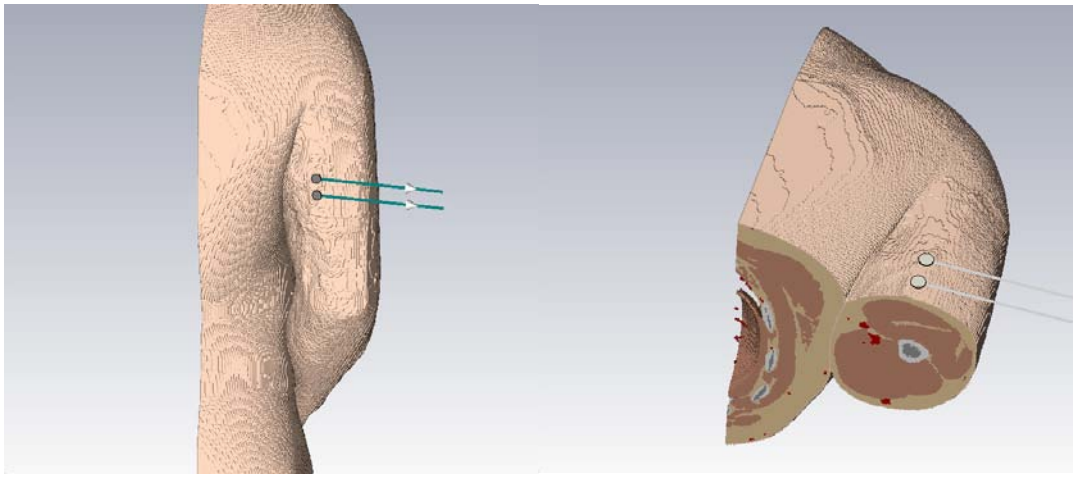

Figure 4.10 Anatomical modeling of the upper limb with discrete data set HUGO (two illustrative elecetrodes are introduced)**.**

The finite integration technique adopted to study the electromagnetic response of the arm is based on a macroscopic point of view (both the electric permittivity and conductivity are global parameters defining the electrical properties of inert media), so we can't include directly any active physiological behavior in it [94-96].

The simulator solving modules performances have been investigated numerically through two different schemes of discretization for Maxwell's

equations: a quasi-static approach and a full-wave analysis. Typically, static models only describe the effect of an amplitude change of the stimulation (variation of potential distribution inside the volume), implying that the result is substantially independent from the pulse duration (even if the pulse duration has an influence on the muscle activation) and neglecting also the dispersive behavior of involved media [90].

We used the transient quasi-static technique to avoid these issues modeling also the capacitive effects due to the electrical permittivity of materials. Even if the voxel model is compliant with the solver used, and it is thus possible to calculate the field distribution for a given excitation (Figure 4.11), the computational cost due to the solving of the entire structure is significantly high.

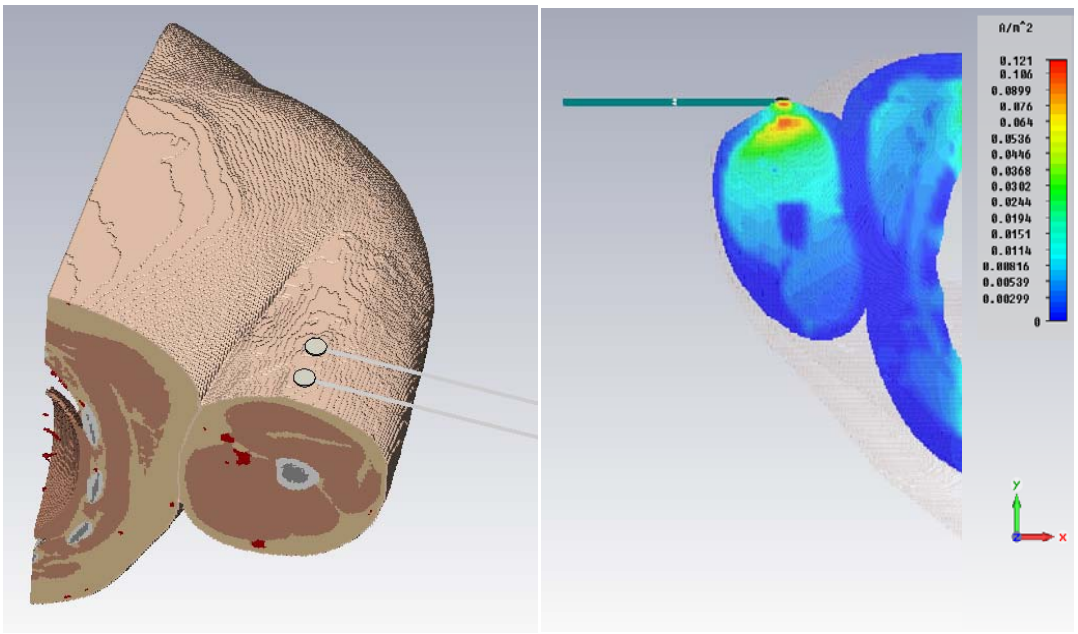

Figure 4.11 Discretization for the phantom model of the upper limb.

However, as shown in [84,91,92] by defininig a simplified geometry consisting of concentric layered cylindrical shells the loss in accuracy is slightly affected. An approximated model has been thenn defined to validate the solver accuracy and consistence, discretized with a tetrahedral meshing. This setup is based on a finite length cylindrical multilayered structure involving the following tissues: bone, bone marrow, cartilage, fat, muscle and skin, as depicted in the following Figures 4.12-13.

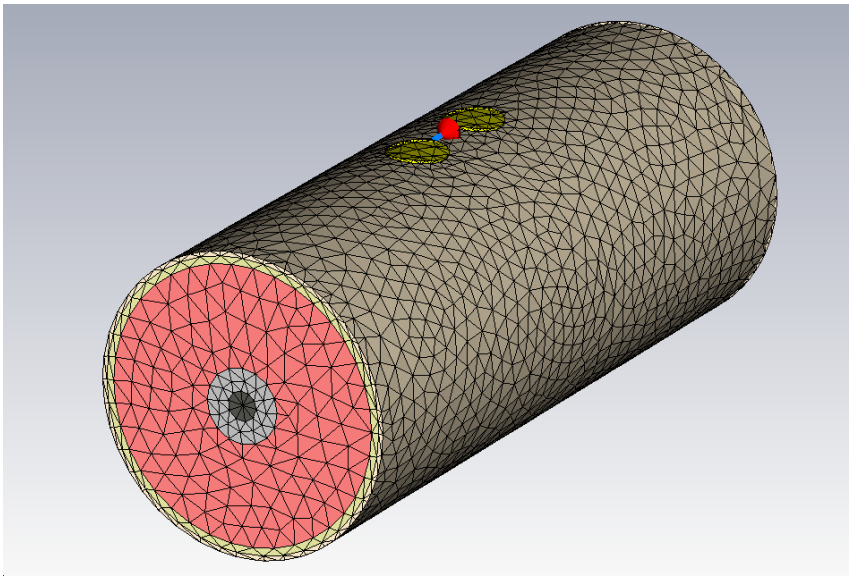

Figure 4.12 Discretization for the phantom model of the upper limb.

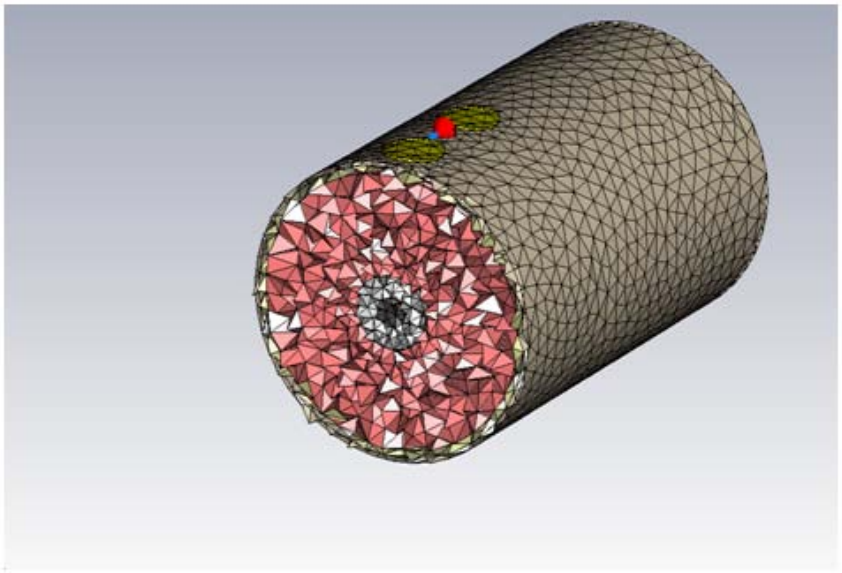

Figure 4.13 Discretization for the phantom model of the upper limb (mesh detail)**.**

The geometric anatomic details have been determined by averaging the values found in literature [84,91,92] and directly measured on in vivo tests, as summarized in the following scheme with reference to Figure 4.12:

- Arm radius: 43 mm
- Arm length: 200 mm
- Skin thickness: 1.5 mm
- Fat thickness: 6 mm
- Muscle thikness: 24.5 mm
- Bone radius: 11 mm
- Hydrogel thickness: 1 mm
- Electrodes thickness: 2 mm

The hydrogel electric characteristics have been derved fro standard solution referenced for example in [91,92]. Two silver circular electrode were initially considered, placed directly above the skin and excited by a biphasic square pulse, as in Figure 4.14. We parameterized the geometry respect to the electrodes position and relative distance to sweep the quantities and study their influence in the model. With the full-wave analysis we also managed to obtain an estimate of the input impedance at the electrode feed point.

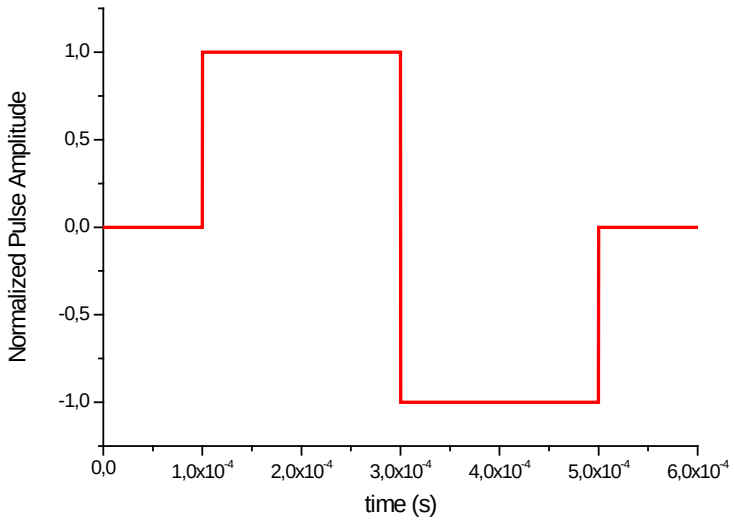

Figure 4.14 Time excitation pulse feeding the electrodes**.**

The interface between skin and electrode is managed by the boundary conditions, and the wet skin effects may be easily modeled by changing the

relative conductivity in the skin layer. We also defined an alternative setup in which an additional layer is placed between the electrode and the skin, modeling for example an adhesive gel. Al the involved materials may also show anisotropic behavior by properly defining different constitutive parameters in the coordinate spatial directions. In Figure 4.15 is reported the calculated current density distribution all over the simulated structure, by considering two Ag/AgCl electrodes with a diameter of 1.5 cm and relative distance of 2 cm; the amplitude of pulse has been varied from 5 mA up to 25 mA, with a duration lying within the range 100-1000 μs (with discrete steps of 50 μs). Similar result may be obtained for square electrodes.

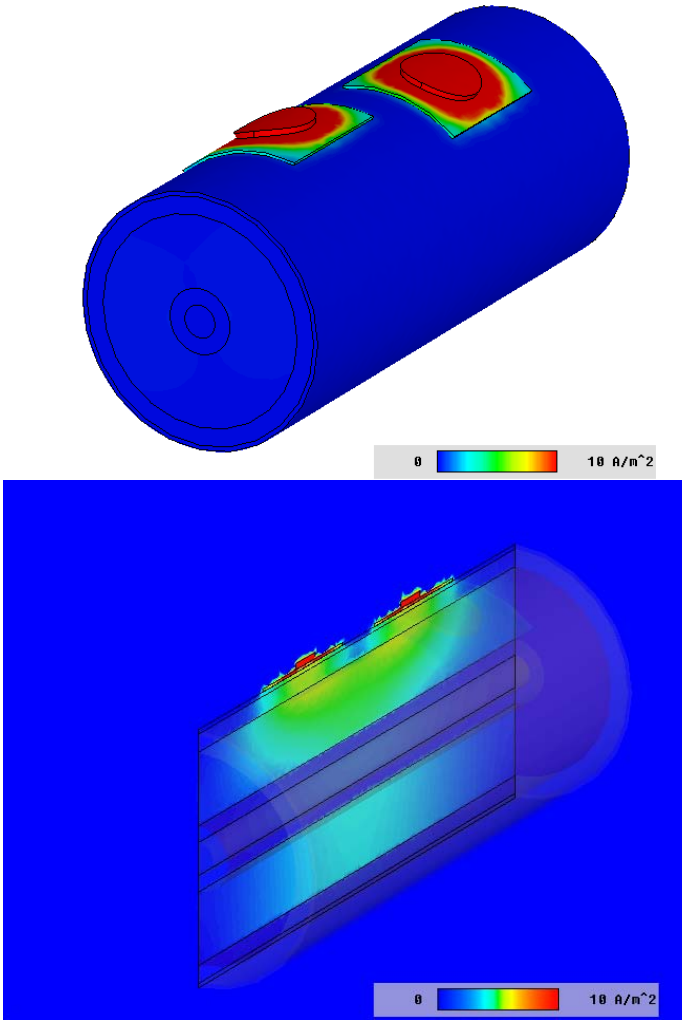

Figure 4.15 Current density distribution inside the phantom model uder simulated FES**.**

It is worth noticing tha this model offers the possibility to monitor the time evolution of the structure, in order obtain some indications about the electromagnetic response after the pulse stimulation. This is consistent with the idea of extending the simulation to the case of an arbitrary distribution of interacting electrodes. In fact, supposing the elements strongly interact, it is possible to apply the concept of the active array factor and using then the superposition principle. The electrodes have been designed perfectly adherent to the skin surface through a conformal deformation of the metallic patch (we considered a realistic Silver based metallization). The electromagnetic field distribution has been calculated in all the structure, including the eddy currents and the energy density.

The same simulations were performed both in time and frequency domain showing, as expected, that the frequency approach is the best in terms of computational cost (time domain solver are inherently slow at low frequencies).

Using the two step approach we studied the volume conductor representation to determine the electromagnetic field distribution inside the arm, and use it as an input excitation amplitude map for a physiological model describing the active cellular response and the generation of action potentials in human tissues. As shown in literature, several nerve models may be used to analyze the transcutaneous electrical stimulation response, starting from the volume conductor model and taking into account the nerve activation. Such models are based on a circuit representation of nerve bundles and the may be properly excited by applying voltage or current inputs [84,97,98,99]. The proposed model is able to provide the right input to an active nerve model describing the complex behaviour of the axons, depending on the spatio-temporal trend of the potential filed along nerve bundles. The link between the passive and the active model is then established by assigning the time dependent, spatially interpolated current density values computed through the passive model as excitation signals.

In order to validate the model, the interpolated values of the current density has been passed to the active model developed in [97-98]. Computing the motor units recruitment recruitment, that is the percentage of axons that are activated divided by all axons that innervate a certain muscle, it is possible

to derive strength duration curve (SDC), defined by the couple of values (surface stimulation pulse duration and pulse amplitude) corresponding to nerve recruitment over 10% [98,99].

By comparing the retrieved SDC with the ones obtained from experimental in-vivo tests performed on six healthy subjects whose biceps brachii has been electrically stimulated with the same previous electrode configuration, we can see that the model predicts a recruitment comparable with the measured response, even if some high order aspect related to discretization and characterization of the involved materials have not been taken into account [100,101].

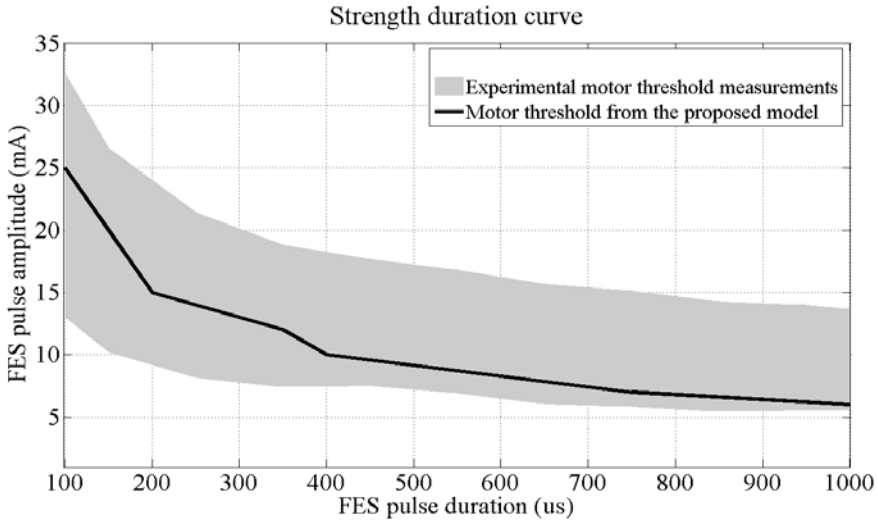

Figure 4.16 Comparison between strength duration curve obtained by in vivo measurements and the one predicted by the proposed model. Figure contained in [97].

Once the model has been validated we performed a set of simulations to compute the electrical field into the tissues by an arbitrary distributions of electrodes. This may assure the possibility to programmatically define the best electrode configurations for a selective and effective muscle contraction.

We thus extended the previous setup to the case of four coupled electrodes plus one reference, as reported in Figure 4.17. By increasing the number of active patches we may reduce the amplitude of the excitation of each electrode while keeping the same recruitment. This may result a crucial aspect when dealing with the comfort of the patient, especially if

considering that the fatigue and pain threshold are directly related to high values of injected currents.

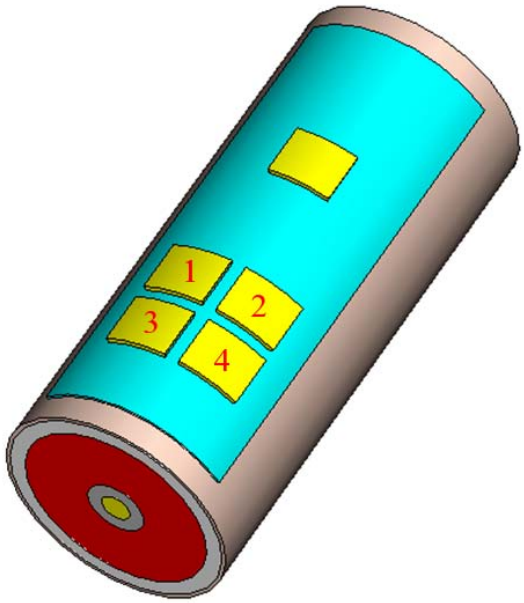

Figure 4.17 Array configuration based on four electrodes applied to the skiomparison between strength duration curves obtained by in vivo measurements and the one predicted by the proposed model. Figure contained in [97].

Looking at the field distribution, it is clear that, when feeding two elements of the array is it possible to sustain higher current density even if providing lower excitation amplitude. In Figure 4.18 are compared simulated current density for two array (left panel) and a matrix of two fed patches (1-4 according to Figure 4.17).

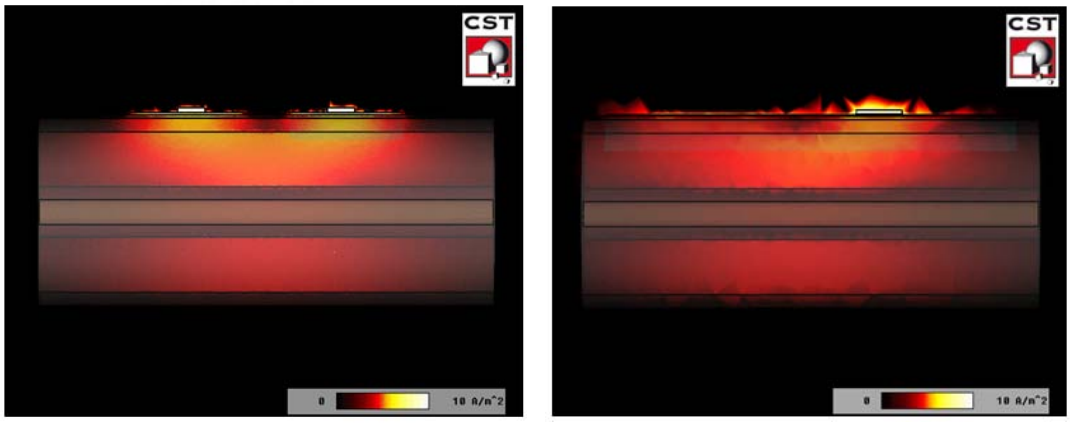

Figure 4.18 Current denstiy distribution two electrodes (left) and an array of four elements plus the reference (right).

Adding other element to the excitation pattern, we can furtherly increase the current density distribution (Figure 4.19), thus preserving the recruitment.

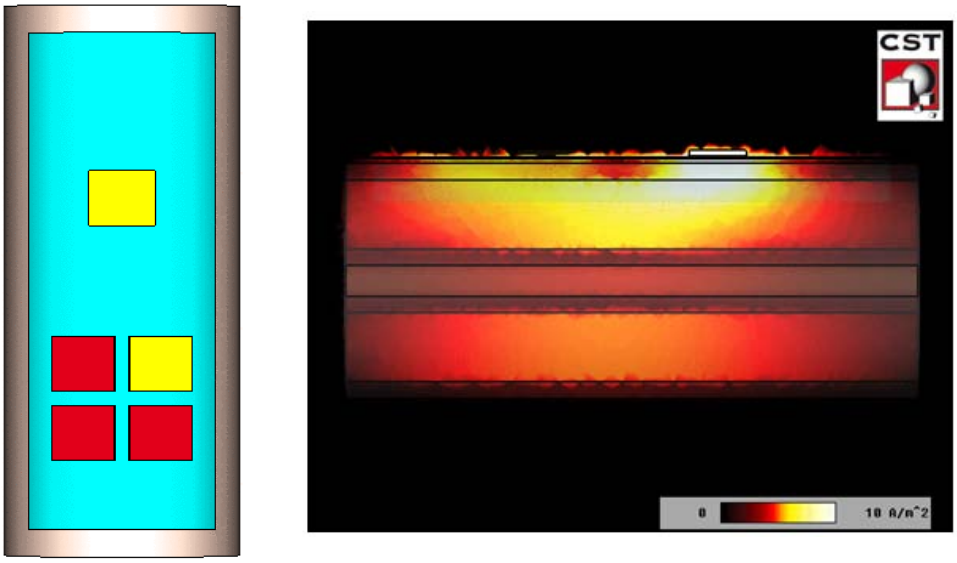

Figure 4.19 Current denstiy distribution for the specified exctitation pattern.

We have also analized variation in the electrode shape (Figure 4.20). Due to the quasi-static nature of the problem this only produce some slight changes in the local distribution of the current density, as shown in Figure 4.21.

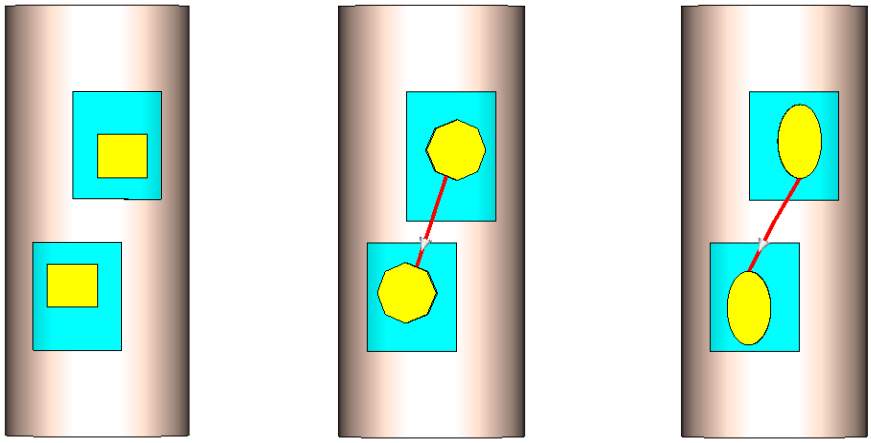

Figure 4.20 Different electrode shapes used in the simulation setups.

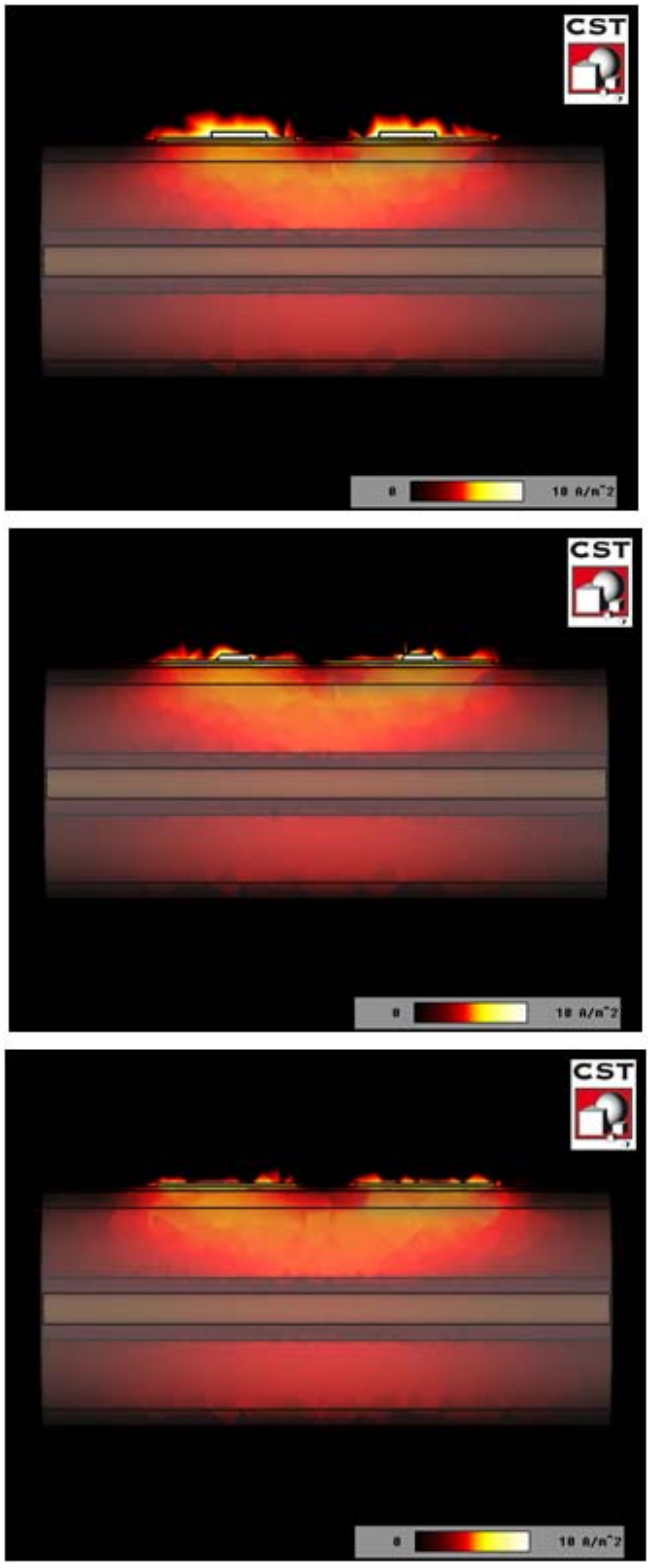

Figure 4.21 Current density distribution for different electrode shapes following the order reported in Figure 4.20.

Finally we tested the proposed model for a very large number of active elements. The model converges to a stable solution according to the previous results, as shown in Figure 4.22. Moreover with large array configuration the proposed layout alow to properly choose the excitation of each single electrode, varying not only the amplitude and duration of the stimulous but also the time shift among each other. This may allow to simulate multisequential FES sessions with a progressive activation of the excitation grid according to a given time pattern.

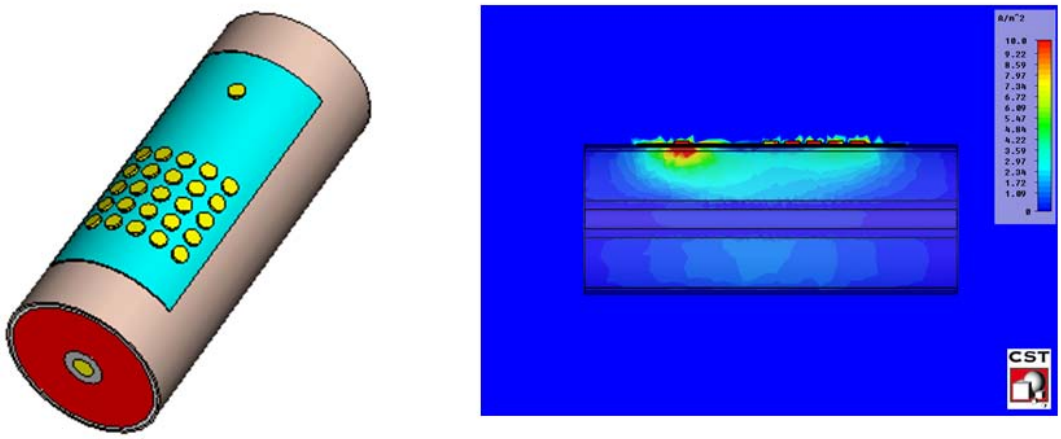

Figure 4.22 Different electrode shapes used in the simulation setups.

4.2 Cloaking aperture-less NSOM tips

Plasmonic covers investigated in the previous Chapter may be successfully used to enhance the performance of near-field scanning optical microscopy (NSOM) systems based on the employment of aperture-less metallic tip probes, which are commonly employed to acquire high-resolution images of nano-particles, electrically small samples or corrugated surfaces [102].

Though the light scattering by the probe extremity is necessary for the correct operation of the NSOM system, the additional scattering due to the whole probe affects the signal-to-noise ratio and, thus, the resolution of the acquired image. By covering the whole probe, except for its extremity, the unwanted scattering can be effectively reduced. The covering material should be designed in order to significantly reduce the undesired scattering contribute due to the strongly plasmonic behavior of the tip.

The system is based on a metallic tip which scans the interest area to get the high-resolution image. In this case, the tip works in the so-called scattering mode, that is when illuminated by an external source, the strong scattered field due to the tip end interacts with the sample to be imaged and enhances its near-field features, allowing the acquisition of an high-resolution image in the far field. However, the resolution of the aperture-less NSOM tip is affected by the unwanted scattering contribution due to the whole probe. Light source beams, in fact, cannot be collimated to exhibit a footprint comparable with the tip end. Therefore, even a great part of the probe, which does not interact with the sample at all, generates scattering contributions reaching the far-field and deteriorating the signal-to-noise ratio and, consequently, the resolution of the acquired image.

The idea is to use the scattering cancellation approach introduced in the prebious chapter to enhance the resolution of the NSOM systems based on aperture-less tips [103]. Here, the invisibility cloak covers the aperture-less NSOM probe, except for its extremity, in order to preserve the strong field enhancement due to the plasmonic nature of the tip and the interaction between the tip itself and the sample. The total covering of the tip with a plasmonic cover, as previously presented for the classical scattering cancellation approach, is not applicable here because it would suppress the strong interaction of the tip with the sample. By cloaking the rest of the probe the plasmonic enhancement is preserved, while significantly reducing the scattering from the whole probe, increasing, thus, the signal-to-noise ratio in the far-field.

By directly comparing the layout of the bare probe with the one covered by the designed covver, it is shown that the scattering by the very tip of the probe (and, thus, the sample-probe interaction) is preserved, while the field amplitude along the probe body, which is responsible for the undesired scattering contributions in the far-field, is effectively reduced. As expected, in the proposed layout the scattering cancellation approach allows to significantly enhance the resolution performance of NSOM systems employing aperture-less metallic tips by reducing the undesired scattering contribution from the tip itself, as reported in [103]. This may lead to several new applications exploiting the scattering free behavior of plasmonic cloaking devices to synthesize high resolution imaging systems.

5. CONCLUSIONS

In this work we studied the design and synthesis of MTMs both at microwaves and optical frequencies, analyzing the theoretical aspects related to the modeling of such complex media and to the manufacturing issues arising when implementing real life setups. We proposed a properly derived hybrid procedure to retrieve the effective permittivity and permeability of planar metamaterial samples relying on the combined use of parametric models and TR techniques.

We have then applied the MTM characterization to the design of electromagnetic cylindrical cloaks working in both the fundamental polarizations. We have also presented the design of electromagnetic cylindrical and spherical cloaks working at optical frequencies using layered structures of plasmonic and non-plasmonic materials, obtaining the desired dispersive behaviors at the visible frequencies, allowing the actual synthesis of the cloaking devices considering also the effect of the losses.

Successively, we extended here the scattering cancellation technique to the case of arbitrarily shaped objects with anisotropic scattering. We have shown how homogeneous covers may be successfully used to cloak moderately sized objects, even when the dipolar scattering contribution is not necessarily dominant. Our findings show that a conformal shape is the ideal solution to achieve weak dependence of the scattering reduction upon the polarization of the impinging illumination. Our results ensure that the plasmonic cloaking technique may be applied also to strongly anisotropic dielectric, plasmonic or conducting objects, by properly tailoring the shape and design of the cloaking plasmonic layer.

We proposed then a theoretical analysis combining optical force calculation to the electromagnetic cloaking formulation, in order to gain further physical insights and explore new possibilities for the manipulation of nano-particles. First, we have shown that the same conditions used to make spherical and cylindrical nano-particles invisible to the electromagnetic field by using the scattering cancellation approach, can be straightforwardly employed also to minimize gradient and scattering optical forces exerted by the illuminating field on the same covered nano-particles. These results have been verified through proper full-wave simulations considering

properly both dispersion and losses of the plasmonic materials used to design the cloaks. We have also extended our speculation to the case of optical torques exerted on spheroidal and cylindrical Rayleigh particles, deriving the conditions to obtain stable equilibrium positions. This investigation led to the interesting result that, anomalously, the usual unstable equilibrium positions of uncovered particles may turn out to be stable ones when properly covering the particles. The additional degrees of freedom introduced by the plasmonic cloaking may be of interest in many nanotechnology applications. In order to apply the proposed theoretical speculations to more complex cases, we have derived the conditions for minimizing optical forces exerted on a cloaked Rayleigh particle placed above a dielectric half-space. Such results may be straightforwardly extended to typical configurations used in several application fields, to obtain, for instance, improved biological sensing, optical trapping and probing.

As further applications, by exploting the characterization techniques presented here, a robust and accurate transient quasi-static passive model of the upper limb has been presented. The model describes the tissues response to surface electrical stimulation, providing the overall electromagnetic field distribution. The model may be successfully used to determine the current and potential distributions inside the arm for an optimal design of a functional electrical stimulation based tremor suppression system.

Finally, the scattering cancellation approach has been applied to significantly enhance the resolution performance of NSOM systems employing aperture-less metallic tips by reducing the undesired scattering contribution from the tip itself.

6. LIST OF PUBLICATIONS

6.1 Journal Papers

[1] **F. Bilotti, S. Tricarico, F. Pierini, and L. Vegni,** "Cloaking apertureless near-field scanning optical microscopy tips," Optics Letters, Vol. 36, No. 2, 211-213, 2011.

[2] **S. Tricarico, F. Bilotti, L. Vegni**, "Reduction of optical forces exerted on nano-particles covered by scattering cancellation based plasmonic cloaks," Physical Review B, 82, 045109, 2010 – Selected Also For The Virtual Journal Of Nanoscale Science & Technology, Vol. 22, No. 4

[3] **F. Bilotti, S. Tricarico, and L. Vegni**, "Plasmonic Metamaterial Cloaking at Optical Frequencies," IEEE Transactions On Nanotechnology, vol. 9, 56-61, 2010, ISSN: 1536-125X

[4] **L. Scorrano, S. Tricarico, F. Bilotti,** "Resonating plasmonic particles to achieve power transmission enhancement," IEEE Photonics Technology Letters, 2010, ISSN: 1041-1135

[5] **S. Tricarico., F. Bilotti, A. Alù, L. Vegni,** "Plasmonic Cloaking for Irregular Objects with Anisotropic Scattering Properties," Physical Review E, Statistical, Nonlinear, And Soft Matter Physics, 2010, ISSN: 1539-3755

[6] **S. Tricarico, F. Bilotti, L. Vegni,** "Multi-functional dipole antennas based on artificial magnetic metamaterials," IET Microwaves, Antennas & Propagation, 2010, ISSN: 1751-8725

[7] **S. Tricarico, F. Bilotti, L. Vegni**, "Plasmonic and Non-Plasmonic Layered Structures for Cloaking Applications at Visible Frequencies," Microwave And Optical Technology Letters, vol. 51; 2713-2717, 2009, ISSN: 0895-2477

[8] **S. Tricarico, F. Bilotti, L. Vegni**, "Scattering Cancellation by Metamaterial Cylindrical Multilayers," Journal Of The European Optical Society, vol. 4, 2009, ISSN: 1990-2573

[9] **F. Bilotti, S. Tricarico, L. Vegni**, "Electromagnetic Cloaking device for TE and TM polarizations," New Journal Of Physics, 2009, ISSN: 1367-2630

6.2 Book Chapters

[1] **S. Tricarico, F. Bilotti, L. Vegni**, "Metamaterials Characterization Through Effective Parameters Retrieval," Studies in Applied Electromagnetics and Mechanics, vol. 34, IOS PRESS, 2010, ISBN 978-1-60750-603-4 (print) 978-1-60750-604-1 (online)

6.3 Conference Papers

[1] **F. Bilotti, S. Tricarico, L. Vegni**, "The role of plasmonic covers to enhance the resolution of aperture and aperture-less NSOM tips" 3rd International Topical Meeting on Nanophotonics and Metamaterials. Seefeld, Austria, 3-6 January 2010

[2] **S. Tricarico, F. Bilotti, L. Vegni,** "Scattering Cancellation Based Actual Cloaking Devices". Proceedings of 20th International Conference on Applied Electromagnetics and Communications – ICECom 2010. Dubrovnik, Croatia, 20-23 September 2010

[3] **F. Bilotti, S. Tricarico, L. Scorrano, and L. Vegni**, "Enhancement of NSOM tip performances through the employment of metamaterials". Proceedings of the Fourth International Congress on Advanced Electromagnetic Materials in Microwaves and Optics - Metamaterials 2010. Karlsruhe, Germany, 13-16 September 2010

[4] **F. Bilotti, S. Tricarico, L. Vegni**, "Applications of metamaterial cloaking". Proceedings of 12th International Ceramics Congress and 5th Forum on New Materials. Italy, Montecatini, 6-18 June 2010

[5] **M. Goffredo, S. Conforto, M. Schmid, S. Tricarico, F. Bilotti, L. Vegni, and T. Dalessio**, "Modelling arm behaviour under surface electrical stimulation". Proceedings of Secondo Congresso Nazionale di Bioingegneria (GNB2010). Torino, Italy, 8-10 July 2010

[6] **M. Goffredo, S. Tricarico, L. Schinaia, M. Schmid, S. Conforto, T. Dalessio** (2010). "Active model of nerves in the upper limb under surface electrical stimulation". Proceedings of XVIII Edition of the International Society of Electrophysiology and Kinesiology (ISEK). Aalborg, Denmark, 16-19 June

[7] **S. Tricarico, F. Bilotti, L. Vegni**, "Scattering cancellation approach to cloaking: new applications". Proceedings of SPIE Photonics Europe 2010, Conference EPE101 – Metamaterials. Brussels, Belgium, 12-16 April 2010 (*invited*).

[8] **S. Tricarico, F. Bilotti, L. Vegni**, "Design of a Multi-Functional Metamaterial Inspired Dipole Antenna". Proceedings of 40th European Microwave Conference. Paris, France, 26 September – 1 October 2010

[9] **S. Tricarico, F. Bilotti, L. Vegni,** "Multi-functional metamaterial-inspired antennas for mobile communications". Proceedings of Proceedings of the Fourth International Congress on Advanced Electromagnetic Materials in Microwaves and Optics – Metamaterials 2010. Karlsruhe, Germany, 13 – 18 September 2010

[10] **S. Tricarico, F. Bilotti, L. Vegni,** "Optical forces on Rayleigh particles covered by metamaterial shells". Proceedings of Proceedings of the Fourth International Congress on Advanced Electromagnetic Materials in Microwaves and Optics – Metamaterials 2010. Karlsruhe, Germany, 13 – 18 September 2010

[11] **S. Tricarico, F. Bilotti, L. Vegni,** "Electromagnetic cloaking Devices: Design and Possible Applications". Proceedings of XVIII Riunione Nazionale di Elettromagnetismo Applicato. Italy, Benevento, 6-10 Settembre 2010

[12] **S. Tricarico, M. Goffredo, F. Bilotti, T. Dalessio, L. Vegni,** "Transient quasi-static passive model of the upper limb under surface electrical stimulation: finite integration based approach". Proceedings of XVIII Edition of the International Society of Electrophysiology and Kinesiology (ISEK). Aalborg, Denmark, 16-19 June 2010

[13] **L. Scorrano, S. Tricarico, F. Bilotti, L. Vegni**, "Design of optical nano-antenna reflectors through dielectric structures with extreme-valued constitutive parameters". Proceedings of Proceedings of the 3rd EOS Topical Meeting on Optical Microsystems (OμS09). Capri, Italy, 27 - 30 September 2009

[14] **S. Tricarico, F. Bilotti, L. Vegni,** "Scattering Reduction with Plasmonic Covers at Optical Frequencies". Proceedings of 2nd European Topical Meeting on Nanophotonics and Metamaterials Nanometa. Seefeld Tirol, Austria, 5 - 8 January 2009

[15] **S. Tricarico, F. Bilotti, A. Alù, L. Vegni,** "Design of Plasmonic Covers to Cloak Arbitrarily-Shaped Objects". Proceedings of Proceedings of the Third International Congress on Advanced Electromagnetic Materials in Microwaves and Optics – Metamaterials 2009. London, UK, 30 August – 4 September 2009

[16] **S. Tricarico, F. Bilotti, L. Vegni**, "Improved Biological Sensing through Electromagnetic Cloaking". Proceedings of Proceedings of the 8th International Symposium on Electric and Magnetic Fields (EMF'09). Mondovì, Italy, May 26-29 2009

[17] **S. Tricarico, F. Bilotti, L. Vegni**, "Radiation Pressure Exerted Over Cloaked Nanoparticles: Theory and Applications". Proceedings of Fourth International Conference on Surface Plasmon Photonics (SPP4). Amsterdam, The Netherlands, 21-26 June 2009

[18] **S. Tricarico, F. Bilotti, L. Vegni,** "Metamaterials Characterization Through Effective Parameters Retrieval". Proceedings of Proceedings of the XIV International Symposium on Electromagnetic Fields in Mechatronics, Electrical and Electronic Engineering (ISEF 2007). Arras, France, 10-12 September 2009

[19] **S. Tricarico, F. Bilotti, L. Vegni**, "Optical cloaking with cylindrical plasmonic implants". Proceedings of Proceedings of the 11th International Conference on Electromagnetics in Advanced Applications – ICEAA 2009. Torino, Italy, 14-18 September 2009

[20] **S. Tricarico, F. Bilotti, L. Vegni**, "Actual cloaking devices operating at optical frequencies". Proceedings of Proceedings of the 3rd EOS Topical Meeting on Optical Microsystems (OμS09). Capri, Italy, 27 - 30 September 2009

[21] **S. Tricarico, F. Bilotti, And L. Vegni,** "A Genetic Algorithm based procedure to retrieve effective parameters of planar metamaterial samples". Proceedings of Proceedings of SPIE Europe Optics and Optoelectronics. Prague, Czech Republic, 20-24 April 2009

[22] **F. Aznar, J. Bonache, F. Martín, B. Alici, K. Aydin, E. Ozbay, F. Bilotti, S. Tricarico, L. Vegni**, "Miniaturization and characterization of metamaterial resonant particles". Proceedings of 38th European Microwave Conference, Amsterdam. Amsterdam, The Netherlands, 27-31 October 2008

[23] **F. Bilotti, S. Tricarico, L. Vegni,** "Multi-functional antennas with artificial magnetic materials: theoretical aspects and numerical simulations". Proceedings of Second International Congress on Advanced Electromagnetic Materials in Microwaves and Optics. Pamplona, Spain, 21-26 September 2008

[24] **F. Bilotti, S. Tricarico, L. Vegni,** "Optical cloaking with metamaterials". Proceedings of EOS Topical Meeting on Nanophotonics, Photonic Crystals and Metamaterials - TOM 3. Paris, France, 29 September – 2 October 2008

[25] **S. Tricarico, F. Bilotti, L. Vegni,** "Parametric models for retrieving effective parameters of planar metamaterial samples". Proceedings of 2nd Young Scientist Meeting on Metamaterials. Barcelona, Spain, 7-8 February 2008

[26] **S. Tricarico, F. Bilotti, And L. Vegni,** "Scattering cancellation based cloaking devices at microwave and optical frequencies," Proceedings

of the IV Workshop on metamaterials and special materials for electromagnetic applications and TLC. Napoli, Italy, 18-19 December 2008.

7. ACKNOWLEDGMENTS

The author would like to acknowledge the ESA Ariadna Program, the Applied electromagnetic Laboratory and the Biolab of Univeristy Roma Tre for their support. The author also wishes to deeply thank Prof. Lucio Vegni and Prof. Filiberto Bilotti for their constant support and contribution without which the writing of this work would not have been possible.

8. REFERENCES

[1] http://www.metamorphose-vi.org

[2] N. Engheta, R.W. Ziolkowski, *Metamaterials: Physics and Engineering Explorations*, New York, Wiley, 2006.

[3] A. Alù et al., "*Single-Negative, Double-Negative, and Low-index Metamaterials and their Electromagnetic Applications*," IEEE Trans. Ant. & Prop. Mag., vol. 49, 23-36, 2007.

[4] A. Sihvola, S. Tretyakov and A. de Baas, "*Metamaterials with extreme material parameters,*" J. Comm. Tech. Electron., vol. 52, 986-990, 2007.

[5] V. Veselago, "*Electrodynamics of substances with simultaneously negative values of ε and μ*," Sov. Phys. Usp. 10 (4), 509–14, 1964.

[6] J. B. Pendry et al., "*Extremely low frequency plasmons in metallic mesostructure*," Phys. Rev. Lett., 76, 4773, 1996.

[7] J. B. Pendry et al., "*Magnetism from conductors and enhanced nonlinear phenomena*," IEEE Trans. Microwave Theory Tech., 47, 2075, 1999.

[8] R.A. Shelby, D.R. Smith, S. Schultz, "*Experimental Verification of a Negative Index of Refraction*," Science 6, 77-79, 2001.

[9] C. Bohren and D. Huffinann, *Absorption and Scattering of Light by Small Particles*, New York, Wiley, 1983.

[10] D. R. Smith and J. B. Pendry, "*Homogenization of metamaterials by field averaging*," J. Opt. Soc. Am. B 23, 391, 2006.

[11] C. R. Simovski, P. A. Belov, "*Backward wave region and negative material parameters of a structure formed by lattices of wires and split-ring resonators*," IEEE Trans. Ant. & Prop., vol. 51, no. 10, 2003.

[12] C. R. Simovski, B. Sauviac, "*Role of wave interaction of wires and split-ring resonators for the losses in a left-handed composite*," Phys. Rev. E, 046607, 2004

[13] A. H. Sihvola, *Electromagnetic mixing formulas and applications*, IEE Press, 1999.

[14] R. W. Ziolkowski, "*Design, fabrication, and testing of double negative metamaterials,*" IEEE Trans. Ant. & Propag., vol. 51, 2003.

[15] F. Mariotte, S. A. Tretyakov, B. Sauviac, "*Modelling effective properties of chiral composites,*" IEEE Ant. & Prop. Mag., vol. 38, 22-32, 1996.

[16] C. R. Simovski, P. A. Belov, "*On homogenization of electromagnetic crystals formed by uniaxial resonant scatterers*," Phys. Rev E, vol. 72, 026615, 2006.

[17] D. R. Smith, D. Shurig, "*Modal analysis of finite-thickness slab with single-negative material parameters*," Phys. Rev. Lett. 90, 077405, 2003.

[18] A. Nicolson, "*Measurement of the intrinsic properties of materials by time domain techniques*," IEEE Trans. Instrum. Meas., vol. 17, 395-402, 1968.

[19] W. Weir, "*Automatic measurement of complex dielectric constant and permeability at microwave frequencies*," Proc. IEEE, vol. 62, 33-36 1974.

[20] M. G. Silveirinha, "*Transverse-average field approach for the characterization of thin metamaterial slabs*," Phys. Rev. E 75, 036613, 2007.

[21] X. Chen et al., "*Retrieval of the effective constitutive parameters of bianisotropic metamaterials*," Phys. Rev. E 71, 046610, 2005.

[22] C.R. Simovski, and S.A. Tretyakov, "*Local constitutive parameters of metamaterials from an effective-medium perspective,*" Phys. Rev. B 75, 195111, 2007.

[23] F. Bilotti and L. Vegni, "*From metamaterial-based to metamaterial-inspired miniaturized antennas: a possible procedure and some examples*," 2008 URSI General Assembly, CD-Digest, Chicago, USA, 7-16 August 2008.

[24] E. Ni, "*An uncertainty analysis for the measurement of intrinsic properties of materials by the combined transmission-reflection method*," IEEE Trans. Instrum. Meas., Vol. 41, No. 4, 1992.

[25] X. Chen, T. M. Grzegorczyk et al., "*Robust method to retrieve the constitutive effective parameters of metamaterials*," Phys. Rev. E, Vol. 70, 016608, 2004.

[26] A. N. Grigorenko, A. K. Geim, H. F. Gleeson, Y. Zhang, A. A. Firsov, I. Y. Khrushchev, and J. Petrovic, "*Nanofabricated media with negative permeability at visible frequencies*," Nature 438, 2005.

[27] A. N. Grigorenko, "*Negative refractive index in artificial metamaterials*," Opt. Lett. 31, 2006

[28] G. A. Deschamps, "*Determination of Reflection Coefficients and Insertion Loss of a Waveguide Junction*," J. Appl. Phys., vol. 24, 1046-1051, 1953.

[29] M. S. Freeman, R. N. Nottenburg, and J. B. DuBow, "*An Automated Frequency Domain Technique for Dielectric Spectroscopy of Materials*," J. Phys. E: Sri. Instrum., vol. 12, 899-903, 1977.

[30] J. Barker-Jarvis, E. J. Vanzura, "*Improved Technique for Determining Complex Permittivity with the Transmission/Reflection Method*," IEEE Trans. Microwave Theory and Tech., vol. 38, no. 8, August 1990.

[31] Mathematica© 6.0, Wolfram Research, Inc., www.wolfram.com

[32] CST Microwave Studio™ 5.0, CST of America, Inc., www.cst.com

[33] S. S. Stuchly and M. Matuszawski, "*A Combined Total Reflection-Transmission Method in Application to Dielectric Spectroscopy*," IEEE Trans. Instrum. Meas., vol. IM-27, 285-288, 1978.

[34] L. P. Ligthart, "*A Fast Computational Technique For Accurate Permittivity Determination Using Transmission Line Method*," IEEE Trans. Microwave Theory and Tech., vol. MTT-31, 249-254, 1983.

[35] F. Bilotti, A. Toscano and L. Vegni, "*Design of Spiral and Multiple Split-Ring Resonators for the Realization of Miniaturized Metamaterial Samples*," IEEE Trans. Ant. & Prop., Vol. 55, No. 8, 2007.

[36] MATLAB®, The MathWorks, Inc., www.mathworks.com

[37] G.W. Milton and N.A. Nicorovici, "*On the cloaking effects associated with anomalous localized resonances,*" Proc. Roy. Soc. A 462, 3027-3059, 2006.

[38] J.B. Pendry, D. Schurig, and D.R. Smith, "*Controlling Electromagnetic Fields,*" Science 312, 1780, 2006.

[39] D. Schurig, J.J. Mock, B.J. Justice, S.A. Cummer, J.B. Pendry, A.F. Starr, and D.R. Smith, "*Metamaterial Electromagnetic Cloak at microwave frequencies,*" Science 314, 977, 2006.

[40] U. Leonhardt, "*Optical conformal mapping,*" Science 312, 1777-1780 (2006).

[41] W. Cai, U.K. Chettiar, A.V. Kildishev, and V.M. Shalaev, "*Optical cloaking with metamaterials,*" Nat. Photonics 1, 224-227, 2007.

[42] Y. Luo, J. Zhang, B. Wu, and C. Hongsheng, "*Interaction of an electromagnetic wave with a cone-shaped invisibility cloak and polarization rotator,*" Phys. Rev. B 78, 125108, 2008.

[43] A. Alù and N. Engheta, "*Achieving transparency with plasmonic and metamaterial coatings,*" Phys. Rev. E 72, 016623, 2005.

[44] A. Alù, and N. Engheta, "*Plasmonic and metamaterial cloaking: physical mechanisms and potentials,*" J. Optics Opt. A 10, 093002, 2008.

[45] A. Alù and N. Engheta, "*Plasmonic materials in transparency and cloaking problems: mechanism, robustness, and physical insights,*" Opt. Expr. 15, 3318, 2007.

[46] A. Alù and N. Engheta, "*Cloaking and transparency for collections of particles with metamaterial and plasmonic covers,*" Opt. Expr. 15, 7578, 2007.

[47] S. Tricarico, F. Bilotti, A. Alù and L. Vegni, "*Plasmonic cloaking for irregular objects with anisotropic scattering properties,*" Phys. Rev. E 81, 026602, 2010.

[48] A. Alù, and N. Engheta, "*Effects of Size and Frequency Dispersion in Plasmonic Cloaking,*" Phys. Revi. E 78, 045602(R), 2008.

[49] M. G. Silveirinha, A. Alù, and N. Engheta, "*Parallel plate metamaterials for cloaking structures,*" Phys. Rev. E 75, 036603, 2007.

[50] F. Bilotti, S. Tricarico and L. Vegni, "*Electromagnetic cloaking devices for TE and TM polarizations,* New J. Phys. 10, 115035, 2008.

[51] F. Bilotti, S. Tricarico and L. Vegni, "*Plasmonic metamaterial cloaking at optical frequencies,*" IEEE Trans. Nanotech. 9, 55, 2010.

[52] M.G. Silveirinha, A. Alù and N. Engheta, "*Infrared and optical invisibility cloak with plasmonic implants based on scattering cancellation,*" Phys. Rev. B 78, 075107, 2008.

[53] C. A. Balanis, *Advanced Electromagnetic Engineering*, Wiley, Hoboken, 1989.

[54] D. Jackson, *Classical Electrodynamics*, Wiley, New York, 1998.

[55] L. Tsang, and J. A. Kong, *Scattering of Electromagnetics Waves Theory and Applications*, Wiley, New York, 2000.

[56] S. Tricarico, F. Bilotti, and L. Vegni, "*Scattering cancellation by metamaterial cylindrical multilayers,*" J. Europ. Opt. Soc. Rap. Public. 4, 09021, 2009.

[57] B. Wood, J.B. Pendry, and D.P. Tsai, "*Directed subwavelength imaging using a layered metal-dielectric system,*" Phys. Rev. B, Vol. 74, 115116, 2006.

[58] S.M. Rytov, "*Electromagnetic properties of a finely stratified medium,*" Sov. Phys. JETP, Vol 2., pp. 466–475, 1955.

[59] D. Bergman, "*The dielectric constant of a composite material - a problem in classical physics,*" Phys. Rep., Phys. Lett. 43, 377, 1978.

[60] D.R. Lide, *Handbook of Chemistry and Physics*, CRC Press, 2003.

[61] Edward D. Palik, *Handbook of Optical Constants of Solids*, Academic Press, 1998.

[62] W. Jiang, T. Cui, G. Yu, X. Lin, Q. Cheng, and J. Chin, "*Arbitrarily elliptical cylindrical invisible cloaking,*" J. Phys. D: Appl. Phys. 41, 085504, 2008.

[63] W.X. Jiang, J. Y. Chin, Q. Cheng, R. Liu, and T. J. Cui, "*Analytical design of conformally invisible cloaks for arbitrarily shaped objects,*" Phys. Rev. E 77, 066607, 2008.

[64] A. Nicolet, F. Zolla et S. Guenneau, "*Electromagnetic analysis of cylindrical cloaks of arbitrary cross-section,*" Optics Letters, 44, 1150-1154, 2008.

[65] A. Noor and Z. Hu, "*Cloaking of metallic sub-wavelength objects by plasmonic metamaterial shell in quasistatic limit,*" IET Microw. Antennas Propagat. 3, 40 (2009)

[66] J. Avelin, R. Sharma, I. Häninnen and A. H. Sihvola, "*Polarizability analysis of cubical and square-shaped dielectric scatterers,*" IEEE Trans. Antennas Propagat. 49, 451, 2008.

[67] J. Avelin and A.H. Sihvola, "*Polarizability of polyhedral dielectric scatterers,*" Microw. Opt. Technol. Lett. 32, 60, 2002.

[68] D.F. Herrick and T.B.A. Senior, "*Low frequency scattering by rectangular dielectric particles,*" Applied Physics 13, 175, 1977.

[69] R. W. Ziolkowski, "*Superluminal transmission of information through an electromagnetic metamaterial,*" Phys. Rev. E 63, 046604, 2001.

[70] S. Tricarico, F. Bilotti, and L. Vegni, "*Reduction of optical forces exerted on nano-particles covered by scattering cancellation based plasmonic cloaks,*" Phys. Rev. B 82, 045109, 2010.

[71] S. Albaladejo et al., "*Scattering forces from the curl of the spin angular momentum of a light field,*" Phys. Rev. Lett. 102, 113602, 2009.

[72] V. Wong and M.A. Ratner, "*Gradient and nongradient contributions to plasmon-enhanced optical forces on silver nanoparticles,*" Physical Review B 73, 075416 (2006).

[73] P. C. Chaumet and M. Nieto-Vesperinas, "*Time-averaged total force on a dipolar sphere in an electromagnetic field,*" Opt. Lett. 15, 1065, 2005.

[74] R. G. Newton, "*Optical theorem and beyond,*" Am. J. Phys 44, 639–642, 1976.

[75] L. Novotny and B. Hecht, *Principles of Nano-Optics, Cambridge University Press*, Cambridge, 2006.

[76] P.C. Chaumet and A. Rahmani, "*Electromagnetic force and torque on magnetic and negative-index scatterers,*" Opt. Express 17, 2224, 2009.

[77] N.I. Grigorchuk P.M. Tomchuck, "*Force of optical radiation pressure on a spheroidal metallic nanoparticle,*" Opt. Express 10, 2007.

[78] Y. Harada and T. Asakura, "*Radiation forces on a dielectric sphere in the Rayleigh scattering regime,*" Optics Communications 124, 529-541, 1996.

[79] M. G. Silveirinha, "*Nonlocal homogenization model for a periodic array of μ-negative rods,*" Phys. Rev. E 73, 046612, 2006.

[80] P.C. Chaumet and M. Nieto-Vesperinas, "*Coupled dipole method determination of the electromagnetic force on a particle over a flat dielectric substrate,*" Phys. Rev. B 61, 14119, 2000.

[81] J. Venermo and A. Sihvola, "*Dielectric polarizability of circular cylinder,*" Journal of Electrostatics 63, 101-117, 2005.

[82] P.L. Marston and J.H. Crichton, "*Radiation torque on a sphere caused by a circularly polarized electromagnetic wave,*" Phys. Rev. A 30, 2508, 1984.

[83] J.A. Stratton, Electromagnetic Theory, McGraw-Hill Companies, New York, USA, 1941.

[84] A. Kuhn, "*Modeling electrical stimulation,*" University Hospital Balgrist, Zurich, Switzerland, 2008 (*PhD Thesis*).

[85] http://www.iai.csic.es/tremor

[86] D.C. Boyd, P.D. Lawrence, P.J. Bratty, "*On modeling the single motor unit action potential,*" IEEE Transactions on Biomedical Engineering, vol. BME-25, 236-243, 1978.

[87] L.M. Livshitz, J. Mizrahi, P.D. Einziger "*Interaction of array of finite electrodes with layered biological tissue: effect of electrode size and configuration,*" IEEE Transactions on Neural Systems and Rehabilitation Engineering, vol. 9, 355-361, 2001.

[88] T.A. Kuiken et al., "*Finite element modeling of electromagnetic signal propagation in a phantom arm*," IEEE Transactions on Neural Systems And Rehabilitation Engineering, vol. 9, no. 4, 346-354, 2001.

[89] T. Keller et al., "*New multi-channel transcutaneous electrical stimulation technology for rehabilitation,*" Proc. of the 28th IEEE EMBS Annual International Conference, New York City, USA, Aug 30-Sept 3, 2006.

[90] R. Ploinsey, D.B. Heppner, "*Considerations of quasi-stationarity in electrophysiological systems,*" Bulletin of Mathematical Biophysics, vol. 29, 657-664, 1967.

[91] A. Kuhn, T. Keller, "*A 3D transient model for transcutaneous functional electrical stimulation,*" Proc. of 10th Annual Conference of the International FES Society, Montreal, Canada, July 2005.

[92] A. Kuhn, T. Keller M. Lawrence, M. Morari, "*A model for transcutaneous current stimulation: simulations and experiments,*" Med. Biol. Eng. Comput., 47, 279–289, 2009.

[93] http://niremf.ifac.cnr.it/tissprop/htmlclie/htmlclie.htm

[94] R. Merletti et al., "*Modeling of surface myoelectric signals – part I: model implementation,*" IEEE Transactions on Biomedical Engineering, vol. 46, 810-820, 1999.

[95] R. Merletti et al., "*Modeling of surface myoelectric signals – part II: model-based signal interpretation,*" IEEE Transactions on Biomedical Engineering, vol. 46, 821-828, 1999.

[96] D. Farina, R. Merletti, "*A novel approach for precise simulation of the EMG signal detected by surface electrodes,*" IEEE Transactions on Biomedical Engineering, vol. 48, 637-646, 2001.

[97] S. Tricarico, M. Goffredo, F. Bilotti, T. D'Alessio, L. Vegni, "*Transient quasi-static passive model Of the upper limb under surface electrical stimulation: Finite integration based approach,*" Proc. of ISEK, Aalborg, Denmark, 2010.

[98] M. Goffredo, S. Conforto, M. Schmid, T. D'Alessio, "*Strength-duration properties of the upper limb under surface electrical stimulation for rehabilitation,*" IASTED 2010.

[99] M. Goffredo, S. Tricarico, L. Schinaia, M. Schmid, S. Conforto, T. D'Alessio, "*Active model of nerves in the upper limb under surface electrical stimulation,*" Proc. of ISEK, Aalborg, Denmark, 2010.

[100] C. Gabriel, "*Dielectric properties of biological tissue: variation with age,*" Bioelectromagnetics Supplement, 7, S12-S18, 2005.

[101] P.A. Mason et al., "*Effects of frequency, permittivity, and voxel size on predicted specific absorption rate values in biological tissue during electromagnetic-field exposure,*" IEEE Transactions on Microwave Theory And Techniques, vol. 48, 2050-2058, 2000.

[102] R.C. Dunn, "*Near-Field Scanning Optical Microscopy,*" Chem. Rev. 99, 2891-2928, 1999.

[103] F. Bilotti, S. Tricarico, F. Pierini, and L. Vegni, "*Cloaking apertureless near-field scanning optical microscopy tips,*" Optics Letters, vol. 36, No. 2, 211-213, 2011.

[104] P. B. Johnson and R. W. Christy, "*Optical Constants of the Noble Metals,*" Phys. Rev. B 6, 4370-4379, 1972.